Title

Synthesis, Surface Modification, and Stabilization of Plasmonic Metal Nanoparticles and Perovskite Nanocrystals

Author

Guarino-Hotz, Melissa Elizabeth

Publication Date

2022

UNIVERSITY OF CALIFORNIA

SANTA CRUZ

Synthesis, Surface Modification, and Stabilization of Plasmonic Metal Nanoparticles and Perovskite Nanocrystals

A dissertation submitted in partial satisfaction

of the requirements for the degree of

DOCTOR OF PHILOSOPHY

in

CHEMISTRY

by

Melissa Guarino-Hotz

December 2022

The Dissertation of Melissa Guarino-Hotz is approved:

Professor Jin Zhang, Chair

Professor Scott Oliver

Professor David Kliger

Peter Biehl
Vice Provost and Dean of Graduate Studies

TABLE OF CONTENTS

LIST OF FIGURES

LIST OF TABLES

ABSTRACT

Synthesis, Surface Modification, and Stabilization of Hollow Plasmonic Metal Nanoparticles and Perovskite Nanocrystals

Melissa Guarino-Hotz

Nanomaterials composed of metals and semiconductors have been studied as powerful tools for various applications in the fields of diagnostics, therapy, sensing, and photovoltaics. Based on the specific application, these nanomaterials can be tuned and optimized to achieve their best performance. Modifications can be made to alter the size, shape, surface morphology, and surface passivation of these nanoparticles. In this dissertation, the effect of these changes on the optical characteristics necessary for effective performance of hollow plasmonic nanoparticles and perovskite nanocrystals are investigated.

In chapter 1, a comprehensive literature review was completed on hollow plasmonic nanoparticles, their synthetic procedures, and their applicability to the biomedical field. This chapter, describes the physical properties of hollow plasmonic structures, such as hollow gold nanospheres (HGNs), by discussing SPR and Mie theory. Numerous synthetic methods leading to hollow structures, including galvanic exchange, and ways to effectively tune size, shell thickness, and surface properties were described. Finally, hollow plasmonic particles' ability to sense, image,

diagnose, and treat diseases were assessed based off the changes in their physical properties.

In chapter 2, HGNs, hollow gold nanostars (HNSs), and silver coated hollow gold nanostars (AgHNSs) were synthesized and compared for their SERS applicability. It was demonstrated in this work that both HNSs and AgHNSs exhibit tunable structural and optical properties. Using rhodamine 6G as a probe molecule, it was determined that HNSs reported an order of magnitude higher relative enhancement over previously reported HNSs and AgHNSs have a four-fold increase in SERS signal compared to HNSs reported herein. Theoretical analyses were compared to the experimental findings, which suggested that the increase in enhancement was not completely due to the addition of silver, but also potentially the branching of individual spikes or increased binding efficacy of the analyte to the nanoparticle. To further explore the applicability of these nanoparticles, capping ligand exchange was completed from citrate to pentanethiol to increase their interaction with negative analytes like bovine serum albumin.

In chapter 3, methylammonium lead bromide magic sized clusters (MSCs) and quantum dots (QDs) were synthesized using a new heated ligand assisted reprecipitation method. A mixture of QDs and MSCs were tuned to monodispersed MSCs by increasing the temperature of the precursor solution. Additionally, the size of the MSCs themselves was tuned by increasing the temperature of the precursor solution and increasing the concentration of capping ligand. The MSCs were analyzed with Raman spectroscopy and determined to be similar to bulk perovskite.

Using IR, mass spectrometry, and control experiments it was determined that oleylamine was the primary capping ligand on the surface of the magic-sized cluster and therefore that the surface must be cationic in nature.

In chapter 4, a comparison of the stability of previous ligand assisted reprecipitation method and newer temperature dependent synthesis of MSCs was made. The MSCs were placed under ambient conditions and exposed to water and observed until they no longer emitted light. Then, they were stabilized with noncoordinating polymer matrix, paraffin, and the solution was then similarly exposed to water and observed until both particles degraded. The paraffin MSCs mixtures were then dried as a film. The LARP MSCs degraded after 3 hours, but the HLARP MSCs remained luminous for 8 days when stabilized with paraffin. Both solids were analyzed with Raman spectroscopy. HLARP MSCs were then characterized using X-ray diffraction and TEM. It was determined that HLARP MSCs are more ordered that LARP MSCs and have an orthorhombic quasi-crystalline structure.

DEDICATION

To my amazing family, friends, and cohort.

It takes a village.

ACKNOWLEDGEMENTS

I would like to thank my advisor, Jin Z. Zhang for giving me the opportunity to join his research group and learn under his supervision. His support and guidance made this journey possible. I would also like to thank my dissertation committee, Scott Oliver and David Kliger for their assistance during these last 5 and a half years.

I also thank my past lab mates, Sarah Lindley, Sara Bonabi, Evan Vickers, and A'lester Allen-Wiggins for patiently training me on instruments, synthesis and helping me get started in the lab. I appreciate their thoughtful advice through this journey. I want to thank my current lab mates, Vivien Cherrette, Heng Zhang, Kevin Chou, Allison Win, and Celia Tdd for their support and making the lab more fun with their energy. I am grateful for all the undergraduate students who helped me immensely during these years, Amanda Brewer, Rebecca Lee, and Liem Pham.

I am also grateful for having my amazing cohort, Jeremy Barnett, Rachel Harold, Kenna Sarka, Jonathan Philpott, Kaitlyn Vian, Anna Johnston, Mingpeng Chen, Forrest Nichols, Stephanie Holmes, Mark Wadolkowski, Michael Dang, Alexandria Smart, Beatriz Ehlke, Chris van Hoorebeke, Grant Koch, Megan Freyman, Justin Farris, and David Delgadillo for being such amazing friends. We went through this process together and we overcame every challenge together.

I would also like to thank my distant support network, my parents, Bettyann and Hank, and my friends, Leeann Page, Jessica Liaudat, Kate Edelson, Alison Reger, and Erik Lehmer for always unconditionally supporting me even from afar. They were always there to listen to me during stressful times and assured me that everything is going to be alright.

The text of this dissertation includes reprints of the following previously published material:

Chapter 1: Guarino-Hotz, M.; Zhang, J. Z. Structural Control and Biomedical Applications of Plasmonic Hollow Gold Nanospheres: A Mini Review. *WIREs Nanomedicine and Nanobiotechnology n/a* (n/a), e1694. https://doi.org/10.1002/wnan.1694.

Chapter 2: Guarino-Hotz, M.; Allen, A. C.; Wang, A.; Zou, S.; Zhang, J. Z. Near-Infrared Light Absorbing Silver-Coated Hollow Gold Nanostars for Surface-Enhanced Raman Scattering Detection of Bovine Serum Albumin Using Capping Ligand Exchange. *J. Phys. Chem. C* **2022**. https://doi.org/10.1021/acs.jpcc.1c09034.

Allen, A. C.; Efrem, M.; Mahalingam, U.; Guarino-Hotz, M.; Foley, A. R.; Raskatov, J. A.; Song, C.; Lindley, S. A.; Li, J.; Chen, B.; Zhang, J. Z. Hollow Gold Nanosphere Templated Synthesis of PEGylated Hollow Gold Nanostars and Use for SERS Detection of Amyloid Beta in Solution. *J. Phys. Chem. B* **2021**. https://doi.org/10.1021/acs.jpcb.1c06776.

Allen, A. C.; Guarino-Hotz, M.; Getahun, A.; Dubois, R.; Zhang, J. “Hollow Gold Nanostars and His-Tagged Antibodies: A Simple Solution for Detecting SARS-CoV-2," *submitted*.

Chapter 3: Guarino-Hotz, M.; Barnett, J. L.; Pham, L. B.; Win, A. A.; Cherrette, V. L.; Zhang, J. Z. Tuning between Methylammonium Lead Bromide Perovskite Magic-Sized Clusters and Quantum Dots through Ligand Assisted Reprecipitation at Elevated Temperatures. *J. Phys. Chem. C* 2022, *126* (32), 13854–13862. https://doi.org/10.1021/acs.jpcc.2c04384.

Chapter 4: Guarino-Hotz, M., et al. “Structural Study of Paraffin-stabilized Methylammonium Lead Bromide Magic Sized Clusters: Implications in Photonics” *Submitted to ACS Applied Nanomaterials*

Chapter One

1 Structural Control and Biomedical Applications of Plasmonic Hollow Gold Nanospheres: A Mini Review

1.1 Abstract

Hollow gold nanospheres (HGNs) are core/shell structures with core being a dielectric material such as solvent and shell being the gold metal. Such structures have two metal/dielectric interfaces to allow interaction between the gold metal with the interior and external dielectric environment. Upon illumination by light, HGNs exhibit unique surface plasmon resonance (SPR) properties compared to solid gold nanoparticles. Their SPR absorption/scattering can be tuned by changing the diameter, shell thicknesses, and surface morphologies. In addition to the low toxicity, easy functionalization, resistance to photobleaching, and sensitivity to changes in surrounding medium of gold, the enhanced surface-to-volume ratio and tunable SPR of HGNs make them highly attractive for different applications in the fields of sensing, therapy, and theranostics. In this article, we review recent progress on the synthesis and structural control of HGNs and applications of their SPR properties in biomedical sensing and theranostics.

1.2 Introduction

Nanoplasmonics is the study of nanoparticles typically composed of noble metals, *e.g.,* copper, silver, and gold, that exhibit the interesting phenomenon of surface plasmon resonance (SPR). SPR absorption occurs when light is on resonance with the intrinsic oscillating frequency of conduction band electrons in plasmonic metal nanostructures.[1] The interaction between light and plasmonic nanoparticles can be described using Mie theory based on Maxwell's equations to describe SPR position and a particle's interaction with surrounding media.[2] One important characteristic of the SPR plasmonic nanoparticles is their strong dependence on shape and, to a lesser degree, on size.[2,3] Plasmonic metal nanoparticles with strong visible light extinction have been used for biomedical sensing, diagnosis, and therapy. Elemental composition, size, and surface morphology can be tuned to optimize desired performance.[4–7]

Gold, in particular, has been used for medical applications due to its stability, low toxicity, and biological compatibility. Indeed, it has been in vivo without eliciting a proinflammatory response.[8] Moreover, gold can be functionalized to interact and bind to biological systems. A number of biologically relevant linkers can be conjugated to the surface of gold nanoparticles including antibodies[9], peptides[10], and oligonucleotides[11] allowing particles to bind in close proximity to diseased tissue.[11,12] Additionally, gold nanoparticles exhibit strong photothermal effects and are capable of transferring light to heat through electron-phonon coupling.[13] They can also provide enhanced electromagnetic fields that are important for applications such as surface enhanced Raman scattering (SERS).[14]

Optical performance is affected by the shape of the nanoparticle. Gold nanoparticles can be synthesized to form many shapes such as solid nanospheres, nanorods, nanocages, or hollow gold nanospheres (HGNs). Solid nanospheres typically absorb light around 520 nm.[15] This is a limiting factor for a number of therapeutic techniques. Tissue and blood also absorb light in the visible region of the spectrum. Thus, nanoparticles with visible light extinction compete with blood and tissue for irradiated light. For biomedical applications, particles should ideally absorb in the near infrared (NIR) window (650 nm – 1700 nm), where tissue and blood do not interfere.[16] There are a number of gold nanoparticles with SPR that can be tuned to the NIR window, including gold nanorods, gold nanocages, and HGNs. Gold nanorods exhibit two plasmon modes, transverse and longitudinal, resulting in two SPR peaks. However, many techniques perform better with a single, narrow absorption peak.[17] Nanocages, which are cubic and hollow, often have broad SPR.[18] HGNs have the advantageous combination of strong, tunable, and narrow NIR SPR.

HGNs are solvent-filled, hollow shells of gold with tunable SPR from 540 to1000 nm.[19–21] Their tunability arises from changing the size and aspect ratio of the structure and allows them to be used in a large number of applications.[19,20,22,23] Their hollow structure affords them an internal and an external surface, whose coupling creates an enhanced electromagnetic field useful in the field of SERS.[24] These internal and external surfaces also result in increased contact with the surrounding media, increasing sensitivity for refractive index sensing.[25] The increased surface to volume ratio also makes them ideal for drug loading.[26–28] Unfortunately, the synthesis of HGNs is non-trivial and requires the use of a sacrificial template. This requirement makes their production more difficult. Therefore, many studies have focused on gaining precise control over their physical and optical properties by controlling their size, shell thickness, and surface morphology.[19,22,23,29,30]

The ability to precisely tune the optical properties of HGNs combined with their biological compatibility and ease of functionalization control has allowed them to be applied and ameliorate several fields. In this review, we introduce the HGN synthesis as well as progress made in tuning the size, shell thickness, and surface morphology. We also discuss how the advantageous HGN structure and how its optical properties have enhanced biomedical applications, including refractive index sensing,[31–33] SERS,[34–36] photoacoustic imaging,[37–40] photothermal ablation therapy,[27,41,42] drug delivery,[26–28] and gene silencing.[43] Moreover, we show the multimodal capabilities that allow HGN's to be used for diagnosis and multiple therapies to be performed simultaneously[27,44].

1.3 Structural Control in HGN Synthesis

1.3.1 Synthesis via galvanic exchange

Galvanic exchange is a common approach to synthesize hollow nanostructures. In this method, one metal is reduced by the oxidation of another, in an electrolytic solution, driven by the difference between their reduction potentials. In the case of HGNs, a low-reduction-potential metal is used to form a sacrificial nanoparticle scaffold. To deposit a gold shell, gold ions are introduced, and galvanic exchange occurs spontaneously due to the difference in reduction potentials. Gold is reduced onto the framework of the scaffold as the scaffold oxidizes and returns to solution.[45] Residual scaffold can then be removed with further oxidation, leaving a solvent-filled shell of gold.

Silver[22,46,47] and cobalt-based[19,21–23,48,49] nanoparticles are often used as templates for making HGNs because they have appropriate reduction potentials (0.7996 V and -0.28 V, respectively) as compared to that of gold (1.498 V).[50] While using silver as a template can yield NIR light emitting particles, there has been less work done to optimize and fine tune their synthesis and particles tend to be more polydispersed.[22,46,47] Additionally, the higher reduction potential of silver often results in an alloyed structure with a broadened SPR. Using cobalt as a sacrificial template, the resulting HGNs tend to be more uniform with narrow SPR, partially due to the ease of scaffold oxidation and removal.[51] Moreover, much work has been done to optimize the parameters involved in synthesis, resulting in improved reproducibility.[19] As such, this review focuses on HGNs synthesized through galvanic exchange with cobalt-based templates. The following paragraphs provide details for each step of the synthesis: cobalt-based nanoparticle formation, galvanic exchange, and subsequent core oxidation.

In the first step, cobalt nanoparticle templates are typically prepared by reducing cobalt (II) chloride with sodium borohydride in an anaerobic environment and in the presence of sodium citrate stabilizing agents.[19,21,22,52] Cobalt coalesces to form particles until it reaches a stable size.[53,54] The scaffold mechanism has been intensely studied, but some disagreement exists as to the final product. Although many have described nanoparticles produced by this method as elemental cobalt, various cobalt borides have been experimentally identified as the main products.[48,49,55] The commonly accepted reaction mechanism with a cobalt boride product is provided in Equation (1).

$$2CoCl_2 + 4NaBH_4 + 9H_2O \rightarrow Co_2B + 4NaCl + 12.5H_2 + 3B(OH)_3 \qquad (1)$$

The formation mechanism has been recently studied using XANES and XPS to confirm that elemental cobalt was not a product of this reaction, also suggesting a cobalt boride product.[19]

In step two, a gold salt solution is added to induce galvanic exchange. As mentioned above, the gold metal deposits onto the cobalt scaffold as it oxidizes into solution. In step three, oxygen is introduced to oxidize the residual cobalt core (Figure 1-1).[45,56] Steps two and three can also be carried out simultaneously.[57] Conducting the synthesis in three separate steps and carrying out galvanic exchange in absence of oxygen enables formation of smooth and continuous shells. The continuous shells can be made thinner and reach more red-shifted SPRs. It is a common misconception that cobalt remains a part of the structure when HGNs are synthesized in this way.[58] However, with proper washing and post-synthetic treatment, ICP-OES has shown that cobalt ions can be efficiently removed and negligible amounts remain in the final HGN structure.[29]

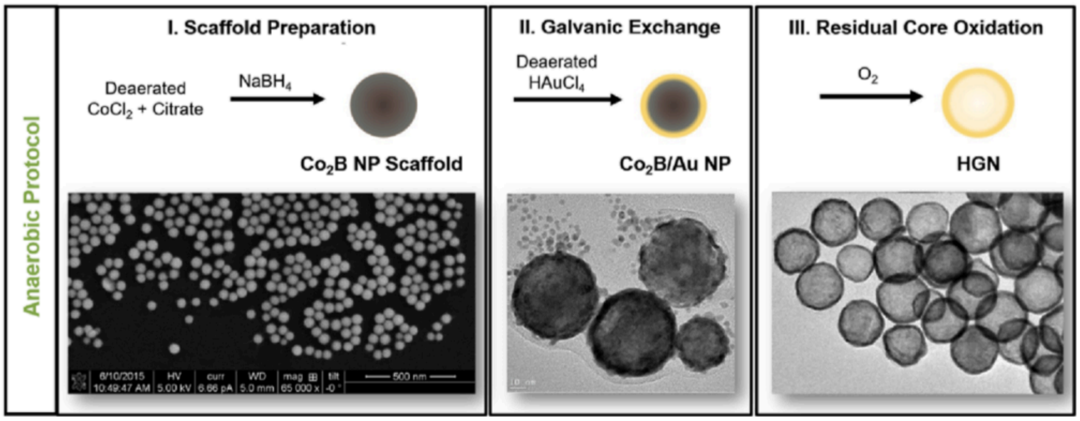

Figure 1-1) Galvanic exchange protocols for HGN synthesis. Anaerobic protocol: galvanic exchange and oxygenation steps are separated, and the gold salt is deaerated so that galvanic exchange may be carried out in the absence of environmental oxygen. A representative SEM image is provided for the cobalt nanoparticle (Co_2B NP) formed in step I and representative HRTEM images are provided for the Co2B NP/Au core/shell structures and resultant HGNs formed in steps II and III, respectively.[19]

1.3.2 Tuning size and shell exchange

Since the optical properties of the HGN are dictated by aspect ratio (ratio of shell thickness to diameter), precise control over the particle structure is essential for achieving the desired optical properties. In general, the SPR of the HGN can be shifted to longer wavelengths by two mechanisms: increasing the overall diameter or decreasing the shell thickness (Figure 1-2). Particles with SPR in the NIR window are especially attractive for many biomedical applications due to deeper tissue penetrations. Additionally, for many of these applications, particles between 30-50 nm are most beneficial because they can be internalized into a cell.[59,60] Unlike solid particles, which can only red-shift by increasing diameter, the HGN diameter and

SPR can be tuned separately by changes in the shell thickness. The same size particle can be made at different SPRs, and the same SPR can be achieved with different diameters (Figure 1-2).

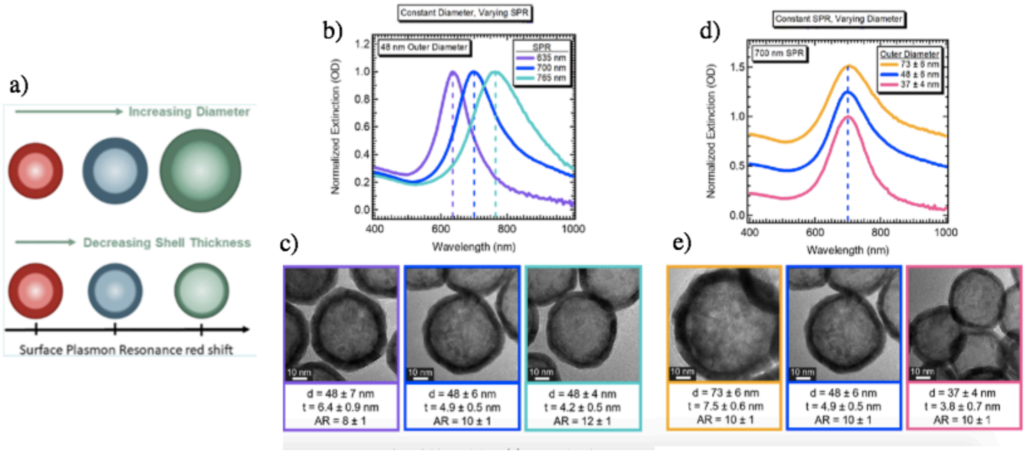

Figure 1- 2: Demonstration of twofold tunability. (a) relationship between SPR, size, and aspect ratio (b) Normalized extinction for HGNs with the same outer diameter but different SPR: 48 nm HGNs with 635, 700, and 765 nm SPR. (c) Corresponding HRTEM images with average diameter (d), shell thickness (t), and aspect ratio (AR) as indicated; scale bar 10 nm. (d) Normalized extinction for HGNs with a different outer diameter but the same SPR: 73 ± 6, 48 ± 6, and 37 ± 4 nm HGNs with 700 nm SPR. After normalization, the 48 ± 6 and 73 ± 6 nm extinctions were offset on the y-axis by 0.25 and 0.50 OD, respectively. (e) Corresponding HRTEM images with d, t, and AR as indicated; scale bar 10 nm. [19]

While, in principle, the diameter and shell thickness of HGNs can be tuned, precise experimental control is not trivial. As such, much of the previous work has concentrated on tuning and optimizing synthetic parameters for control of size and uniformity. The effects in relation to changing these parameters are listed in Table 1 below.

Table 1-1) Modifications of HGN Synthesis and Subsequent Effect on Particle and SPR

Modification	Effect on Particle	Effect on SPR
Increase [Citrate$^-$] capping agent	Decrease cobalt nanoparticle size	Blue-shift[23]
Increase [BH_4^-]	Decrease cobalt nanoparticle size	Blue-Shift[22]
Increase [$B(OH_4)/BH_4$]	Increase cobalt nanoparticle size, more monodispersed	Red-shift, smaller FWHM[19]
Increase temperature	Decrease cobalt nanoparticle size	Blue-Shift[21]
Increase rate of addition of cobalt nanoparticle to gold salt	More monodispersed	Smaller FWHM, blue shift[1,22,61]
Increase [$HAuCl_4$]	Increase HGN shell thickness	Blue-Shift[22]

In terms of size control, one can vary the concentration of capping ligand or reducing agent. Schwartzberg *et al*. reported that increasing the concentration of citrate capping ligand decreases the size of the resulting particles. The more citrate on the surface of the cobalt nanoparticles, the sooner they are stabilized and reach their critical radius, limiting their growth.[22] Alternatively, Schwartzberg *et al.* also showed that the cobalt size also decreases with increasing concentrations of reducing agent.[22] The degree to which the initial concentration of cobalt is reduced will determine the free cobalt in solution available to form nanoparticles. Increasing the concentration of borohydride forms more nucleation centers, which creates smaller particles. Using these methods in conjunction, it was possible to synthesize a range of particles from 25 nm to 71 nm.[22]

Size can also be tuned by changing the reaction temperature. According to Pu *et al.* increasing the temperature during the nucleation of cobalt ions created smaller cobalt nanoparticles.[21] The critical radius is dependent on temperature through its dependence on total free energy of a system.[21,62]

$$r_{crit} = \frac{-2\gamma}{\Delta G_v} = \frac{2\gamma v}{k_B T ln(S)} \qquad (2)$$

where critical radius is r_{crit}, surface free energy is γ, and total free energy of a bulk crystal is ΔG. As the temperature of the system is increased, less surface energy is necessary to reach the critical radius and form a stable nanoparticle. Thus, as the temperature is increased the nanoparticle size decreases. By varying the synthesis temperature it was possible to change the size of the HGN from 24 nm to 122 nm.[21]

Previous methods that achieved large size ranges were prone to polydispersity in the resultant structures. To solve this problem, Lindley *et al.* introduced $B(OH)_4^-$ as a growth agent during the BH_4 reduction of the cobalt nanoparticle. $B(OH)_4^-$ is the final product of the hydrolysis of BH_4.[19] It promotes coalescence by slowing down the nucleation of cobalt nanoparticles, leading to large scaffold diameters. The success of the introduction of $B(OH)_4$ was two-fold: By adding the $B(OH)_4$, it was possible to access a decent size range, from 19 nm to 76 nm, while also achieving monodispersity.[19]

Much work has also been carried out to control the thickness and quality of the gold shell formed during galvanic exchange. The shell thickness may be controlled simply by the concentration of gold used in the galvanic exchange step, where higher concentrations of gold result in thicker shells (and blue-shifted SPR) while lower concentrations of gold result in thinner shells (and red-shifted SPR).[23] However, it is important to note that the speed of the addition is also important for the homogeneity of the particle. For instance, Adams *et al*. changed the rate at which cobalt nanoparticles were added to a gold salt solution.[23] Slow addition of cobalt nanoparticles resulted in a broad distribution of shell thicknesses and blue-shifted particles. This was due to the nonuniform mixing in the cobalt nanoparticles that were added first and introduced to high concentrations of gold ions and thus formed thick shelled particles. However, cobalt nanoparticles toward the end of the addition were among significantly lower concentration of gold ions and thus formed thinner-shelled particles. The HGNs synthesized with fast addition during galvanic exchange were significantly red-shifted and more monodispersed.[23] In addition to thickness, the morphology of the shell wall has also been controlled, as discussed in the following section.

1.3.3 Surface morphology

Since the optical properties of plasmonic structures are shape dependent, the applicability of plasmonic particles can be improved by changing the shape or surface morphology of a nanoparticle. These changes can significantly alter the scattering, absorption, and surface to volume ratios allowing them to be tuned for specific applications and changing their ability to interact with their surrounding media.[63,64]

Bumpy and spikey HGNs have been engineered for use in sensing and theranostic applications[29,65]. Control of surface morphology has been primarily achieved by surfactant-directed seed-mediated growth, or template-directed growth. The synthetic parameters used to control morphology are outlined in Table 2.

Table 1-2) Modifications of Two Syntheses that Increase the Rugosity of a HGN

Type of Synthesis	Modification	Resulting morphology
Template-directed	Using PVP as a stabilizing agent[23]	Bumpy
Template-directed	Increasing [$HAuCl_4$][22,29]	Lightly Bumpy
Template-directed	Switching from anaerobic addition of gold to aerobic[19]	Bumpy
Template directed	Adding increasing OH^- addition to cobalt nanoparticles[29]	Bumpy to highly rugose (See Figure 1-4)

Surfactant-assisted seed-mediated growth	Increase volume of growth solution[66]	Spikey
Surfactant-assisted seed-mediated growth	Change Surfactant (CTAC to CTAB)[66]	Ranging from bumpy to spikey (see Figure 1-4)
Surfactant-assisted seed-mediated growth	Increase [NaBr][66]	Spikey

One surface control method can actually be achieved by changing the stabilizing agent. According to *Adams et al.,* using PVP results in bumpier surface morphology due to an unequal coating of gold.[23] However, this also results in relatively polydispersed particles that are difficult to biologically functionalize.[20,52]

Another method is to simply increase the amount of gold available for galvanic exchange; higher concentrations of gold results in thick shells with slightly bumpy surface morphology.[23] Although the reaction of gold salt with the cobalt nanoparticle scaffold occurs almost instantaneously, when the gold is added, a second shell-mediated growth may take place on a longer time scale, creating thicker and bumpier shells due to the reduction of gold by citrate.[22] Used independently, this technique is rather limited in its results and produces particles with minimal rugosity.

The presence of oxygen during galvanic exchange may be used in order to increase the rugosity of particles to a larger extent.[19,29] When the gold salt is efficiently deaerated and galvanic exchange is carried out in an air-free manner, smooth and continuous shells can be formed. However, if the gold salt is not deaerated and galvanic replacement is carried out in an aerobic environment, both galvanic replacement and removal of cobalt occur at the same time (Figure 1-3). This competition encourages patchwork deposition of gold and aids the formation of bumpy particles.[29]

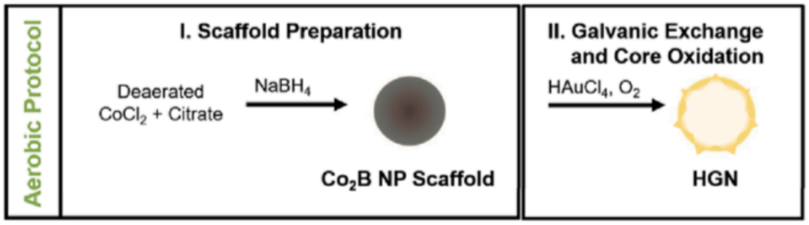

Figure 1-3) Aerobic protocol: cobalt nanoparticles (Co_2B NP) are prepared by wet-chemical reaction between cobalt ions and sodium borohydride, galvanic exchange is carried out by the introduction of Co_2B NP to aqueous gold ions, and the Co_2B NP core is simultaneously oxidized out of the shell by interaction with environmental oxygen resulting in bumpy surface morphology[19]

A more recent technique was developed utilizing the addition of OH^- ions. It was hypothesized that OH^- attaches to the surface of the cobalt nanoparticles inhibiting the ability of Au^{+3} ions to access the surface and promoting the formation of a bumpy shell.[29] By varying the concentration of free OH^-, it was possible to synthesize particles ranging from mildly bumpy to extremely rugose (Figure 1-4).[29] Figure 1-4a shows the particles morphology that results after aerobic addition of gold, with no addition of NaOH. Figure 1-4b-d show how the surface morphology changes when increasing volumes of NaOH are added to the gold salt before galvanic replacement. The rugosity increases with increasing amount of OH^- (Figure 1-4a-c) until structural integrity is lost (Figure 1-4d). Interestingly, when the OH^- was allowed to equilibrate with the gold salt before galvanic exchange, the rugosity decreased. During equilibration, the pH of the solution decreases as the OH^- displaces the chlorine ligands of the gold salt. Figure 1-4e shows the maximum addition of NaOH (same as Figure 1-4d) with a 60 minute equilibration before galvanic exchange. The surface structure of Figure 1-4e is more similar to that of Figure 1-4a (no OH) than Figure 1-4d. This result indicated that the increased rugosity of the nanoparticle is due to free OH^- in the solution, not speciation of the gold salt. As the volume of OH^- was increased and the shell morphology became more rugose, the particle diameters increased from 70 nm to 90 nm.[29]

Changing the surface morphology affects the resultant optical properties. For the HGNs shown in Figure 1-4a, with no addition of NaOH, the SPR was sharp and symmetric around 630 nm. However, as the structure became more rugose, the SPR broadened and red-shifted. In Figure 1-4d, when the shells lost structural integrity, the resultant extinction was flattened, lower, and broader, barely resembling an SPR.[29]

In syntheses, using surfactant directed seed mediated growth there is no use of the cobalt scaffold. Instead, numerous small silver seed particles were synthesized on negatively charged carboxylate-modified polystyrene beads.[30,66,67] These polymer particles were then added to a growth solution containing $HAuCl_4$, ascorbic acid, $AgNO_3$, and cationic surfactants. The standard reduction potentials of $Ag^+(aq)/Ag(s)$ and $AuBr_2^-(aq)/Au(s)$ are 0.962 and 1.11 V, respectively, allowing gold precursors to be reduced on polymer beads through both galvanic exchange and catalytic reduction, forming spikey HGNs. There are a number of ways to modify this synthesis to change the surface morphology of these particles. Similar to the above syntheses, it was also reported that increasing the volume of growth solution, *ie*. increasing the amount of gold, produced shells with longer spikes.[66] Halides have also been used to control spike formation. Changing the surfactant from cetyltrimethylammonium chloride (CTAC) to cetyltrimethylammonium bromide (CTAB) increases the rugosity of the shells (see Figure 1-4g-j).[30,66,67] Using CTAC as the surfactant resulted in rounded protrusions on the particles (Figure 1-4g). Moving to CTAB the structure moves to a spikey structure (Figure 1-4h). Finally, using CTAC with an addition Br^- (CTACBr) resulted in even finer spikes (Figure 1-4i-j).[66] Moreover, increasing additions of NaBr increased the spikey character of the gold shell.[66] This is likely explained by the preferential binding of bromide ions to selective facets of gold or silver, which has been found to promote the growth of anisotropic particles resulting in nanorods or spikes.[66,67]

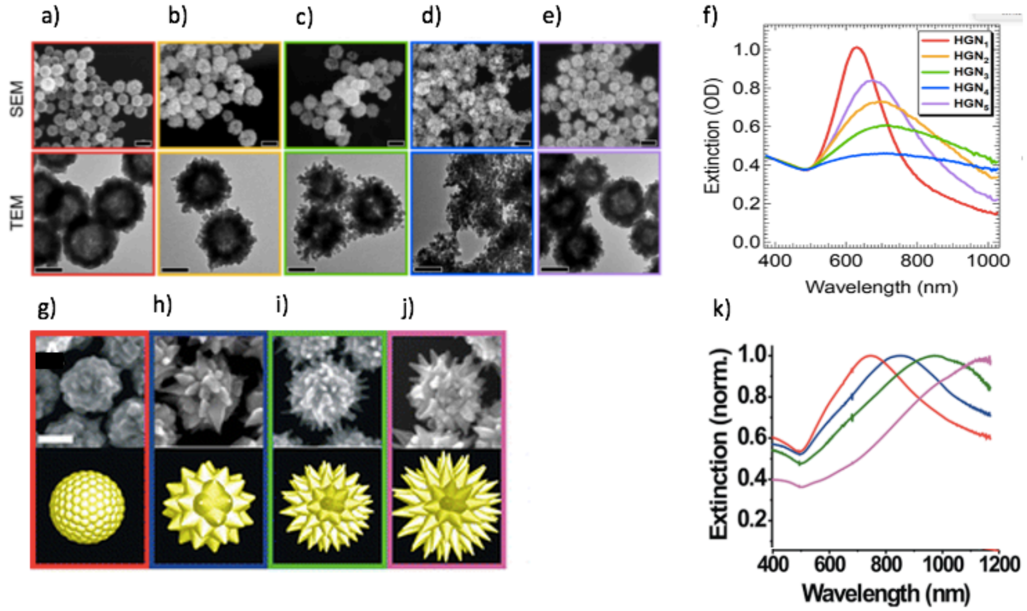

Figure 1-4) (a-d) SEM and TEM images of Bumpy Hollow Gold Nanospheres made using template directed method and increasing concentrations of OH^- from left to right. (e) SEM and TEM image of bumpy hollow gold nanospheres with maximum addition of NaOH and 60-minute wait time before injection of NaOH. SEM scale bars are 100 nm. TEM scale bars are 50 nm[29]. (f) Uv-Vis spectra of corresponding Bumpy HGNs[29] (g-k) SEM images of Spikey HGNs synthesized using the surfactant-assisted seed-mediated method Through Change of Surfactant (g) CTAC (h) CTAB (i and j) CTACBr (k) Uv-Vis spectra of corresponding Spikey HGNs[66]

Similar to the bumpy particles shown in Figure 1-4a-d. The spikier particles (Figure 1-4g-j) showed a broadened and red-shifted SPR broadened and red-shifted. This is also likely due to the increased size, 176 nm to 212 nm.[66] Moreover, smooth HGNs and spiky HGNs with differing lengths of spikes were compared for single particle scattering measurements. Smooth particles had significantly lower scattering intensities than spikey HGNs and scattering intensity increased with the rugosity of the particle.[67]

Since structure dictates function, major strides have been made in the ability to control the size, shell thickness, and surface morphology of HGNs.[68] Tuning the thickness and rugosity of a nanoparticle changes its optical extinction and its performance in absorption, or scattering, based applications. Synthesizing particles with rugose surface morphology red-shifts the SPR significantly, creating another synthetic pathway to produce NIR light absorbing particles for biological applications. However, the particles tend to be larger, which could make it more difficult to internalize them into a cell.[69] Nevertheless, the increased surface area makes them ideal for drug loading and catalysis.[29] These particles also have the potential of increased local field enhancements for sensing.[70] The advantages of increased synthetic control are presented and discussed in the next section.

1.4 Enhanced Performance in Biomedical Applications

1.4.1 Sensing

The hollow structure, stability, enhanced electromagnetic field, resistance to photobleaching, biocompatibility, NIR absorption, and high surface to volume ratio of HGNs make them ideal for multiple applications in the field of sensing, allowing for earlier detection, higher sensitivity, and lower limits of detection. Recent developments in refractive index sensing, SERS, and imaging are outlined below.

1.4.1.1 Refractive Index Sensing

Refractive index (RI) sensing is the use of changes in spectral profiles in response to environmental RI changes to detect molecules. It is used to make biosensors that detect the adsorption of target molecules for label-free detection of analyte/receptor interactions such as antibodies and antigens or DNA hybridization.[71] The SPR of plasmonic nanoparticles is very responsive to changes in the surrounding medium, with the SPR red-shifting with increase in refractive index. Biological materials usually have a higher refractive index than the surrounding medium, increasing the surrounding mediums refractive index and causing the SPR of the nanoparticle to red-shift. HGNs have been shown to make excellent substrates for RI sensing due to their hollow structure, which increases the surface area in contact with the surrounding medium.[33,64] Additionally, hollow particles show stronger plasmonic fields than their solid counterparts from the coupling between internal and external surface plasmon fields.[32] In a study done by Tuersun *et al*., the geometrical parameters of HGNs and silica-core gold nanoshells were compared and investigated with Mie Theory. HGNs of the same diameter were determined to have a higher RI sensitivity than the same sized silica core counterparts.[72] Similarly, in a number of studies, it was shown that HGNs outperformed solid gold nanospheres.[25,32] Refractive index sensitivity is compared by using sensitivity factors, described by the shift in SPR per surrounding medium refractive index unit (RIU).[64] The reported sensitivity factors of HGNs are subject to change from study to study, but are typically reported around 400 nm/RIU.[64] This is twice as sensitive as a 2-D photonic crystal used in RI sensing technology and can detect a change of 0.001 RIU.[73,74] Sun *et al*. attributed their improvement to the change in dielectric sensitivity of hollow nanostructures[25] while Mamoud *et al*. attributed it to the stronger surface plasmon fields from the coupling of an interior and exterior wall.[32] Mamoud *et al*. also showed that sensitivity factors increase linearly with aspect ratio and confirmed with DDA calculations.[32] With their increased sensitivity, HGNs have been incorporated into optical fiber biosensors that have been used to detect thyroglobulin with an impressive LOD of 0.19 pg/ml[75] and rabbit IgG with a LOD of 0.019 μg/ml.[31]

It should be noted that gold nanorods often report sensitivity factors higher than those of HGNs, around 490 nm/RUI.[64] However, while much research has been conducted to optimize the functionality of thin-shelled HGNs, the high aspect ratios of spikey HGNs would also prove to be effective for RI sensing. According to Pallares *et al.*, spikey solid gold nanoparticles exhibited increased sensitivity factor to 533 nm/RUI due to their high surface-area-to-volume ratio,[76] higher than those typically reported for gold nanorods. One may expect that hollow bumpy and spikey HGNs with their increased SPR and surface area would also produce even higher sensitivity factors for RI sensing

1.4.1.2 Surface enhanced Raman scattering

Raman spectroscopy measures the polarizability of a molecule. It is molecularly specific and has low interference with water, making it very useful in the detection of biological molecules. However, it has a very low quantum yield. Therefore, SERS is employed to increase the low quantum yield by allowing molecules to interact with a roughened metal surface, scattering incident light and creating a strong electromagnetic field.[77] It is highly desirable for SERS substrates to be monodispersed and stable to allow for consistent and reproducible collection of data. With the continued optimization of the HGN synthesis, HGNs have become more desirable as SERS substrates.[78,79] Silver substrates are commonly reported to have increased SERS signal over gold.[80] However, silver is much more reactive than gold, which can produce inconsistent results.[81] According to *Schwartzberg et al.* using HGNs over silver substrates led to 10-fold signal consistency and increased sensistivity.[79] Moreover, the spherical shape of HGNs leads to improved consistency and sensitivity over gold nanorods due to the angle dependence of SERS signal intensity.[82]

Moreover, HGNs are well-positioned to serve as *in vivo* SERS substrates. As mentioned, they maintain the biological compatibility and ease of functionalization of their solid gold counterparts. However, they are tunable to the NIR window and remain in biologically relevant size ranges. HGNs, like most gold nanoparticles, may be functionalized using heterobifunctional polyethylene glycol, that protects the nanoparticle, allowing them to be circulated in the bloodstream, and attached to a biologically useful molecule like an antibody, peptide, or oligonucleotide.[12,29,35,39,40] However, unlike solid gold nanoparticles, the SPR is tunable to the NIR window while the particle diameter remains in biologically relevant size ranges. Additionally, HGNs have a stronger LPSR than solid gold nanospheres[83] and more intense electromagnetic field due the coupling of interior and exterior surface fields.[24] This combination of attributes has led to numerous successful trials in detecting cancer phenotypes,[84] tumor antigens,[78] and multiple biomarkers simultaneously through the use of reporting molecules.[35]

This is exemplified by a study on the rapid and sensitive detection of breast cancer phenotype markers. Three different nanotags with different Raman reporter molecules were conjugated to HGNs. Each nanotag was designed to attach to a different phenotype using specific antibodies, allowing for fast identification of cancer cell phenotypes using Raman mapping without the need of complicated data analysis. Showing marked improvement from fluorescent tagging, HGNs can test phenotypes and quantify proteins simultaneously.[84] Wang *et al*. have also used a SERS based immunoassay for neuron-specific enolase and S100-β protein. The concentrations of these compounds in blood are useful in the preliminary determination of brain injuries. HGNs, through the use of reporting molecules like mercaptobenzoic acid, produced an accurate and sensitive immunoassay with a linear detection range of 0.2 to 22 ng/mL for both biomarkers. Interference studies were conducted in human serum samples with bovine serum albumin, glucose, carcinoembryonic antigen, and neuron specific enolase which were in good agreement with the commonly conducted enzyme-linked immunosorbent assay method. This SERS based immunoassay provided a more specific and sensitive technique than currently used methods and allows for earlier detection of brain injuries.[34] HGNs are proving to be a more sensitive substrate for immunoassays with much improved multiplexing capabilities.

Since SERS relies on a field enhancement from a roughened metal substrate,[77] spikey HGNs were employed as an alternative substrate. Spikey HGNs are less monodispersed than smooth HGNs but show a marked enhancement in SERS signal due to an increase in locally enhanced electric fields and generation of hot spots between the junctions of the tips.[85] Using single particle measurements, it was determined that spikey HGNs with longer spikes showed red-shifted SPR and had more scattering than smooth particles. Since these spikes are arranged at all angles, any polarization of incident light can produce significant localized electric fields at every spike. These particles allow single particle detection of mercaptobenzoic acid.[67] The increased scattering properties of spikey and bumpy HGNs make them ideal, sensitive candidates for SERS.

1.4.1.3 Imaging

HGNs have been used for magnetic resonance, nuclear, fluorescent, and photoacoustic imaging of disease markers.[86] We focus our discussion on photoacoustic imaging, a modality which does not require the coupling with another particle.

Photoacoustic imaging uses the generation of an acoustic wave resulting from the absorption of optical energy. Incident radiation causes a rapid thermoelastic expansion of tissue and contrasting agents, creating an ultrasonic wave which can be used to create an image.[38–40,87] Contrasting agents should have a low quantum yield, be resistant to photobleaching, have low toxicity, and be biologically compatible and easily functionalized.[88] HGNs make excellent contrasting agents due to their strong resonant absorption tuned to the NIR window, biocompatibility, and biological functionalization.[40] HGNs can be functionalized to attach to tumor cells for targeted imaging. Moreover, they can circulate the bloodstream to detect if cancer is beginning to metastize.[39] This allows for early detection of the spread of cancers. It is non-invasive with high spatial resolution (as low as 5μm) at depths as low as 5-6 cm.[87] According to Lu *et al.*, functionalized HGNs improved the contrast of brain vasculature in a mouse brain when injected into the middle cerebral artery, yielding significantly higher resolution images than intrinsic optical contrast of blood alone.[40] Figure 1-5A shows photoacoustic imaging of the mouse brain pre-injection to illustrate baseline intrinsic contrast. Figure 1-4F shows an open skull photograph of a mouse brain. Figures 1-5B and 1-5C show the same image at 5 minutes and 2 hours post-injection, respectively. Structural detail is noticeably improved. The differential images shown in Figure 1-5D and 1-5E, obtained by removing the baseline signal shown in Figure 1-5A, illustrate the extent of resolution improvement achieved post-injection. Importantly, the vital organ tissue samples of the mice showed no acute toxicity or inflammation in response to injection.[40]

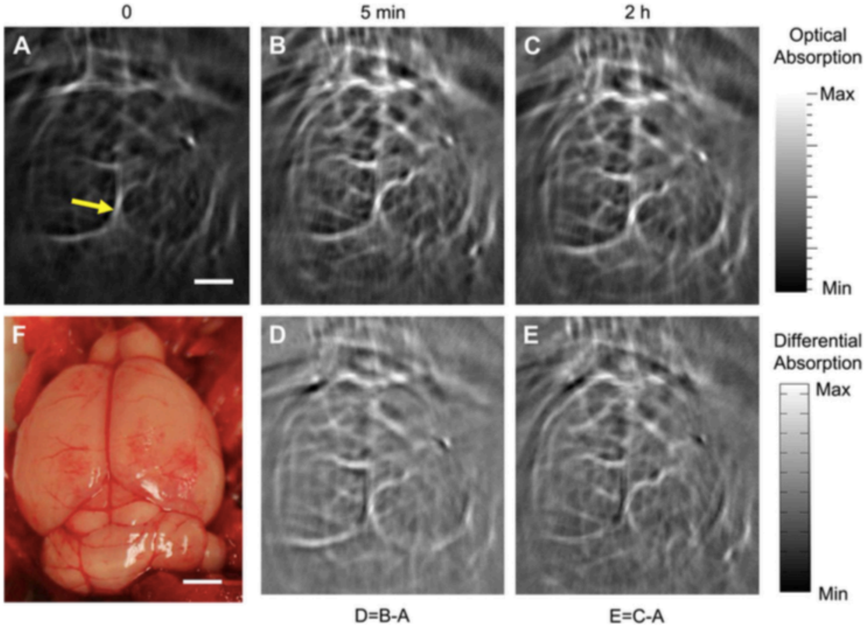

Figure 1-5) Noninvasive PAT imaging of a mouse brain in vivo employing PEG-HGN and NIR light at a wavelength of 800 nm. Photoacoustic image acquired (A) before injection, (B) 5 min after injection, and (C) 2 h after the intravenous injection of PEG-HGN. (D) and (E) Differential images that were obtained by subtracting the pre-injection image from the post-injection images (F) Open-skull photograph of the mouse brain cortex obtained after the data acquisition for PAT. Bar = 2 mm.

Gold nanorods with aspect ratios 3 and 4 are reported to provide better contrast than HGNs because of higher optical scattering.[37] However, it is possible to tune the scattering and absorption properties of HGNs by changing the size and surface morphology.[21] Moreover, though untested, spikey and bumpy HGNs are likely strong contrast agent candidates. However, while HGNs can be used to produce relatively detailed images, the real improvement made to photoacoustic imaging with HGNs is in the combination with other techniques, as discussed in the following section.

1.4.2 Theranostics

The photothermal effect, based on light to heat conversion, is the foundation for several theranostics and combinative therapy approaches. In photothermal therapy (PTT), metal particles with strong light absorption, ideally in the NIR region, are conjugated with targeting molecules, such as antibodies, that can bind to antigens on tumor cell surface. Upon illumination with light, the particles absorb light and convert it into heat, which induces hyperthermia in the cells.[89]

Effective PTT requires the use of particles that are biologically compatible, easily functionalized, and easy to deliver, with strong NIR optical adsorption and high photothermal conversion.[41] HGNs benefit from the ease of functionalization associated with all gold nanoparticles and can be successfully attached to a biological linker that will bind to an overexpressed receptor[27,42,90,91]. Typically binding is done with small peptides[43] or antibodies,[92] and now DNA oligonucleotide aptamers that bind to a receptor on a cell of diseased tissue.[42] HGNs can also be linked to diseased tissue by encapsulating them inside of micellular structures to be accepted and internalized into a cell.[93,94] The strong, narrow emission in the NIR window, resulting from its spherical shape, lead to more efficient photothermal effect than gold nanorods and nanocages.[41]

While PTT has proven effective, tumor cells have defense mechanisms that prevent cell death during hyperthermia. Heat shock proteins are overexpressed in response to lethal heat and allow cells to resist hyperthermia.[43] Therefore, the efficacy of PTT is often improved by combining it with other therapies. A common coupling is photothermal therapy with drug delivery or gene silencing. In these techniques, particles are coated with a cancer therapy drugs or small interfering RNA (siRNA) that are released when particles are irradiated with laser light. Thus, heat induced destruction of tumors is combined with targeted drug release or gene silencing therapy.[26,28,43,86,94,95] While this technique works with solid particles, the hollow cavity and subsequent increased surface area of HGNs are highly advantageous. HGNs can load pharmaceuticals on both their interior and exterior surfaces, increasing the drug delivery load significantly. A number of therapeutics have been photothermally released from the surfaces of HGNs, including but not limited to doxorubicin (DOX),[28,90] paxlitacel,[94] chlorin,[95] and small interfering RNA (siRNA).[43,86] You *et al*. achieved a 3.5-fold increase in drug loading of DOX when compared to solid gold particles. While the HGNs' release of DOX could readily be controlled using a NIR laser, the gold nanoparticles did not release any DOX in response to NIR light. By combining targeted hyperthermia with effective loading and release of DOX, melanoma cell apoptosis was greatly increased. PTT alone resulted in 40.6% cell apoptosis, while the combination more than doubled the outcome, resulting in 86.4% cell death.[90]

The same technique can be applied for gene silencing. SiRNA silence the generation of heat-shock proteins that protect tumors from hyperthermia. Wang *et al*. conducted in vitro and in vivo studies combining PTT and controlled release of siRNA. In vitro studies conducted on glioma tumor cells determined that introducing siRNA therapy with photothermal therapy resulted in more rapid temperature elevation. This will allow for shorter, more effective treatments. Moreover, the temperature to induce cell death was lowered by ~2 degrees to 48°C with the addition of siRNA resulting in less collateral damage of surrounding tissue. The in vivo effects of PTT gene silencing treatment were monitored with fluorescent imaging over a period of 24 hours showing the retention of siRNA conjugated HGNs and improved fluorescence over unconjugated ones (Figure 1-6a). Infrared thermal images of glioma tumor bearing nude mice after PTT were taken using siRNA conjugated HGNs and unconjugated HGNs. It was confirmed that temperature rapidly raised to 46.4°C in 8 minutes, while unconjugated HGNs only reached 39.6°C (Figure 1-6c). Moreover, mice treated with PTT and gene silencing therapy showed a 70% increase survival rate when compared to those that did not receive treatment.[43] HGNs are well-suited substrates for this therapy due their larger surface area, high photothermal effect, and combinative therapy capabilities.[43]

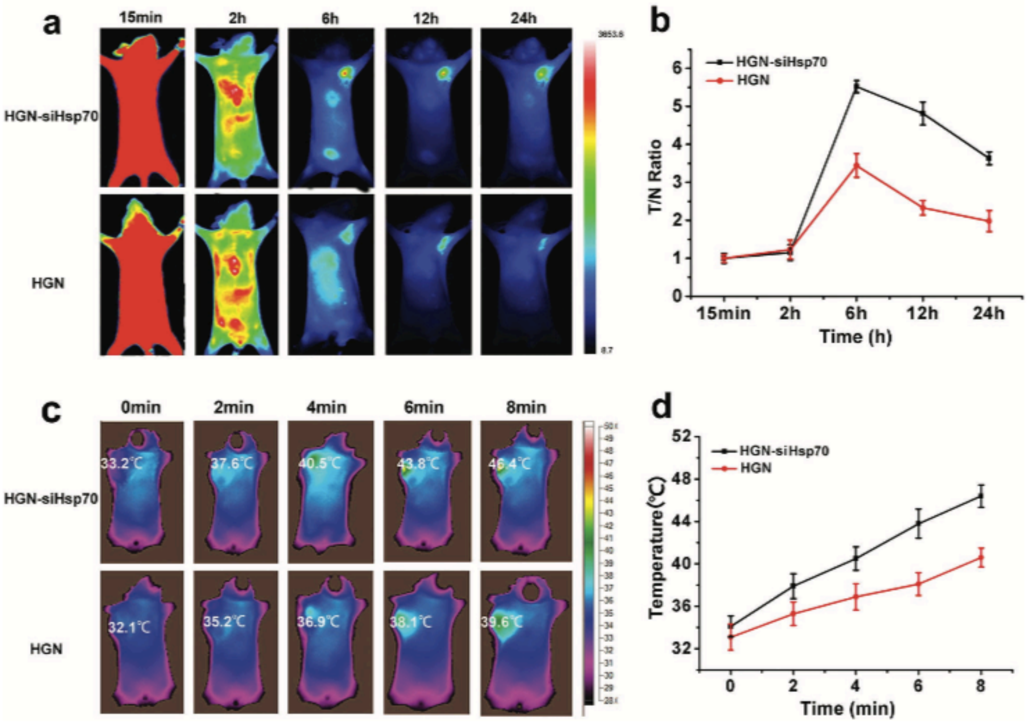

Figure 1-6) In vivo biodistribution and photothermal effects of HGNs and siRNA conjugated HGNs (HGN-siHsp70). a) Fluorescence imaging of HGN-siHsp70 and HGN at 15 min, 2 h, 6 h, 12 h, and 24 h after intravenous injection. b) Tumor to normal tissue ratios of glioma tumor bearing mice at different time points after injection. c) Infrared thermal images of glioma tumor bearing mice i.v. injected with HGN and HGN-siHsp70 within 8 min under 765 nm laser irradiation. d) Temperature changes on tumor sites according to the imaging in (c).[96]

Finally, many studies have highlighted the impressive multimodal capabilities of HGNs.[27,29,44] While Wang et al. was able to use HGNs for PTT, targeted gene silencing treatment, and fluorescent imaging, it is possible to go further and simultaneously use photoacoustic imaging.[96] Lee *et al*. utilized fluorescence imaging, photoacoustic imaging, photothermal therapy, and targeted drug delivery of DOX in the same study. DOX conjugated HGNs were injected into murine tumor bearing mice. HGNs were used to enhance fluorescent images taken of the mice. Additionally, since HGNs exhibit the photoacoustic effect, which is dependent on temperature, they can be used to take temperature measurements. During PTT, the temperature was raised from 37°C to 50°C and NIR laser light was used to simultaneously control the release of DOX. This resulted in 64% cell death compared to the 7% cell death of the untreated tumors. In this way, imaging and temperature measurements were done concurrently to monitor the efficacy of treatment.[27] These measurements have traditionally required invasive insertion of a thermocouple to measure temperature and expensive MRI imaging. This underlines the outstanding multimodal capabilities HGNs.

However, HGNs are capable of more than just photoacoustic imaging and fluorescent imaging. In a study done by *Vickers et al.,* HGNs were used for both two photon photoluminescence (2PPL) and photothermal therapy.[44] Two photon photoluminescence is used in high resolution imaging, especially of biological tissues, because of the quadratic dependence of absorption on excitation intensity.[97] The traditional substrates for this technique have drawbacks; organic dyes have poor photostability[98] and quantum dots are prone to photoblinking[99] and high cytotoxicity.[100] Gold substrates are highly photostable, do not exhibit photoblinking, are non-cytotoxic, and have large two-photon cross section.[44] While gold nanorods are commonly used for their two photon action cross sections from the "lightning rod effect",[101,102] Vickers *et al.* conducted in vitro studies on HeLa cervical cancer cells and demonstrated an impressive, estimated 1.5×10^{-4} 2PPL quantum yield, greater than what has been reported for gold nanorods,[103] using HGNs.[44] Moreover, the fine control over the synthesis of HGNs allowed them to determine that while thicker shelled particles with blue-shifted absorptions had a higher two photon photoluminescence cross sections, 820 nm NIR absorbing particles still had higher cross sections than gold nanorods. In addition to multiphoton microscopy, the HGNs also administered highly targeted and effective photothermal treatment while requiring less laser exposure and shorter power density than gold nanorods.[44]

While many theranostic studies have been conducted with smooth HGNs, there is great potential for bumpy and spikey HGNs. Lindley *et al*. synthesized bumpy HGNs and demonstrated experimentally and theoretically that smooth and bumpy particles with identical radius of their inner cavities produced the same amount of heat when irradiated. Smooth HGNs had 99% photothermal conversion efficiency while bumpy HGNs had 96-97% photothermal conversion efficiency, which are among the highest reported for gold structures in literature.[29,104–106] Thus, the highly effective light-to-heat converting capabilities of HGNs are not diminished by changing their surface morphology. Moreover, bumpy particles have higher surface area for drug loading, making them excellent candidates for theranostics.[29]

1.5 Summary

Hollow gold nanospheres have strong, narrow, tunable surface plasmon resonance to the near infrared window, enhanced electromagnetic fields due to their solvent filled inner cavity, high photothermal conversion, low cytoxicity, and are easily functionalized. Recent developments in the precise synthetic control over their size, shell thickness, and surface morphology have allowed greater control of their optical and surface properties leading to growing use in the fields of biomedical research. HGNs have been established as highly attractive plasmonic structures for refractive index sensing, SERS, imaging, photothermal therapy, drug delivery, and theranostics. While smooth NIR light absorbing particles have dominated most fields, bumpy and spikey particles are starting to find their uses in the fields of SERS and PTA. HGNs remain a novel and important tool in the field of nanotherapeutics and diagnostics.

1.6 References

(1) Adams, S.; Zhang, J. Z. Unique Optical Properties and Applications of Hollow Gold Nanospheres (HGNs). *Coord. Chem. Rev.* **2016**, *320–321*, 18–37. https://doi.org/10.1016/j.ccr.2016.01.014.

(2) Hergert, W.; Wriedt, T. *The Mie Theory: Basics and Applications*; Springer, 2012.

(3) Li, X.; Choy, W. C. H.; Lu, H.; Sha, W. E. I.; Ho, A. H. P. Efficiency Enhancement of Organic Solar Cells by Using Shape-Dependent Broadband Plasmonic Absorption in Metallic Nanoparticles. *Adv. Funct. Mater.* **2013**, *23* (21), 2728–2735. https://doi.org/10.1002/adfm.201202476.

(4) Grzelczak, M.; M. Liz-Marzán, L. The Relevance of Light in the Formation of Colloidal Metal Nanoparticles. *Chem. Soc. Rev.* **2014**, *43* (7), 2089–2097. https://doi.org/10.1039/C3CS60256G.

(5) Kolwas, K.; Derkachova, A. Damping Rates of Surface Plasmons for Particles of Size from Nano- to Micrometers; Reduction of the Nonradiative Decay. *J. Quant. Spectrosc. Radiat. Transf.* **2013**, *114*, 45–55. https://doi.org/10.1016/j.jqsrt.2012.08.007.

(6) Link, S.; El-Sayed, M. A. Size and Temperature Dependence of the Plasmon Absorption of Colloidal Gold Nanoparticles. *J. Phys. Chem. B* **1999**, *103* (21), 4212–4217. https://doi.org/10.1021/jp984796o.

(7) Miller, M. M.; Lazarides, A. A. Sensitivity of Metal Nanoparticle Surface Plasmon Resonance to the Dielectric Environment. *J. Phys. Chem. B* **2005**, *109* (46), 21556–21565. https://doi.org/10.1021/jp054227y.

(8) Shukla, R.; Bansal, V.; Chaudhary, M.; Basu, A.; Bhonde, R. R.; Sastry, M. Biocompatibility of Gold Nanoparticles and Their Endocytotic Fate Inside the Cellular Compartment: A Microscopic Overview. *Langmuir* **2005**, *21* (23), 10644–10654. https://doi.org/10.1021/la0513712.

(9) Lee, S.; Chon, H.; Lee, M.; Choo, J.; Shin, S. Y.; Lee, Y. H.; Rhyu, I. J.; Son, S. W.; Oh, C. H. Surface-Enhanced Raman Scattering Imaging of HER2 Cancer Markers Overexpressed in Single MCF7 Cells Using Antibody Conjugated Hollow Gold Nanospheres. *Biosens. Bioelectron.* **2009**, *24* (7), 2260–2263. https://doi.org/10.1016/j.bios.2008.10.018.

(10) Lee, J. H.; Jeong, H. S.; Lee, D. H.; Beack, S.; Kim, T.; Lee, G.-H.; Park, W. C.; Kim, C.; Kim, K. S.; Hahn, S. K. Targeted Hyaluronate–Hollow Gold Nanosphere

Conjugate for Anti-Obesity Photothermal Lipolysis. *ACS Biomater. Sci. Eng.* **2017**, *3* (12), 3646–3653. https://doi.org/10.1021/acsbiomaterials.7b00549.

(11) Luo, J.; Cheng, Y.; He, X.-Y.; Liu, Y.; Peng, N.; Gong, Z.-W.; Wu, K.; Zou, T. Self-Assembled CpG Oligodeoxynucleotides Conjugated Hollow Gold Nanospheres to Enhance Cancer-Associated Immunostimulation. *Colloids Surf. B Biointerfaces* **2019**, *175*, 248–255. https://doi.org/10.1016/j.colsurfb.2018.12.001.

(12) You, J.; Zhou, J.; Zhou, M.; Liu, Y.; Robertson, J. D.; Liang, D.; Van Pelt, C.; Li, C. Pharmacokinetics, Clearance, and Biosafety of Polyethylene Glycol-Coated Hollow Gold Nanospheres. *Part. Fibre Toxicol.* **2014**, *11* (1), 26. https://doi.org/10.1186/1743-8977-11-26.

(13) Guan, G.; Win, K. Y.; Yao, X.; Yang, W.; Han, M.-Y. Plasmonically Modulated Gold Nanostructures for Photothermal Ablation of Bacteria. *Adv. Healthc. Mater.* *n/a* (n/a), 2001158. https://doi.org/10.1002/adhm.202001158.

(14) Ren, X.; Tan, E.; Lang, X.; You, T.; Jiang, L.; Zhang, H.; Yin, P.; Guo, L. Observing Reduction of 4-Nitrobenzenthiol on Gold Nanoparticles in Situ Using Surface-Enhanced Raman Spectroscopy. *Phys. Chem. Chem. Phys.* **2013**, *15* (34), 14196–14201. https://doi.org/10.1039/C3CP51385H.

(15) Shimizu, T.; Teranishi, T.; Hasegawa, S.; Miyake, M. Size Evolution of Alkanethiol-Protected Gold Nanoparticles by Heat Treatment in the Solid State. *J. Phys. Chem. B* **2003**, *107* (12), 2719–2724. https://doi.org/10.1021/jp026920g.

(16) Jiang, Y.; Li, J.; Zhen, X.; Xie, C.; Pu, K. Dual-Peak Absorbing Semiconducting Copolymer Nanoparticles for First and Second Near-Infrared

Window Photothermal Therapy: A Comparative Study. *Adv. Mater.* **2018**, *30* (14), 1705980. https://doi.org/10.1002/adma.201705980.

(17) Zheng, J.; Yang, W.; Wang, J.; Zhu, J.; Qian, L.; Yang, Z. An Ultranarrow SPR Linewidth in the UV Region for Plasmonic Sensing. *Nanoscale* **2019**, *11* (9), 4061–4066. https://doi.org/10.1039/C8NR09703H.

(18) Zhang, J. Z. Biomedical Applications of Shape-Controlled Plasmonic Nanostructures: A Case Study of Hollow Gold Nanospheres for Photothermal Ablation Therapy of Cancer. *J. Phys. Chem. Lett.* **2010**, *1* (4), 686–695. https://doi.org/10.1021/jz900366c.

(19) Lindley, S. A.; Cooper, J. K.; Rojas-Andrade, M. D.; Fung, V.; Leahy, C. J.; Chen, S.; Zhang, J. Z. Highly Tunable Hollow Gold Nanospheres: Gaining Size Control and Uniform Galvanic Exchange of Sacrificial Cobalt Boride Scaffolds. *ACS Appl. Mater. Interfaces* **2018**, *10* (15), 12992–13001. https://doi.org/10.1021/acsami.8b00726.

(20) Xie, H.; A. Larmour, I.; Chen, Y.-C.; W. Wark, A.; Tileli, V.; W. McComb, D.; Faulds, K.; Graham, D. Synthesis and NIR Optical Properties of Hollow Gold Nanospheres with LSPR Greater than One Micrometer. *Nanoscale* **2013**, *5* (2), 765–771. https://doi.org/10.1039/C2NR33187J.

(21) Pu, Y.-C.; Song, F.; Zhang, W.; Lindley, S.; Adams, S.; Zhang, J. Z. Size-Tunable Synthesis of Hollow Gold Nanospheres through Control of Reaction Temperature. *Part. Part. Syst. Charact.* **2017**, *34* (8), 1600255. https://doi.org/10.1002/ppsc.201600255.

(22) Schwartzberg, A. M.; Olson, T. Y.; Talley, C. E.; Zhang, J. Z. Synthesis, Characterization, and Tunable Optical Properties of Hollow Gold Nanospheres. *J. Phys. Chem. B* **2006**, *110* (40), 19935–19944. https://doi.org/10.1021/jp062136a.

(23) Adams, S.; Thai, D.; Mascona, X.; Schwartzberg, A. M.; Zhang, J. Z. Key Factors Affecting the Reproducibility of Synthesis and Growth Mechanism of Near-Infrared Absorbing Hollow Gold Nanospheres. *Chem. Mater.* **2014**, *26* (23), 6805–6810. https://doi.org/10.1021/cm5033892.

(24) Mahmoud, M. A.; Snyder, B.; El-Sayed, M. A. Surface Plasmon Fields and Coupling in the Hollow Gold Nanoparticles and Surface-Enhanced Raman Spectroscopy. Theory and Experiment. *J. Phys. Chem. C* **2010**, *114* (16), 7436–7443. https://doi.org/10.1021/jp9109018.

(25) Sun, Y.; Xia, Y. Increased Sensitivity of Surface Plasmon Resonance of Gold Nanoshells Compared to That of Gold Solid Colloids in Response to Environmental Changes. *Anal. Chem.* **2002**, *74* (20), 5297–5305. https://doi.org/10.1021/ac0258352.

(26) You, J.; Zhang, G.; Li, C. Exceptionally High Payload of Doxorubicin in Hollow Gold Nanospheres for Near-Infrared Light-Triggered Drug Release. *ACS Nano* **2010**, *4* (2), 1033–1041. https://doi.org/10.1021/nn901181c.

(27) Lee, H. J.; Liu, Y.; Zhao, J.; Zhou, M.; Bouchard, R. R.; Mitcham, T.; Wallace, M.; Stafford, R. J.; Li, C.; Gupta, S.; Melancon, M. P. In Vitro and in Vivo Mapping of Drug Release after Laser Ablation Thermal Therapy with Doxorubicin-Loaded Hollow Gold Nanoshells Using Fluorescence and Photoacoustic Imaging. *J.*

Controlled Release **2013**, *172* (1), 152–158. https://doi.org/10.1016/j.jconrel.2013.07.020.

(28) You, J.; Zhang, R.; Zhang, G.; Zhong, M.; Liu, Y.; Van Pelt, C. S.; Liang, D.; Wei, W.; Sood, A. K.; Li, C. Photothermal-Chemotherapy with Doxorubicin-Loaded Hollow Gold Nanospheres: A Platform for near-Infrared Light-Trigged Drug Release. *J. Controlled Release* **2012**, *158* (2), 319–328. https://doi.org/10.1016/j.jconrel.2011.10.028.

(29) Lindley, S. A.; Zhang, J. Z. Bumpy Hollow Gold Nanospheres for Theranostic Applications: Effect of Surface Morphology on Photothermal Conversion Efficiency. *ACS Appl. Nano Mater.* **2019**, *2* (2), 1072–1081. https://doi.org/10.1021/acsanm.8b02331.

(30) Sanchez-Gaytan, B. L.; Park, S.-J. Spiky Gold Nanoshells. *Langmuir* **2010**, *26* (24), 19170–19174. https://doi.org/10.1021/la1038969.

(31) Li, S.; Wu, Q.; Ma, P.; Zhang, Y.; Song, D.; Wang, X.; Sun, Y. A Sensitive SPR Biosensor Based on Hollow Gold Nanospheres and Improved Sandwich Assay with PDA-Ag@Fe3O4/RGO. *Talanta* **2018**, *180*, 156–161. https://doi.org/10.1016/j.talanta.2017.12.051.

(32) Mahmoud, M. A.; El-Sayed, M. A. Gold Nanoframes: Very High Surface Plasmon Fields and Excellent Near-Infrared Sensors. *J. Am. Chem. Soc.* **2010**, *132* (36), 12704–12710. https://doi.org/10.1021/ja104532z.

(33) Tu, M. H.; Sun, T.; Grattan, K. T. V. LSPR Optical Fibre Sensors Based on Hollow Gold Nanostructures. *Sens. Actuators B Chem.* **2014**, *191*, 37–44. https://doi.org/10.1016/j.snb.2013.09.094.

(34) Wang, Y.; Zhao, P.; Mao, L.; Hou, Y.; Li, D. Determination of Brain Injury Biomarkers by Surface-Enhanced Raman Scattering Using Hollow Gold Nanospheres. *RSC Adv.* **2018**, *8* (6), 3143–3150. https://doi.org/10.1039/C7RA12410D.

(35) Choi, N.; Dang, H.; Das, A.; Sim, M. S.; Chung, I. Y.; Choo, J. SERS Biosensors for Ultrasensitive Detection of Multiple Biomarkers Expressed in Cancer Cells. *Biosens. Bioelectron.* **2020**, *164*, 112326. https://doi.org/10.1016/j.bios.2020.112326.

(36) Xie, H.; Larmour, I. A.; Smith, W. E.; Faulds, K.; Graham, D. Surface-Enhanced Raman Scattering Investigation of Hollow Gold Nanospheres. *J. Phys. Chem. C* **2012**, *116* (14), 8338–8342. https://doi.org/10.1021/jp3014089.

(37) Li, W.; Chen, X. Gold Nanoparticles for Photoacoustic Imaging. *Nanomed.* **2015**, *10* (2), 299–320. https://doi.org/10.2217/nnm.14.169.

(38) Fu, Q.; Zhu, R.; Song, J.; Yang, H.; Chen, X. Photoacoustic Imaging: Contrast Agents and Their Biomedical Applications. *Adv. Mater.* **2019**, *31* (6), 1805875. https://doi.org/10.1002/adma.201805875.

(39) Rouleau, L.; Berti, R.; Ng, V. W. K.; Matteau-Pelletier, C.; Lam, T.; Saboural, P.; Kakkar, A. K.; Lesage, F.; Rhéaume, E.; Tardif, J.-C. VCAM-1-Targeting Gold

Nanoshell Probe for Photoacoustic Imaging of Atherosclerotic Plaque in Mice. *Contrast Media Mol. Imaging* **2013**, *8* (1), 27–39. https://doi.org/10.1002/cmmi.1491.

(40) Lu, W.; Huang, Q.; Ku, G.; Wen, X.; Zhou, M.; Guzatov, D.; Brecht, P.; Su, R.; Oraevsky, A.; Wang, L. V.; Li, C. Photoacoustic Imaging of Living Mouse Brain Vasculature Using Hollow Gold Nanospheres. *Biomaterials* **2010**, *31* (9), 2617–2626. https://doi.org/10.1016/j.biomaterials.2009.12.007.

(41) Zhang, J. Z. Biomedical Applications of Shape-Controlled Plasmonic Nanostructures: A Case Study of Hollow Gold Nanospheres for Photothermal Ablation Therapy of Cancer. *J Phys Chem Lett* **2010**, 10.

(42) Grabowska-Jadach, I.; Kalinowska, D.; Drozd, M.; Pietrzak, M. Synthesis, Characterization and Application of Plasmonic Hollow Gold Nanoshells in a Photothermal Therapy—New Particles for Theranostics. *Biomed. Pharmacother.* **2019**, *111*, 1147–1155. https://doi.org/10.1016/j.biopha.2019.01.037.

(43) Wang, Z.; Li, S.; Zhang, M.; Ma, Y.; Liu, Y.; Gao, W.; Zhang, J.; Gu, Y. Laser-Triggered Small Interfering RNA Releasing Gold Nanoshells against Heat Shock Protein for Sensitized Photothermal Therapy. *Adv. Sci.* **2017**, *4* (2), 1600327. https://doi.org/10.1002/advs.201600327.

(44) Vickers, E. T.; Garai, M.; Bonabi Naghadeh, S.; Lindley, S.; Hibbs, J.; Xu, Q.-H.; Zhang, J. Z. Two-Photon Photoluminescence and Photothermal Properties of Hollow Gold Nanospheres for Efficient Theranostic Applications. *J. Phys. Chem. C* **2018**, *122* (25), 13304–13313. https://doi.org/10.1021/acs.jpcc.7b09055.

(45) Chee, S. W.; Tan, S. F.; Baraissov, Z.; Bosman, M.; Mirsaidov, U. Direct Observation of the Nanoscale Kirkendall Effect during Galvanic Replacement Reactions. *Nat. Commun.* **2017**, *8* (1), 1224. https://doi.org/10.1038/s41467-017-01175-2.

(46) Prevo, B. G.; Esakoff, S. A.; Mikhailovsky, A.; Zasadzinski, J. A. Scalable Routes to Gold Nanoshells with Tunable Sizes and Response to Near-Infrared Pulsed-Laser Irradiation. *Small* **2008**, *4* (8), 1183–1195. https://doi.org/10.1002/smll.200701290.

(47) Zhang, Z.-S.; Yang, Z.-J.; Liu, X.-L.; Li, M.; Zhou, L. Multiple Plasmon Resonances of Au/Ag Alloyed Hollow Nanoshells. *Scr. Mater.* **2010**, *63* (12), 1193–1196. https://doi.org/10.1016/j.scriptamat.2010.08.037.

(48) Masa, J.; Weide, P.; Peeters, D.; Sinev, I.; Xia, W.; Sun, Z.; Somsen, C.; Muhler, M.; Schuhmann, W. Amorphous Cobalt Boride (Co2B) as a Highly Efficient Nonprecious Catalyst for Electrochemical Water Splitting: Oxygen and Hydrogen Evolution. *Adv. Energy Mater.* **2016**, *6* (6), 1502313. https://doi.org/10.1002/aenm.201502313.

(49) Glavee, G. N.; Klabunde, K. J.; Sorensen, C. M.; Hadjipanayis, G. C. Borohydride Reduction of Cobalt Ions in Water. Chemistry Leading to Nanoscale Metal, Boride, or Borate Particles. *Langmuir* **1993**, *9* (1), 162–169. https://doi.org/10.1021/la00025a034.

(50) 11.2: Standard Reduction Potential https://chem.libretexts.org/Bookshelves/General_Chemistry/Map%3A_Chemistry_(Z

umdahl_and_Decoste)/11%3A_Electrochemistry/11.2%3A_Standard_Reduction_Potential (accessed Nov 20, 2020).

(51) Rodriguez-Montelongo, S. A.; Gonzalez-Hernandez, J.; Macias, A. H.; Silva-Ramirez, A. S.; Castillo Martin del Campo, C. G.; Gutierrez-Hernandez, J. M.; Ruiz, F.; Gonzalez-Ortega, O. Synthesis, Characterization, and Toxicity of Hollow Gold Nanoshells. *J. Nanoparticle Res.* **2018**, *20* (11), 311. https://doi.org/10.1007/s11051-018-4420-2.

(52) Preciado-Flores, S.; Wang, D.; A. Wheeler, D.; Newhouse, R.; K. Hensel, J.; Schwartzberg, A.; Wang, L.; Zhu, J.; Barboza-Flores, M.; Z. Zhang, J. Highly Reproducible Synthesis of Hollow Gold Nanospheres with near Infrared Surface Plasmon Absorption Using PVP as Stabilizing Agent. *J. Mater. Chem.* **2011**, *21* (7), 2344–2350. https://doi.org/10.1039/C0JM03690K.

(53) LaMer, V. K.; Dinegar, R. H. Theory, Production and Mechanism of Formation of Monodispersed Hydrosols. *J. Am. Chem. Soc.* **1950**, *72* (11), 4847–4854. https://doi.org/10.1021/ja01167a001.

(54) Houk, L. R.; Challa, S. R.; Grayson, B.; Fanson, P.; Datye, A. K. The Definition of "Critical Radius" for a Collection of Nanoparticles Undergoing Ostwald Ripening. *Langmuir* **2009**, *25* (19), 11225–11227. https://doi.org/10.1021/la902263s.

(55) Glavee, G. N.; Klabunde, K. J.; Sorensen, C. M.; Hadjapanayis, G. C. Borohydride Reductions of Metal Ions. A New Understanding of the Chemistry Leading to Nanoscale Particles of Metals, Borides, and Metal Borates. *Langmuir* **1992**, *8* (3), 771–773. https://doi.org/10.1021/la00039a008.

(56) Melancon, M. P.; Zhou, M.; Li, C. Cancer Theranostics with Near-Infrared Light-Activatable Multimodal Nanoparticles. *Acc. Chem. Res.* **2011**, *44* (10), 947–956. https://doi.org/10.1021/ar200022e.

(57) Petit, C.; Pileni, M. P. Nanosize Cobalt Boride Particles: Control of the Size and Properties. *J. Magn. Magn. Mater.* **1997**, *166* (1), 82–90. https://doi.org/10.1016/S0304-8853(96)00621-X.

(58) Thibodeaux, C. A.; Kulkarni, V.; Chang, W.-S.; Neumann, O.; Cao, Y.; Brinson, B.; Ayala-Orozco, C.; Chen, C.-W.; Morosan, E.; Link, S.; Nordlander, P.; Halas, N. J. Impurity-Induced Plasmon Damping in Individual Cobalt-Doped Hollow Au Nanoshells. *J. Phys. Chem. B* **2014**, *118* (49), 14056–14061. https://doi.org/10.1021/jp504467j.

(59) Morgan, E.; Wupperfeld, D.; Morales, D.; Reich, N. Shape Matters: Gold Nanoparticle Shape Impacts the Biological Activity of SiRNA Delivery. *Bioconjug. Chem.* **2019**, *30* (3), 853–860. https://doi.org/10.1021/acs.bioconjchem.9b00004.

(60) Yue, J.; Feliciano, T. J.; Li, W.; Lee, A.; Odom, T. W. Gold Nanoparticle Size and Shape Effects on Cellular Uptake and Intracellular Distribution of SiRNA Nanoconstructs. *Bioconjug. Chem.* **2017**, *28* (6), 1791–1800. https://doi.org/10.1021/acs.bioconjchem.7b00252.

(61) Grzelczak, M.; M. Liz-Marzán, L. The Relevance of Light in the Formation of Colloidal Metal Nanoparticles. *Chem. Soc. Rev.* **2014**, *43* (7), 2089–2097. https://doi.org/10.1039/C3CS60256G.

(62) CFD-Nucleation.Pdf.

(63) Barnes, W. L. Particle Plasmons: Why Shape Matters. *Am. J. Phys.* **2016**, *84* (8), 593–601. https://doi.org/10.1119/1.4948402.

(64) Shabaninezhad, M.; Ramakrishna, G. Theoretical Investigation of Size, Shape, and Aspect Ratio Effect on the LSPR Sensitivity of Hollow-Gold Nanoshells. *J. Chem. Phys.* **2019**, *150* (14), 144116. https://doi.org/10.1063/1.5090885.

(65) Controlling the Topography and Surface Plasmon Resonance of Gold Nanoshells by a Templated Surfactant-Assisted Seed Growth Method | The Journal of Physical Chemistry C https://pubs.acs.org/doi/abs/10.1021/jp401189k (accessed Oct 28, 2020).

(66) Sanchez-Gaytan, B. L.; Qian, Z.; Hastings, S. P.; Reca, M. L.; Fakhraai, Z.; Park, S.-J. Controlling the Topography and Surface Plasmon Resonance of Gold Nanoshells by a Templated Surfactant-Assisted Seed Growth Method. *J. Phys. Chem. C* **2013**, *117* (17), 8916–8923. https://doi.org/10.1021/jp401189k.

(67) Sanchez-Gaytan, B. L.; Swanglap, P.; Lamkin, T. J.; Hickey, R. J.; Fakhraai, Z.; Link, S.; Park, S.-J. Spiky Gold Nanoshells: Synthesis and Enhanced Scattering Properties. *J. Phys. Chem. C* **2012**, *116* (18), 10318–10324. https://doi.org/10.1021/jp300009b.

(68) Gagner, J. E.; Lopez, M. D.; Dordick, J. S.; Siegel, R. W. Effect of Gold Nanoparticle Morphology on Adsorbed Protein Structure and Function. *Biomaterials* **2011**, *32* (29), 7241–7252. https://doi.org/10.1016/j.biomaterials.2011.05.091.

(69) S. Levy, E.; P. Morales, D.; V. Garcia, J.; O. Reich, N.; C. Ford, P. Near-IR Mediated Intracellular Uncaging of NO from Cell Targeted Hollow Gold

Nanoparticles. *Chem. Commun.* **2015**, *51* (100), 17692–17695. https://doi.org/10.1039/C5CC07989F.

(70) Barbosa, S.; Agrawal, A.; Rodríguez-Lorenzo, L.; Pastoriza-Santos, I.; Alvarez-Puebla, R. A.; Kornowski, A.; Weller, H.; Liz-Marzán, L. M. Tuning Size and Sensing Properties in Colloidal Gold Nanostars. *Langmuir* **2010**, *26* (18), 14943–14950. https://doi.org/10.1021/la102559e.

(71) Mayer, K. M.; Hafner, J. H. Localized Surface Plasmon Resonance Sensors. *Chem. Rev.* **2011**, *111* (6), 3828–3857. https://doi.org/10.1021/cr100313v.

(72) Tuersun, P. Optimizing the Figure of Merit of Gold Nanoshell-Based Refractive Index Sensing. *Optik* **2016**, *127* (1), 250–253. https://doi.org/10.1016/j.ijleo.2015.10.069.

(73) White, I. M.; Fan, X. On the Performance Quantification of Resonant Refractive Index Sensors. *Opt. Express* **2008**, *16* (2), 1020–1028.

(74) Baker, J. E.; Sriram, R.; Miller, B. L. Two-Dimensional Photonic Crystals for Sensitive Microscale Chemical and Biochemical Sensing. *Lab. Chip* **2015**, *15* (4), 971–990. https://doi.org/10.1039/c4lc01208a.

(75) Kim, H.-M.; Hong Jeong, D.; Lee, H.-Y.; Park, J.-H.; Lee, S.-K. Improved Stability of Gold Nanoparticles on the Optical Fiber and Their Application to Refractive Index Sensor Based on Localized Surface Plasmon Resonance. *Opt. Laser Technol.* **2019**, *114*, 171–178. https://doi.org/10.1016/j.optlastec.2019.02.002.

(76) M. Pallares, R.; Stilson, T.; Choo, P.; Hu, J.; Odom, T. W. Using Good’s Buffers To Control the Anisotropic Structure and Optical Properties of Spiky Gold

Nanoparticles for Refractive Index Sensing. *ACS Appl. Nano Mater.* **2019**, *2* (8), 5266–5271. https://doi.org/10.1021/acsanm.9b01117.

(77) Stiles, P. L.; Dieringer, J. A.; Shah, N. C.; Van Duyne, R. P. Surface-Enhanced Raman Spectroscopy. *Annu. Rev. Anal. Chem.* **2008**, *1* (1), 601–626. https://doi.org/10.1146/annurev.anchem.1.031207.112814.

(78) Guo, M.; Dong, J.; Xie, W.; Tao, L.; Lu, W.; Wang, Y.; Qian, W. SERS Tags-Based Novel Monodispersed Hollow Gold Nanospheres for Highly Sensitive Immunoassay of CEA. *J. Mater. Sci.* **2015**, *50* (9), 3329–3336. https://doi.org/10.1007/s10853-015-8825-3.

(79) Schwartzberg, A. M.; Oshiro, T. Y.; Zhang, J. Z.; Huser, T.; Talley, C. E. Improving Nanoprobes Using Surface-Enhanced Raman Scattering from 30-Nm Hollow Gold Particles. *Anal. Chem.* **2006**, *78* (13), 4732–4736. https://doi.org/10.1021/ac060220g.

(80) Carlini, L.; Fasolato, C.; Postorino, P.; Fratoddi, I.; Venditti, I.; Testa, G.; Battocchio, C. Comparison between Silver and Gold Nanoparticles Stabilized with Negatively Charged Hydrophilic Thiols: SR-XPS and SERS as Probes for Structural Differences and Similarities. *Colloids Surf. Physicochem. Eng. Asp.* **2017**, *532*, 183–188. https://doi.org/10.1016/j.colsurfa.2017.05.045.

(81) Huang, G. G.; Han, X. X.; Hossain, M. K.; Ozaki, Y. Development of a Heat-Induced Surface-Enhanced Raman Scattering Sensing Method for Rapid Detection of Glutathione in Aqueous Solutions. *Anal. Chem.* **2009**, *81* (14), 5881–5888. https://doi.org/10.1021/ac900392s.

(82) Ru, E. C. L.; A. Meyer, S.; Artur, C.; G. Etchegoin, P.; Grand, J.; Lang, P.; Maurel, F. Experimental Demonstration of Surface Selection Rules for SERS on Flat Metallic Surfaces. *Chem. Commun.* **2011**, *47* (13), 3903–3905. https://doi.org/10.1039/C1CC10484E.

(83) Lee, S.; Chon, H.; Lee, J.; Ko, J.; Chung, B. H.; Lim, D. W.; Choo, J. Rapid and Sensitive Phenotypic Marker Detection on Breast Cancer Cells Using Surface-Enhanced Raman Scattering (SERS) Imaging. *Biosens. Bioelectron.* **2014**, *51*, 238–243. https://doi.org/10.1016/j.bios.2013.07.063.

(84) Lee, S.; Chon, H.; Lee, J.; Ko, J.; Chung, B. H.; Lim, D. W.; Choo, J. Rapid and Sensitive Phenotypic Marker Detection on Breast Cancer Cells Using Surface-Enhanced Raman Scattering (SERS) Imaging. *Biosens. Bioelectron.* **2014**, *51*, 238–243. https://doi.org/10.1016/j.bios.2013.07.063.

(85) L. Kleinman, S.; R. Frontiera, R.; Henry, A.-I.; A. Dieringer, J.; Duyne, R. P. V. Creating, Characterizing, and Controlling Chemistry with SERS Hot Spots. *Phys. Chem. Chem. Phys.* **2013**, *15* (1), 21–36. https://doi.org/10.1039/C2CP42598J.

(86) Cancer Theranostics with Near-Infrared Light-Activatable Multimodal Nanoparticles | Accounts of Chemical Research https://pubs.acs.org/doi/abs/10.1021/ar200022e (accessed Nov 4, 2020).

(87) Li, W.; Chen, X. Gold Nanoparticles for Photoacoustic Imaging. *Nanomed.* **2015**, *10* (2), 299–320. https://doi.org/10.2217/nnm.14.169.

(88) Fu, Q.; Zhu, R.; Song, J.; Yang, H.; Chen, X. Photoacoustic Imaging: Contrast Agents and Their Biomedical Applications. *Adv. Mater.* **2019**, *31* (6), 1805875. https://doi.org/10.1002/adma.201805875.

(89) Biomedical Applications of Shape-Controlled Plasmonic Nanostructures: A Case Study of Hollow Gold Nanospheres for Photothermal Ablation Therapy of Cancer | The Journal of Physical Chemistry Letters https://pubs.acs.org/doi/abs/10.1021/jz900366c (accessed Nov 5, 2020).

(90) You, J.; Zhang, G.; Li, C. Exceptionally High Payload of Doxorubicin in Hollow Gold Nanospheres for Near-Infrared Light-Triggered Drug Release. *ACS Nano* **2010**, *4* (2), 1033–1041. https://doi.org/10.1021/nn901181c.

(91) Effects of Photoacoustic Imaging and Photothermal Ablation Therapy Mediated by Targeted Hollow Gold Nanospheres in an Orthotopic Mouse Xenograft Model of Glioma | Cancer Research https://cancerres.aacrjournals.org/content/71/19/6116.short (accessed Sep 24, 2020).

(92) Melancon, M. P.; Lu, W.; Yang, Z.; Zhang, R.; Cheng, Z.; Elliot, A. M.; Stafford, J.; Olson, T.; Zhang, J. Z.; Li, C. In Vitro and in Vivo Targeting of Hollow Gold Nanoshells Directed at Epidermal Growth Factor Receptor for Photothermal Ablation Therapy. *Mol. Cancer Ther.* **2008**, *7* (6), 1730–1739. https://doi.org/10.1158/1535-7163.MCT-08-0016.

(93) Sancho-Albero, M.; Mar Encabo-Berzosa, M. del; Beltrán-Visiedo, M.; Fernández-Messina, L.; Sebastián, V.; Sánchez-Madrid, F.; Arruebo, M.; Santamaría, J.; Martín-Duque, P. Efficient Encapsulation of Theranostic Nanoparticles in Cell-

Derived Exosomes: Leveraging the Exosomal Biogenesis Pathway to Obtain Hollow Gold Nanoparticle-Hybrids. *Nanoscale* **2019**, *11* (40), 18825–18836. https://doi.org/10.1039/C9NR06183E.

(94) You, J.; Wang, Z.; Du, Y.; Yuan, H.; Zhang, P.; Zhou, J.; Liu, F.; Li, C.; Hu, F. Specific Tumor Delivery of Paclitaxel Using Glycolipid-like Polymer Micelles Containing Gold Nanospheres. *Biomaterials* **2013**, *34* (18), 4510–4519. https://doi.org/10.1016/j.biomaterials.2013.02.069.

(95) Yu, M.; Guo, F.; Wang, J.; Tan, F.; Li, N. Photosensitizer-Loaded PH-Responsive Hollow Gold Nanospheres for Single Light-Induced Photothermal/Photodynamic Therapy. *ACS Appl. Mater. Interfaces* **2015**, *7* (32), 17592–17597. https://doi.org/10.1021/acsami.5b05763.

(96) Wang, Z.; Li, S.; Zhang, M.; Ma, Y.; Liu, Y.; Gao, W.; Zhang, J.; Gu, Y. Laser-Triggered Small Interfering RNA Releasing Gold Nanoshells against Heat Shock Protein for Sensitized Photothermal Therapy. *Adv. Sci.* **2017**, *4* (2), 1600327. https://doi.org/10.1002/advs.201600327.

(97) Biagioni, P.; Celebrano, M.; Savoini, M.; Grancini, G.; Brida, D.; Mátéfi-Tempfli, S.; Mátéfi-Tempfli, M.; Duò, L.; Hecht, B.; Cerullo, G.; Finazzi, M. Dependence of the Two-Photon Photoluminescence Yield of Gold Nanostructures on the Laser Pulse Duration. *Phys. Rev. B* **2009**, *80* (4), 045411. https://doi.org/10.1103/PhysRevB.80.045411.

(98) Kansal, S. K.; Singh, M.; Sud, D. Studies on Photodegradation of Two Commercial Dyes in Aqueous Phase Using Different Photocatalysts. *J. Hazard. Mater.* **2007**, *141* (3), 581–590. https://doi.org/10.1016/j.jhazmat.2006.07.035.

(99) Nakamura, M.; Ozaki, S.; Abe, M.; Matsumoto, T.; Ishimura, K. One-Pot Synthesis and Characterization of Dual Fluorescent Thiol -Organosilica Nanoparticles as Non-Photoblinking Quantum Dots and Their Applications for Biological Imaging. *J. Mater. Chem.* **2011**, *21* (12), 4689–4695. https://doi.org/10.1039/C0JM04259E.

(100) Probing the Cytotoxicity of Semiconductor Quantum Dots | Nano Letters https://pubs.acs.org/doi/abs/10.1021/nl0347334?casa_token=3LcP_3ZGq58AAAAA:Pe0L826mgZM_-pxv8eGiug1uJEkMbPnsKMxrqD3F4Nev1R1565CBn1i9fmuByR9uMQJEj4ZZKSEFkhTMjg (accessed Nov 27, 2020).

(101) Near-Field Two-Photon-Induced Photoluminescence from Single Gold Nanorods and Imaging of Plasmon Modes | The Journal of Physical Chemistry B https://pubs.acs.org/doi/abs/10.1021/jp051631o?casa_token=TMUNeFtmcGIAAAAA:8hYdkxixKIhZnnVEsKhw_phZZ4y6cWWGSw2vNwZpkNJXfVwhLSU3Ncl27fIRlfRbOWQlh1GNcLpQ8ANq2g (accessed Nov 24, 2020).

(102) Mohamed, M. B.; Volkov, V.; Link, S.; El-Sayed, M. A. The `lightning' Gold Nanorods: Fluorescence Enhancement of over a Million Compared to the Gold Metal. *Chem. Phys. Lett.* **2000**, *317* (6), 517–523. https://doi.org/10.1016/S0009-2614(99)01414-1.

(103) Wu, X.; Yang, F.; Ming, T.; Xiong, R.; Wang, P.; Chen, J. Au Nanorods Can Be Used for Long-Term Cell Imaging? *Appl. Phys. Lett.* **2011**, *98* (21), 213704. https://doi.org/10.1063/1.3593961.

(104) Enhanced Radiosensitization of Gold Nanospikes via Hyperthermia in Combined Cancer Radiation and Photothermal Therapy | ACS Applied Materials & Interfaces https://pubs.acs.org/doi/abs/10.1021/acsami.6b10132?casa_token=SOUwk-QPfgsAAAAA:6lneFoAYZuOLosUwbeKSucQ_lHdaA2XrGIB144x2r3AjboP3L1X_QK3FYa1Yp80gFk3-_1c-1JvfXwf6JA (accessed Nov 29, 2020).

(105) Chen, H.; Shao, L.; Ming, T.; Sun, Z.; Zhao, C.; Yang, B.; Wang, J. Understanding the Photothermal Conversion Efficiency of Gold Nanocrystals. *Small* **2010**, *6* (20), 2272–2280. https://doi.org/10.1002/smll.201001109.

(106) Zeng, J.; Goldfeld, D.; Xia, Y. A Plasmon-Assisted Optofluidic (PAOF) System for Measuring the Photothermal Conversion Efficiencies of Gold Nanostructures and Controlling an Electrical Switch. *Angew. Chem.* **2013**, *125* (15), 4263–4267. https://doi.org/10.1002/ange.201210359.

Chapter Two

2 Near-Infrared Light Absorbing Silver Coated Hollow Gold Nanostars for Surface Enhanced Raman Scattering Detection of Bovine Serum Albumin Using Capping Ligand Exchange

2.1 Abstract

Two novel urchin-like plasmonic nanostructures, hollow gold nanostars (HNSs) and silver-coated hollow gold nanostars (AgHNSs), were synthesized using hollow gold nanospheres (HGNs) as a template. The particle morphology was assessed by transmission electron microscopy (TEM), optical properties were characterized by UV-Vis spectroscopy, and elemental composition was evaluated by both inductively coupled plasma-optical emission spectrometry (ICP-OES) and energy dispersive X-ray (EDX) analysis. Both the HNSs and AgHNSs exhibit tunable structural and optical properties. Their unique star-shaped structure provides desired "hot spots" for enhancing the electromagnetic (EM) field for surface enhanced Raman scattering (SERS) applications, while their near-infrared (NIR) absorption is ideal for biomedical applications. A comparative analysis of the relative SERS enhancement using Rhodamine 6G (R6G) showed that HNSs reported herein have an order of magnitude higher relative enhancement over previously reported HNSs. Moreover, AgHNSs have a four-fold increase in SERS signal compared to HNSs. Discrete dipole approximation (DDA) simulations of electric field enhancement were used to corroborate the experimental findings. The comparison between the experimental and theoretical results suggests that the significant increase

in SERS enhancement cannot be completely explained by the larger dielectric constant of silver. The branching of individual spikes, or increased binding efficacy of the analyte to the nanoparticles, likely also plays an important role. To further explore the applicability of these novel structures, successful capping ligand exchange from citrate to pentanethiol was used to switch the surface charge from negative to positive to facilitate the SERS detection of dried bovine serum albumin (BSA). AgHNSs are a stable and effective NIR absorbing substrate for SERS detection of biological samples. Elemental analyses of the AgHNSs, in conjunction with DDA simulations, provide insights into their enhancement mechanism.

2.2 Introduction

Raman scattering is a molecularly specific technique based on the measurement of the vibrational frequency of molecules. However, most biological molecules have low polarizability, yielding a low Raman signal.[1,2] Therefore, surface enhanced Raman scattering (SERS) is often used to increase the Raman signal by allowing molecules to interact with the enhanced electromagnetic (EM) field due to a roughened metal surface or metal nanoparticles.[3] SERS has been particularly useful in the detection of biological molecules that have weak normal Raman signals.[2–4]

Serum albumins are the most abundant proteins in the circulatory system and contribute to osmotic blood pressure. They play a major role in drug deposition and success.[5] As an example of such proteins, bovine serum albumin (BSA) in both its dried and liquid forms has often been studied as a model system.[6] Like most proteins, BSA has a weak Raman signal but has been successfully detected using SERS with different nanoparticles.[7–9] However, as BSA is negatively charged at low to neutral pH,[10] it does not bind well on negatively charged nanoparticles, especially when dried. Thus, positively charged particles are desired for improved BSA detection,[11] especially for detecting samples in dry form.[12] Dried samples are used as references as they often yield 1-2 orders of magnitude increased Raman signal and remove solvent background.[13] These benefits are particularly useful in diagnostic studies and biopsies.[12]

Plasmonic nanostructures, typically composed of coinage metals like copper, silver, and gold, are common and effective substrates for SERS. They exhibit tunable optical and electronic properties due to their structure-dependent surface plasmon resonance (SPR).[14] Among the different plasmonic metals, gold nanoparticles are often utilized for biological applications due to their low toxicity, stability, tunability, and biological compatibility.[15–17] Gold nanoparticles such as solid nanospheres[18], nanorods[19], hollow nanospheres (HGNs)[20–22], and solid nanostars have been used for SERS. Nanostars have shown increased SERS activity, with reported enhancement factors 2-5 orders of magnitude higher than their solid spherical counterparts.[23] The increased SERS activity has been attributed to the spikes that act as antennae to produce strong EM field enhancements. Additionally, analytes are more likely to be trapped in between spikes of the nanoparticles.[24–26] Thus, nanostars exhibit both tip and gap hot spots without the need for aggregation.[27] Hollow structures such as HGNs are highly tunable with both internal and external surfaces, whose coupling further enhances the EM field as well as their SERS capabilities.[28] Moreover, the hollow core allows for an added degree of structural control in tuning the SPR by varying shell thickness.[29] Our lab has recently demonstrated that it is possible to introduce spikes on the surface of HGNs, which allows the combination of the properties of HGNs with those of gold nanostars into one structure, hollow gold nanostars (HNSs), with improved SERS activity.[65]

While gold is well situated for biological studies, silver is generally a more sensitive SERS substrate.[30] However, silver is less stable than gold.[31–33] As a result, bimetallic Ag-Au nanoparticles have been studied with the combined stability of gold and strong SERS of silver.[34] Likewise, solid gold nanostars have been coated with silver for SERS applications, however, most do not have the same level of tunability or do not retain their spikes and their NIR absorption after coating.[35,36] Silver coated HNSs (AgHNSs) retain their NIR absorption and their spiky structure, however, they are often capped with negatively charged species such as citrate, limiting their use with negatively charged analytes. By exchanging negatively charged capping ligands like citrate for those with positive charges, one may facilitate SERS detection of negatively charged molecules like BSA even when samples are dried.[37–41]

In this work, we have synthesized three hollow, plasmonic nanoparticles for comparative study of their SERs activities. Their morphology was assessed by TEM, optical properties were analyzed by UV-Vis spectroscopy, and elemental composition was evaluated by both ICP-OES and EDX. Detailed analysis of the relative SERS enhancement of the HNSs and AgHNSs, combined with DDA simulations, was used to gain insight into the mechanism of the enhancement, which is attributed to both the

EM effect and chemical effect of silver.[42] Additionally, successful capping ligand exchange from citrate to pentanethiol was used to switch the surface charge from negative to positive to facilitate the SERS detection of dried BSA. AgHNSs are a stable, versatile, and effective NIR absorbing substrate for SERS detection of dried biological samples.

2.3 Materials and Methods

2.3.1 Synthesis of Cobalt Nanoparticles

Cobalt (II) chloride hexahydrate ($CoCl_2 \cdot 6H_2O$) was purchased from Mallinckrodt, trisodium citrate dihydrate ($Na_3C_6H_5O_7 \cdot 2H_2O$) was purchased from VWR International, and sodium borohydride ($NaBH_4$) was purchased from Fisher Scientific. All water used in synthesis was ultrapure in quality, with a resistivity of 18.3 MΩ cm.

Cobalt nanoparticles were synthesized according to the procedure found in Lindley et al.[29] Briefly, 100 μL of 0.40 M cobalt (II) hexahydrate and 930 μL of 0.40 M trisodium citrate dihydrate were added to 100 mL of ultrapure water in a 500 mL round-bottom flask. This solution was magnetically stirred at 700 rpm and deaerated with nitrogen for one hour.

A 300 μL mixture of freshly prepared aqueous 1.0 M $NaBH_4$ and 1.0 M $NaB(OH)_4$ was prepared in a ratio of 1:2. The mixture was immediately injected into the cobalt solution while it continuously stirred under nitrogen. The solution was stirred for two minutes and turned from pale pink to dark brown, indicating the reduction of Co^{2+} ions and the formation of Co_2B nanoparticle scaffold. To ensure the complete reaction of borohydride, the nanoparticles were allowed to react for 90 minutes.

2.3.2 Synthesis of Hollow Gold Nanospheres

HGNs were synthesized using well documented sacrificial cobalt nanoparticle template method.[29,43,44] Chloroauric acid ($HAuCl_4$) was purchased from Fisher Scientific. Ultrapure water with a resistivity of 18.3 MΩ cm was used. A 15 mL solution of 0.667 mM chloroauric acid and ultrapure water was deaerated with nitrogen for one hour while stirring at 700 rpm. The gold salt solution was injected in its entirety into the cobalt nanoparticle solution and allowed to stir for five minutes under a nitrogen atmosphere. The solution was exposed to air and allowed to react until the color changed from brown to blue, indicating the oxidation of the cobalt scaffold and the formation of the gold shell.

2.3.3 Synthesis of Hollow Gold Nanostars

The surface morphology of HGNs was changed to make HNSs by following a previously published protocol from the Vo Dinh group.[27] Chloroauric acid ($HAuCl_4$), L-Ascorbic acid, silver nitrate ($AgNO_3$), and 38.0% hydrochloric acid (HCl) were purchased from Fisher Scientific. All water used in synthesis was ultrapure in quality with a high resistivity. A gold salt solution containing 20 mL of water and 50 μL of $HAuCl_4$, a 1.0 mL 1.0 M HCl solution, 20 mL of 3.0-4.2 mM $AgNO_3$ solution, and 10 mL of 100 mM ascorbic acid solution were made. Immediately after the preparation of the ascorbic and silver nitrate solutions, 20 μL of 1.0 M HCl and 200 μL of the hollow gold nanosphere solution were added to the entirety of the gold salt solution into a 50 mL beaker. Then, 200 μL of the silver nitrate solution and 100 μL of the ascorbic acid solution were added quickly and simultaneously. The addition caused an immediate color change from clear to blue-grey, indicating the formation of spikes on the surface of the hollow gold nanosphere seed particle.

2.3.4 Synthesis of Silver Coated Hollow Gold Nanostars

L-Ascorbic acid and silver nitrate ($AgNO_3$) and were purchased from Fisher Scientific. Milli-q water was used for the synthesis. Silver coating protocol was modified from Olsen et al. and Sonay *et al.*[45,46] First, 3.0 mL of as-prepared HNSs were added to a 50 mL beaker. Then, 2.24 mL of 0.10 mM ascorbic acid were added respectively to 3.0 mL of the HNS solution. A 1.0 M silver nitrate solution was added to the ascorbic acid and nanoparticle solutions in 20 μL aliquots every 30 seconds while stirring with a magnetic stir bar at 1000 rpm. A total of 390 μL of silver nitrate solution was added to the HNS solution. The HNS solution changed from blue-grey back to blue, indicating the replacement of silver on the surface of the hollow gold nanostars.

2.3.5 Characterizations

UV-vis spectra were obtained using an Agilent Technologies Cary 60 UV-Vis spectrophotometer using a 700 μL quartz cuvette with 10 mm optical path length. The extinction measurements were performed on all plasmonic particles as prepared. Zeta potential measurements were taken on a Malvern Panalytical zetasizer nano ZS90 with 1.0 mL disposable folded capillary cells for three trials with automated run times. Energy dispersive X-Ray (EDX) mapping of the HNS and AgHNS samples was performed using an FEI TitanX electron microscope operating at 200 kV.

ICP-OES was conducted using 38.0% hydrochloric acid (HCl) and 70.0% nitric acid (HNO_3) purchased from Fisher Scientific. All water used in sample preparation was ultrapure in quality, with a high resistivity. All samples and gold standard solutions were mixed with a gold blank solution composed of 5.0 mL of HCl and 9.0 mL of HNO_3 in up to 100 mL of water. A 20 ppm gold solution was prepared and diluted to 10 ppm, 5 ppm, 2 ppm, and 1 ppm. To create an HGN sample, 600 μL of as prepared HGN solution was added to 5400 μL of the gold blank solution. In order to make the HNS and AgHNS sample solutions, two 1 mL aliquots of each as-prepared sample were washed by centrifugation at 13,000 rpm for one minute, the supernatant was disposed of, and the concentrated particles were combined and diluted to 1.0 mL with water. Then, 600 μL of the washed particles were added to 5400 μL of the gold blank solution respectively. Silver standards were prepared with a silver blank solution. The silver blank solution was composed of 13 mL of HNO_3 in up to 100 mL of water. A 10 ppm silver standard solution was prepared and diluted to 5 ppm, 2 ppm, 1 ppm, and 0.5 ppm. The silver blank was used in subsequent washing protocols between samples. All elemental analyses were taken on a Thermo iCap radial view inductively coupled plasma optical emission spectrometer (ICP-OES). Internal standardization was carried out with Sc and Y internal references. Two Au wavelengths (242.795 and 267.595 nm) and one Ag wavelength (328.068 nm) were used for analysis.

Scanning electron microscopy (SEM) was performed at the W.M. Keck Center for Optofluidics at the University of California, Santa Cruz on an FEI Quanta 3D field emission microscope operated at 10.0 kV acceleration voltage. All samples were dropped onto hexagonal, 400 mesh copper grids with a carbon support film of standard 5−6 nm thickness (Electron Microscopy Sciences) and allowed to air dry. High-resolution transmission electron microscopy (HRTEM) was performed on an FEI UT Tecnai microscope operated at 200 kV acceleration voltage. Diameter measurements were taken directly from electron microscope images using ImageJ software. HGN solutions were centrifuged twice under ambient conditions at 13,000 rpm for two minutes and resuspended in ultrapure water. HNSs and AgHNSs and washed once at 13,000 rpm for one minute. For each sample, 30 HGN diameters were used to calculate the average diameter.

2.3.6 Simulations

Using the discrete dipole approximation (DDA) method, the extinction spectra and the enhanced electric field of the nanostars were calculated with different numbers of spikes. In the simulations, the dielectric constants of the silver and gold were taken from Palik's handbook.[47] The length of the discrete dipole used was one nanometer and the medium of the nanoparticle was water, which is the same as that in the experiment. The structure parameters of the nanostars are taken from experimental measurements. The diameter of the core in the central core-shell structure is 13 nm and the diameter of the outer layer of the core is 39 nm. The spike is 34 nm in length and 10 nm in diameter, however, the spike will become thicker at the bottom with a cone shape. Simulations were run for nanostars composed of pure gold, pure silver, and Ag/Au alloys containing 8% in weight (HNSs). We also calculated nanostars where the core is composed of Ag/Au alloy with 8% silver weight while the alloy in spikes is 14% silver in weight (AgHNSs).

2.3.7 Raman and SERS Spectroscopies

Rhodamine 6G (R6G) was purchased from Acros Organics. All water used in sample preparation was ultrapure in quality. A concentrated 10^{-3} M solution of R6G in water was prepared and serial dilution was conducted to produce 10^{-4},10^{-5}, 10^{-6}, 10^{-7}, and 10^{-8} M using HGN, HNS, and AgHNS solutions. The HGNs and AgHNSs were used as prepared, while the HNSs were diluted by 42.7% before adding R6G to keep the number of particles constant between HNSs and AgHNSs. The samples were focused on using the Olympus BH2-UMA microscope using a 633 nm laser at 12 mW for 30 seconds with two accumulations. This was used for its ability to better analyze liquid samples.

Pentanethiol was purchased from Alfa Aesar and 96.0% solid bovine serum albumin (BSA) was purchased from Sigma Aldrich. First, capping ligand exchange was conducted by adding 1.0 mL of 0.60 mM pentanethiol solution to 1.0 mL of with HNSs or AgHNSs. Then, BSA was added to 100 μL pentanethiol capped particles to make a 10^{-4} M solution. The resulting solution was dropped onto a stainless-steel plate and allowed to dry for one hour. Raman measurements were conducted on a Thermo Fisher DRX3 785 nm laser at a power of 1 mW for 30 seconds and three accumulations using a 100x objective. Multiple measurements were taken, and all measurements were taken on the dark outer ring of the dried sample to remove the drying pattern as a variable (see image below). While the higher wavelength of laser likely reduced the intensity of the Raman spectrum, this system was used for its mapping capabilities and is ideal for dried samples.

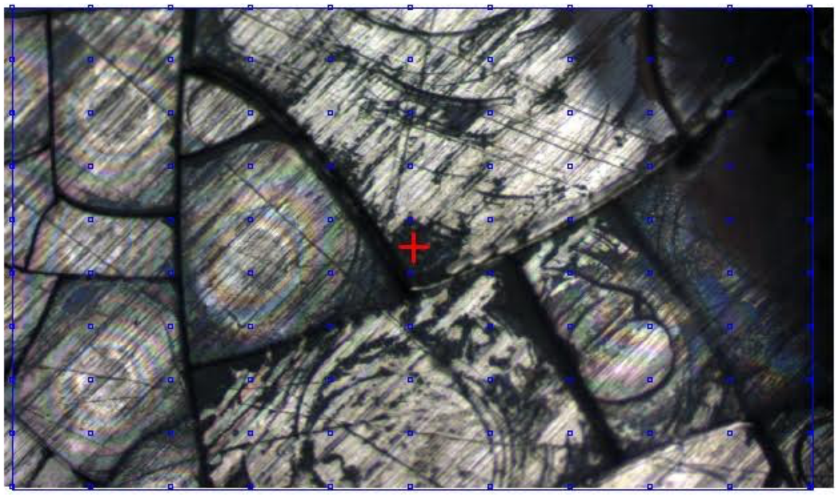

Figure 2-1: Mapping of dried BSA sample on stainless steel.

2.4 Results and Discussion

2.4.1 Optical and Structural Properties

Solid gold nanospheres exhibit a size-dependent SPR band around 540 nm.[48] As SPR is also greatly dependent on the shape, creating a hollow cavity, like in HGNs, allows tuning of the SPR into the NIR region.[29,43,49,50] Three types of hollow plasmonic nanostructures were synthesized for comparative study in this work. The HGNs are smooth and spherical with an average outer diameter of 30 nm (Figure 2-1b), with a strong, relatively narrow SPR band peaked around 560 nm (Figure 2-2a), due to their monodispersity and spherical shape.[29]

Upon the addition of gold ions, ascorbic acid, and silver nitrate to the HGN solution, HNSs with urchin-like protrusions are produced (Figure 2-2c,d,e). This results in a significantly broadened SPR peaked around 860 nm with a shoulder at 540 nm (Figure 2-2a). The resulting spectrum is similar, although shifted, to the characteristic spectra of solid gold nanostars.[26,51,52] The 540 nm shoulder likely corresponds to the HGN core of the particle, blue-shifted due to the thickening of the gold shell. The 860 nm band can be attributed to the gold spikes.[24,26] The broadening of the spectrum is likely due to the branching on each spike and polydispersity. The structural and optical properties of these HNSs were tuned by increasing the concentration of silver cations available during gold spike formation, which resulted in increased spike length and branching of individual spikes.

Finally, reducing silver ions on the surface of the existing HNSs to form AgHNSs did not result in a noticeable change in structure (Figure 2-2 f, g, h). The resulting nanostructures retain their urchin-like characteristics, however, their SPR changes significantly. There is a slightly more pronounced SPR band peaked around 540 nm attributed to the HGN core, indicating that the core is relatively unchanged in size. This is supported by TEM results. However, the peak at 840 nm is blue-shifted to 720 nm (Figure 2-2a). Since the primary structure remains relatively unchanged, the shift can be attributed to the replacement of gold with silver. Moreover, since no peak appears at 420 nm, which is often associated with the SPR of silver nanoparticles, it does not seem that silver nanoparticles were generated as a byproduct. The combination of the 120 nm blue shift without the appearance of a 420 nm peak indicates a silver coating.[53] The silver addition can further be understood with a closer look at the spikes under HRTEM (Figure 2-2 e, h). The lattice spacing of the HNSs and the AgHNSs both match those for gold from the International Centre for Diffraction Data, [54] This indicates that although there was a significant impact on the SPR, the silver addition did not impact the existing gold crystal lattice and likely exists as a thin layer on the HNS surface. AgHNSs retain their NIR absorption as a consequence of their hollow core, unlike their solid silver-coated gold nanostar counterparts.[35,55] These characteristics make them better situated for *in vivo* studies that require experiments to be conducted where blood and tissue are transparent.

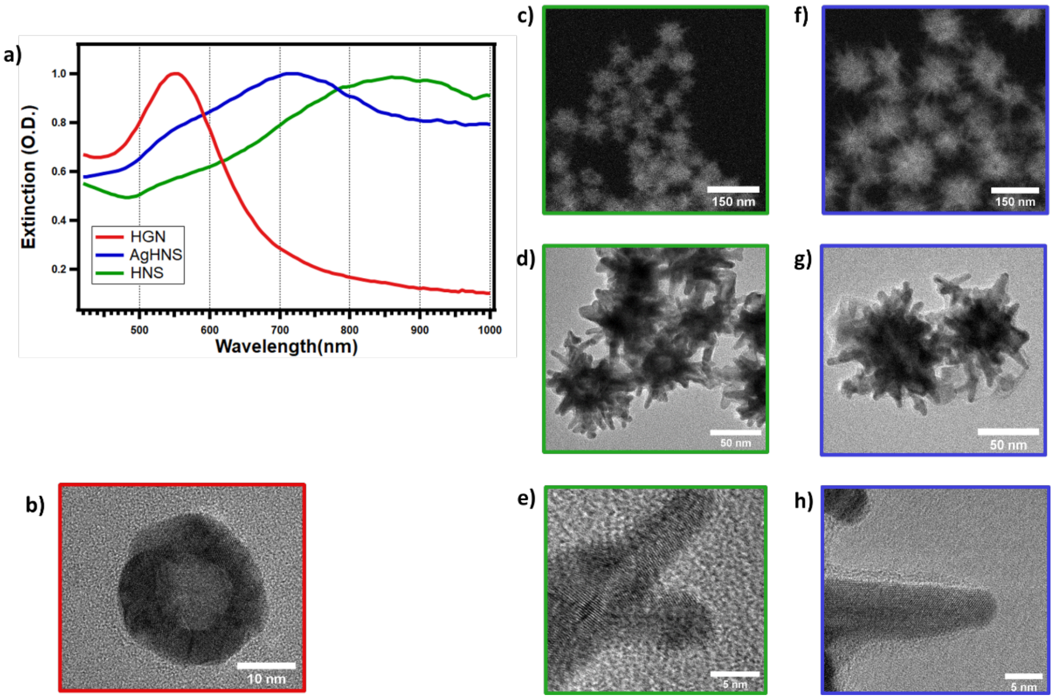

Figure 2-2 UV-Vis spectra (a), SEM images (b, c, f) of HGNs, HNSs, and AgHNSs, respectively. HRTEM images of HNSs (d, e) and AgHNSs (g, h).

2.4.2 Elemental Composition and Surface Properties

Given the lack of change in structure with the addition of the silver coating, we sought to explore the extent to which silver was incorporated into the system. ICP-OES was employed to compare and quantify the concentration of silver and gold incorporated into the nanoparticles' structures (Table 1 dark grey). As silver is only used in small amounts as a catalyst during the synthesis of HNSs, it was not expected to be significantly incorporated into the HNS structure. However, from these concentrations, it was determined that HNSs are compositionally ~8 wt% silver. Thus, any resulting EM enhancement could potentially be attributed, not only the shape of the nanostructure, but also chemical composition. By contrast and as expected, AgHNSs contain nearly twice the weight percent in silver than that of HNSs. This suggests successful deposition silver. The specific concentration values of gold and silver for each sample are given in Table S1.

Additionally, the surface layer elemental composition of both HNSs and AgHNSs was determined by EDX elemental mapping with a penetration depth of 0.45 nm. The surface of the HNS is only 2.04 wt% silver. The combination of the EDX and the ICP-OES data suggests that silver is fully embedded in the structure. However, the surface of the AgHNS structure was found to be 13.76 wt% silver (Table I light grey). Therefore, the silver found in the is structure is predominantly on the surface of the nanoparticle.

Table 2-I Weight Percentage of Gold and Silver as Determined by ICP-OES (Bulk) and EDX (Surface)

Sample	Weight Percent Gold (%)	Weight Percent Silver (%)	Surface Weight Percent Gold (%)	Surface Weight Percent Silver (%)
HGN	100	-	-	-
HNS	92.3	7.69	97.96	2.04
AgHNS	84.07	15.93	86.26	13.76

The above data help to provide some insight into the growth mechanism of the nanostructures. The synthesis of HNSs uses similar principles to that of gold nanorods,[54] using silver as a catalyst to assist in anisotropic growth of gold spikes onto the surface of the HGN seed particle (Figure 2-3). In this process, we observe a small amount of silver trapped in the gold crystal lattice.

However, using the same reagents in different concentrations, silver deposition on the surface of the HNSs is achieved to form AgHNSs. Ascorbic acid is used as a weak reducing agent and cannot reduce silver ions without the presence of gold seed particles. In this case, HNS seed particles lower the reduction potential of the salt allowing the silver to be catalytically reduced onto the surface of the HNSs (Figure 2-3). Silver is added slowly, keeping its concentration sufficiently low, thus favoring the heterogenous nucleation and growth of silver films onto HNSs (Figure 2-2).[2]

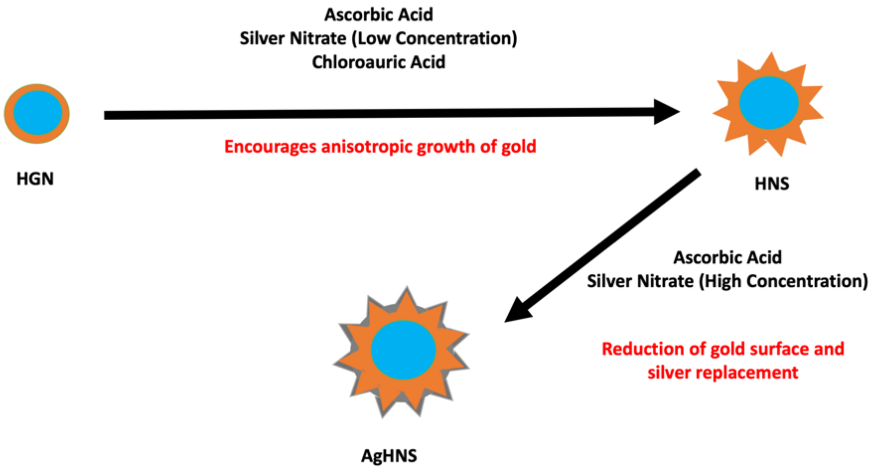

Figure 2-3 Schematic of the HGN seed templated synthesis of HNSs of varying rugosity and silver coating.

While silver deposition is often used to enhance the Raman signal, it can cause stability issues. To explore the effects of the spikes and silver coating, zeta potential measurements were taken for the HGNs, HNSs, and AgHNSs and determined to be -36.7, -40.7, -30.3 mV respectively. Zeta potential results indicate the charge on the surface of a particle and therefore the degree of repulsion between similarly charged particles, which prevents aggregation. The instability of silver can result in zeta potential measurements as low as 10 mV.[56] The as-prepared hollow plasmonic particles are negatively charged due to citrate capping ligands.

HGNs, HNSs, and AgHNSs all have zeta potential magnitudes above 30 mV, indicating a relatively high level of stability for a nanoparticle, making them well situated for *in vivo* work where stability is paramount. Furthermore, we can conclude that the silver coating does not significantly increase the likelihood of aggregation of AgHNSs, which is usually undesired since it often leads to inconsistent Raman measurements.[57]

2.4.3 Surface-Enhanced Raman Scattering Spectra and Mechanism

SERS spectra were obtained for all substrates, using a 633 nm laser system ideal for liquid samples. The probe molecule R6G was used to examine, and compare, sensitivity and consistency before and after the silver coating on the gold nanostructures. A requisite spectrum comparing R6G at 10^{-6} M is provided in Figure 2-4. The SERS spectra of R6G combined with HNS and AgHNS solutions have been reduced by a factor of 100 to better overlay the spectra.

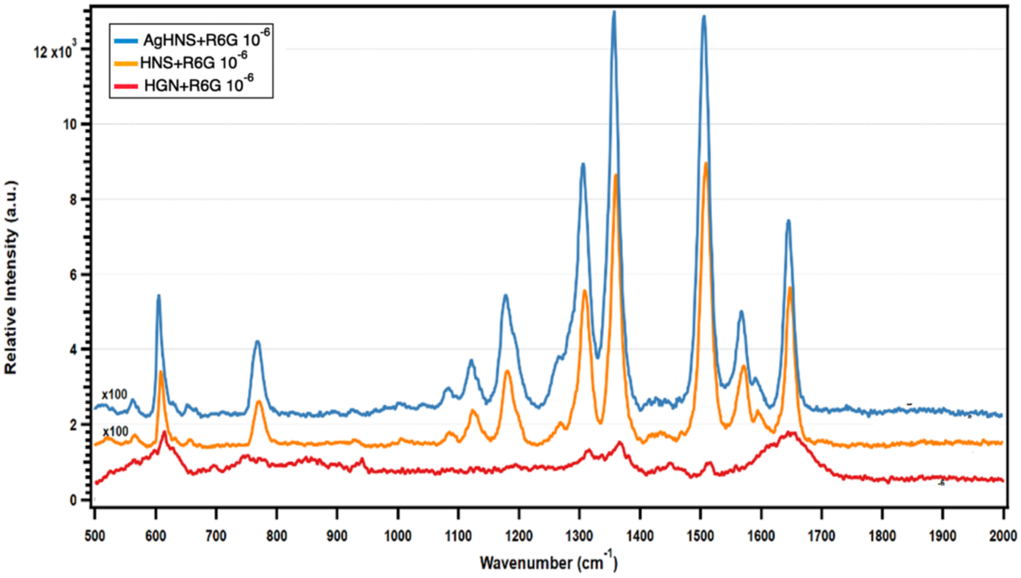

Figure 2-4 SERS spectra for a 10^{-6} M solution of R6G in HGNs (red), HNSs (orange), and AgHNSs (blue).

The relative intensities of the 1507 cm^{-1} peak are used to calculate enhancement factors relative to HGNs.[58] A description of the methods used to find these enhancement factors is provided in the SI. The HNSs exhibited 1280 times enhancement over HGNs for the 1507 cm^{-1} vibrational mode. Our lab has recently observed an analytical enhancement factor of 6.2x10^5 for HGNs alone using the same vibrational mode of R6G.[59] The HGNs benefit from the enhancement of the EM field by both the interior and exterior surfaces.[20] With the addition of the spikes, the relative enhancement factor increased by three orders of magnitude, which can be explained by the increase in the number of active binding sites for the analyte molecules, and by the antenna effect of the spikes.[51] The relative enhancement factor shown here is an order of magnitude higher than previously reported HNSs,[59] likely due to the increased amount of silver, causing an increased spike tip length and branching, leading to a further enhanced EM field and number of hot spots.

Finally, with the addition of a silver layer to the HNSs, AgHNSs exhibit a 5630-fold enhancement from HGNs. Comparing this to the relative enhancement factor of HNSs alone, we can conclude that the light silver coating on AgHNSs does yield a 439% increase in signal. This is expected as silver is known to be a better SERS substrate than gold.[60] As evidenced by EDX, the surface of the AgHNSs is ~14%, over 6x that of the HNSs, which is likely responsible for the improved SERS enhancement. Using the known analytical enhancement factors of HGNs previously reported in our lab as a reference point,[59] the projected enhancement of the HNSs and the AgHNSs are ~7.95×10^8 and ~3.49×10^9 respectively (see SI for more details).

To corroborate these findings, DDA simulations were done to examine the optical and electric properties and evaluate the enhancement observed.[61,62] Raman enhancement is dependent on many variables, including shape and composition of the substrate, wavelength of the incident field, and many others that will not be discussed herein. The size and composition of the substrate affect the EM field, which is proportional to the enhanced electric field, $|E|^2$, at the excitation wavelength which is 633 nm as well as at the Stokes shifted wavelengths. We calculated both the $|E|^2$ at excitation and two Stokes shifted wavelengths corresponding to the Stokes shift of 500 cm^{-1} (at 658 nm) and 1500 cm^{-1} (at 700 nm). In the calculations, the incident light propagates along the X-axis and the contour plot is in the YZ plane and through the particle center. It should be noted that the simulations were conducted for a chemical composition nearly identical to that of the HNS, based on the combination of both ICP-OES and EDX data. However, for computational ease, the model assumes 12 uniform, unbranched, protruding spikes while the average HNS and AgHNS do experience both branching and polydispersity.

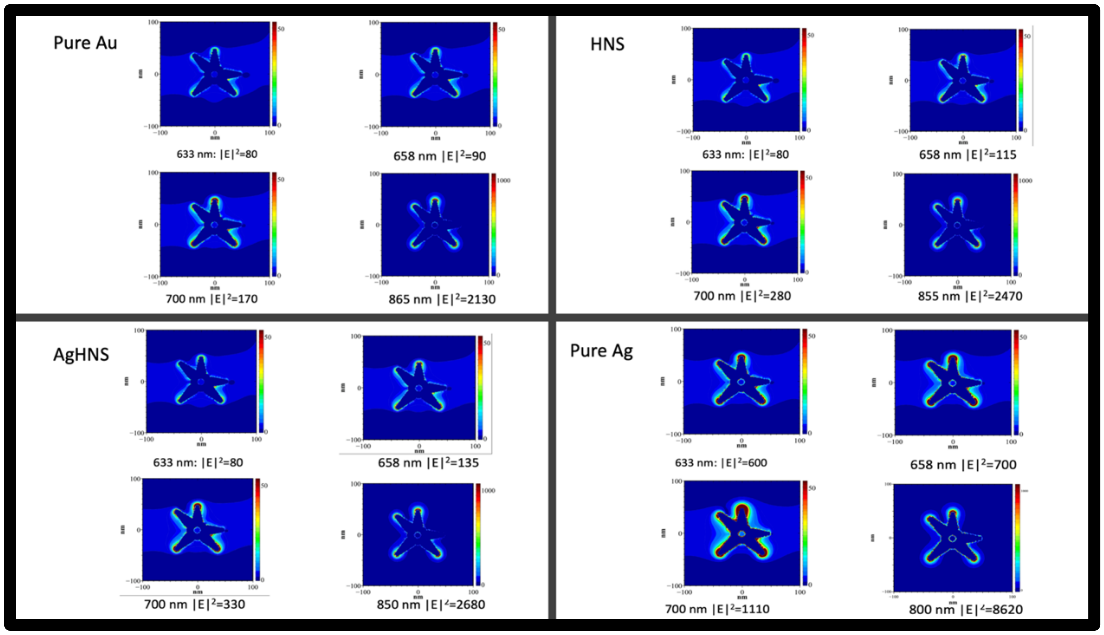

Figure 2-5 DDA Simulations of the Electric Enhancement Mapping of Pure Au Nanostars (top left), HNSs (top right), AgHNSs (bottom left), and Pure Ag Nanostars (bottom right). $|E|^2$ represents the highest enhanced electric field.

Electric fielding mapping was conducted for four nanoparticles, two experimental, HNSs and AgHNSs, and two theoretical, composed of pure gold and pure silver (Figure 2-5). As expected, the pure gold hollow nanostar exhibits the lowest electric field enhancement across four wavelengths, including the including the incident wavelength 633 nm, the two stokes shifted wavelengths, and the resonance wavelength (Figure 2-5 top left). Contrastingly, the pure Ag hollow nanostar shows an order of magnitude higher electric field at each wavelength except at 800 nm (Figure 2-5 bottom right).

The simulations for the HNS composed of 8% (Figure 2-4 top right) show a 50% increase in the electric field at the stokes shifted wavelength 700 nm. This corresponds to the mode at 1500 cm^{-1}, nearly equivalent to the 1507 cm^{-1} which were compared for the experimental R6G enhancement factors. Thus, since the previously reported HNSs contain proportionally less silver, this might be a reason for their lower relative enhancement.

The simulation of AgHNS shows a 17% increase in the electric field compared to the HNS without a silver coating at the same stokes shifted wavelength of 700 nm and mode of 1500 cm^{-1}. (Figure 2-5 bottom left). While the composition of silver is represented accurately, experimental data showed a 439% increase over HNSs at the same concentration. This indicates that the differences in the dielectric constants of gold and silver affecting the EM field are not sufficient to describe the experimentally observed enhancement factor. It is possible that the branching of individual spikes observed in the experimental structure accounts for some of the discrepancy by the production of more hot spots, thus, acting as a multiplier for the EM enhancement of silver over gold. It is also possible that silver acts as a more effective substrate for R6G due to more effective analyte-substrate interaction, producing a chemical enhancement.[63] R6G is known to bind effectively to both silver and gold, but a possible difference in binding efficacy of silver and gold is not established.[64] However, it has been shown that analytes, such as glutathione, do bind preferentially to silver over gold leading to increased chemical enhancement.[40] Also, as the interaction between substrate and analyte becomes stronger, the chemical enhancement becomes more substantial.[63] It is possible that the increased SERS signal from AgHNSs and R6G is partially due to increased chemical enhancement. Additionally, the lower zeta potential of the AgHNS might result in aggregation creating even more hot spots and increased enhancement factors.

2.4.4 Detection of Bovine Serum Albumin

To further explore the applicability of these novel structures, four 1.5×10^{-5} M solutions of BSA containing either HNSs or AgHNSs were prepared using citrate capped and pentanethiol capped nanoparticles and allowed to dry. Zeta potential measurements were conducted again on the pentanethiol capped nanoparticles. HNSs switched to 31.3 mV and AgHNSs switched to 25.7 mV. Comparing these reported zeta potentials with citrate capped particles, we see that the nanoparticles switch from negative to positive surface potential with the ligand exchange, and the pentanethiol capped particles retain similar zeta potential magnitudes. This indicates that stability is not lost with the replacement of the capping ligand. While pentanethiol is often used as a capping ligand,[65,66] its effect on surface potential is not usually mentioned. Here we observe that pentanethiol capped nanoparticles are noticeably positively charged. This is slightly unexpected due to the neutrality of pentanethiol. However, the positive charge could be due to weak induction, causing the electron density from the alkane to be situated on the sulfur. It is also possible that the acidic pH of the solution may be donating electrons and causing a positive charge.

A 785 nm laser was used to excite the pentanethiol and citrate capped particles and analytes as the instrument was better able to map and analyze dried samples. While SERS cross section is function of excitation wavelength and SPR signal depends on SPR wavelength, since the SPR of these samples is sufficiently broad, it is unlikely that this dependence would be significant.[67] However, the positively charged surface proved to be more effective at interacting with the negatively charged analyte, BSA. The more stable citrate capped HNSs and AgHNSs were less successful at yielding SERS signal, yielding little to no signal, under the same parameters as the pentanethiol capped particles using dried samples. The SERS spectra of pentanethiol capped HNSs and AgHNSs are shown in Figure 2-6.

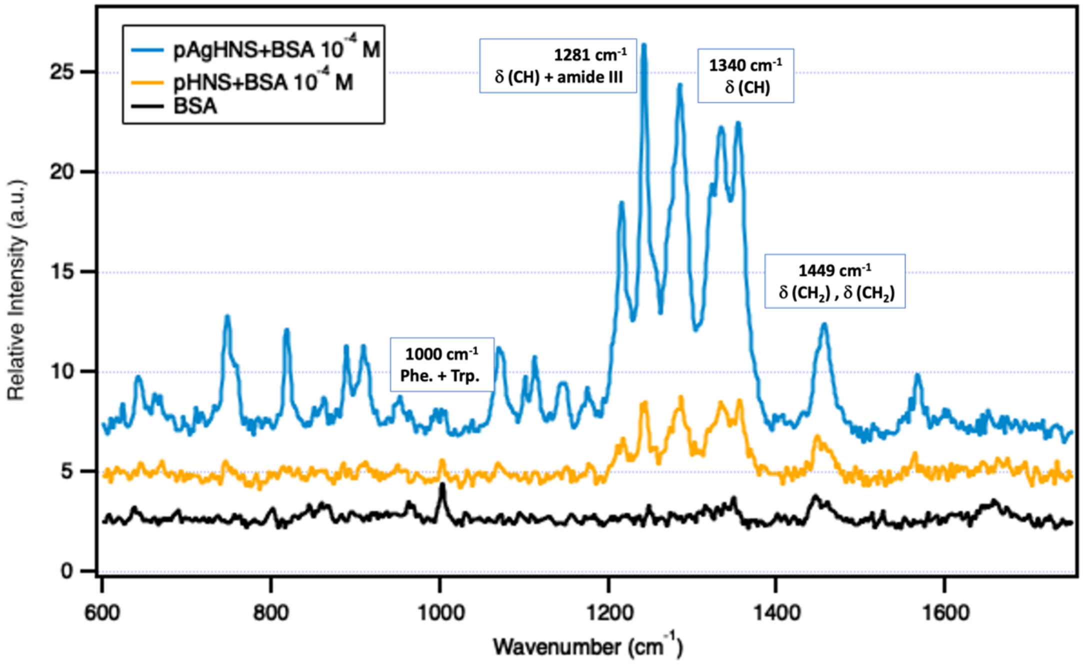

Figure 2-6 Raman Spectra for a 1.5 10^{-5} M solution of BSA in water (black), SERS spectra for 1.5 10^{-5} M solution of BSA in HNSs (orange), and AgHNSs (blue).

Vibrational analysis of SERS spectra in Figure 2-6 can be found in SI (Table S2). As both BSA and the citrate capped nanoparticles are negatively charged, it is likely that upon the drying of the sample, the analyte and nanoparticle would repel each other, drying on separate portions of the stainless steel, yielding little to no SERS signals. However, by conducting ligand exchange and changing the surface potential from negative to positive, the BSA and analyte dry near each other, yielding a significant enhancement. Moreover, the nanoparticles resonance peak wavelengths will be shifted during drying in comparison to those in water, similarly changing the SERS signal. By changing the capping ligand of these nanoparticles, we ameliorated their use for dried Raman samples. This is particularly useful for analytes that are difficult to analyze in solution. It should also be noted that AgHNSs retain their higher enhancement over HNSs even with dried samples and a different analyte, likely due to both their electromagnetic and chemical enhancement from the addition of silver. This is encouraging for their use with other analytes.

2.5 Conclusion

In summary, the structural and surface properties, optical characteristics, elemental composition, and SERS activities of HGNs, HNSs, and AgHNSs have been systematically studied and compared. The combined spiky surface morphology and strong NIR light absorption of the HNSs and AgHNSs are desired for NIR SERS applications. ICP-OES and EDX, elemental analyses of HNSs and AgHNSs were conducted to confirm the silver deposition into the crystal lattice of the HNSs and the surface of the AgHNSs. The efficacy of these particles for SERS was compared using R6G yielding a relative enhancement factor of 1280 for HNSs and 5630 for AgHNSs when compared to HGNs. Ligand exchange was conducted on the spiky HNSs and AgHNSs originally capped with citrate with pentanethiol. These pentanethiol capped particles yielded SERS spectra of BSA while the citrate capped particles did not. This indicates the successful switch to a positively charged capping ligand that is more effective for SERS for negatively charged analytes. AgHNSs present themselves as a novel and effective substrate well situated for biomedical applications due to their combined significant EM enhancement from the star structures and NIR absorption due to the hollow core.

2.6 References

(1) Nie, S. Probing Single Molecules and Single Nanoparticles by Surface-Enhanced Raman Scattering. *Science* **1997**, *275* (5303), 1102–1106. https://doi.org/10.1126/science.275.5303.1102.

(2) Olson, T. Y.; Schwartzberg, A. M.; Orme, C. A.; Talley, C. E.; O'Connell, B.; Zhang, J. Z. Hollow Gold−Silver Double-Shell Nanospheres: Structure, Optical Absorption, and Surface-Enhanced Raman Scattering. *J. Phys. Chem. C* **2008**, *112* (16), 6319–6329. https://doi.org/10.1021/jp7116714.

(3) Stiles, P. L.; Dieringer, J. A.; Shah, N. C.; Van Duyne, R. P. Surface-Enhanced Raman Spectroscopy. *Annual Review of Analytical Chemistry* **2008**, *1* (1), 601–626. https://doi.org/10.1146/annurev.anchem.1.031207.112814.

(4) Huang, G. G.; Han, X. X.; Hossain, M. K.; Ozaki, Y. Development of a Heat-Induced Surface-Enhanced Raman Scattering Sensing Method for Rapid Detection of Glutathione in Aqueous Solutions. *Anal. Chem.* **2009**, *81* (14), 5881–5888. https://doi.org/10.1021/ac900392s.

(5) Hu, Y.-J.; Liu, Y.; Wang, J.-B.; Xiao, X.-H.; Qu, S.-S. Study of the Interaction between Monoammonium Glycyrrhizinate and Bovine Serum Albumin. *Journal of Pharmaceutical and Biomedical Analysis* **2004**, *36* (4), 915–919. https://doi.org/10.1016/j.jpba.2004.08.021.

(6) Schwenk, N.; Mizaikoff, B.; Cárdenas, S.; I. López-Lorente, Á. Gold-Nanostar-Based SERS Substrates for Studying Protein Aggregation Processes. *Analyst* **2018**, *143* (21), 5103–5111. https://doi.org/10.1039/C8AN00804C.

(7) Shao, M.; Lu, L.; Wang, H.; Luo, S.; Ma, D. D. D. Microfabrication of a New Sensor Based on Silver and Silicon Nanomaterials, and Its Application to the Enrichment and Detection of Bovine Serum Albumin via Surface-Enhanced Raman Scattering. *Microchim Acta* **2009**, *164* (1), 157–160. https://doi.org/10.1007/s00604-008-0051-0.

(8) Iosin, M.; Canpean, V.; Astilean, S. Spectroscopic Studies on PH- and Thermally Induced Conformational Changes of Bovine Serum Albumin Adsorbed

onto Gold Nanoparticles. *Journal of Photochemistry and Photobiology A: Chemistry* **2011**, *217* (2), 395–401. https://doi.org/10.1016/j.jphotochem.2010.11.012.

(9) David, C.; Guillot, N.; Shen, H.; Toury, T.; Chapelle, M. L. de la. SERS Detection of Biomolecules Using Lithographed Nanoparticles towards a Reproducible SERS Biosensor. *Nanotechnology* **2010**, *21* (47), 475501. https://doi.org/10.1088/0957-4484/21/47/475501.

(10) Böhme, U.; Scheler, U. Effective Charge of Bovine Serum Albumin Determined by Electrophoresis NMR. *Chemical Physics Letters* **2007**, *435* (4), 342–345. https://doi.org/10.1016/j.cplett.2006.12.068.

(11) Avila, F.; Ruano, C.; Lopez-Tocon, I.; F. Arenas, J.; Soto, J.; C. Otero, J. How the Electrode Potential Controls the Selection Rules of the Charge Transfer Mechanism of SERS. *Chemical Communications* **2011**, *47* (14), 4213–4215. https://doi.org/10.1039/C0CC05314G.

(12) Moisoiu, V.; Iancu, S. D.; Stefancu, A.; Moisoiu, T.; Pardini, B.; Dragomir, M. P.; Crisan, N.; Avram, L.; Crisan, D.; Andras, I.; Fodor, D.; Leopold, L. F.; Socaciu, C.; Bálint, Z.; Tomuleasa, C.; Elec, F.; Leopold, N. SERS Liquid Biopsy: An Emerging Tool for Medical Diagnosis. *Colloids and Surfaces B: Biointerfaces* **2021**, *208*, 112064. https://doi.org/10.1016/j.colsurfb.2021.112064.

(13) Depciuch, J.; Parlinska-Wojtan, M. Comparing Dried and Liquid Blood Serum Samples of Depressed Patients: An Analysis by Raman and Infrared Spectroscopy Methods. *Journal of Pharmaceutical and Biomedical Analysis* **2018**, *150*, 80–86. https://doi.org/10.1016/j.jpba.2017.11.074.

(14) Lindley, S. A.; Zhang, J. Z. Bumpy Hollow Gold Nanospheres for Theranostic Applications: Effect of Surface Morphology on Photothermal Conversion Efficiency. *ACS Appl. Nano Mater.* **2019**, *2* (2), 1072–1081. https://doi.org/10.1021/acsanm.8b02331.

(15) Shukla, R.; Bansal, V.; Chaudhary, M.; Basu, A.; Bhonde, R. R.; Sastry, M. Biocompatibility of Gold Nanoparticles and Their Endocytotic Fate Inside the Cellular Compartment: A Microscopic Overview. *Langmuir* **2005**, *21* (23), 10644–10654. https://doi.org/10.1021/la0513712.

(16) Lee, S.; Chon, H.; Lee, M.; Choo, J.; Shin, S. Y.; Lee, Y. H.; Rhyu, I. J.; Son, S. W.; Oh, C. H. Surface-Enhanced Raman Scattering Imaging of HER2 Cancer Markers Overexpressed in Single MCF7 Cells Using Antibody Conjugated Hollow Gold Nanospheres. *Biosensors and Bioelectronics* **2009**, *24* (7), 2260–2263. https://doi.org/10.1016/j.bios.2008.10.018.

(17) Lee, J. H.; Jeong, H. S.; Lee, D. H.; Beack, S.; Kim, T.; Lee, G.-H.; Park, W. C.; Kim, C.; Kim, K. S.; Hahn, S. K. Targeted Hyaluronate–Hollow Gold Nanosphere Conjugate for Anti-Obesity Photothermal Lipolysis. *ACS Biomater. Sci. Eng.* **2017**, *3* (12), 3646–3653. https://doi.org/10.1021/acsbiomaterials.7b00549.

(18) Phan, H. T.; Heiderscheit, T. S.; Haes, A. J. Understanding Time-Dependent Surface-Enhanced Raman Scattering from Gold Nanosphere Aggregates Using Collision Theory. *J. Phys. Chem. C* **2020**, *124* (26), 14287–14296. https://doi.org/10.1021/acs.jpcc.0c03739.

(19) Lin, K.; Yi, J.; Hu, S.; Liu, J.; Wang, X.; Ren, B. Size Effect on SERS of Gold Nanorods Demonstrated via Single Nanoparticle Spectroscopy | The Journal of Physical Chemistry C. *Jounal of Physical Chemistry C* **2016**, *120* (37), 20806–20813. https://doi.org/10.1021/acs.jpcc.6b02098.

(20) Guarino-Hotz, M.; Zhang, J. Z. Structural Control and Biomedical Applications of Plasmonic Hollow Gold Nanospheres: A Mini Review. *WIREs Nanomedicine and Nanobiotechnology n/a* (n/a), e1694. https://doi.org/10.1002/wnan.1694.

(21) Lee, S.; Chon, H.; Lee, M.; Choo, J.; Shin, S. Y.; Lee, Y. H.; Rhyu, I. J.; Son, S. W.; Oh, C. H. Surface-Enhanced Raman Scattering Imaging of HER2 Cancer Markers Overexpressed in Single MCF7 Cells Using Antibody Conjugated Hollow Gold Nanospheres. *Biosensors and Bioelectronics* **2009**, *24* (7), 2260–2263. https://doi.org/10.1016/j.bios.2008.10.018.

(22) Ko, J.; Lee, S.; Kyu Lee, E.; Chang, S.-I.; Chen, L.; Yoon, S.-Y.; Choo, J. SERS-Based Immunoassay of Tumor Marker VEGF Using DNA Aptamers and Silica-Encapsulated Hollow Gold Nanospheres. *Physical Chemistry Chemical Physics* **2013**, *15* (15), 5379–5385. https://doi.org/10.1039/C2CP43155F.

(23) Esenturk, E. N.; Walker, A. R. H. Surface-Enhanced Raman Scattering Spectroscopy via Gold Nanostars. *Journal of Raman Spectroscopy* **2009**, *40* (1), 86–91. https://doi.org/10.1002/jrs.2084.

(24) Yuan, H.; Khoury, C. G.; Hwang, H.; Wilson, C. M.; Grant, G. A.; Vo-Dinh, T. Gold Nanostars: Surfactant-Free Synthesis, 3D Modelling, and Two-Photon

Photoluminescence Imaging. *Nanotechnology* **2012**, *23* (7), 075102. https://doi.org/10.1088/0957-4484/23/7/075102.

(25) Khoury, C. G.; Vo-Dinh, T. Gold Nanostars For Surface-Enhanced Raman Scattering: Synthesis, Characterization and Optimization. *J. Phys. Chem. C* **2008**, *112* (48), 18849–18859. https://doi.org/10.1021/jp8054747.

(26) Barbosa, S.; Agrawal, A.; Rodríguez-Lorenzo, L.; Pastoriza-Santos, I.; Alvarez-Puebla, R. A.; Kornowski, A.; Weller, H.; Liz-Marzán, L. M. Tuning Size and Sensing Properties in Colloidal Gold Nanostars. *Langmuir* **2010**, *26* (18), 14943–14950. https://doi.org/10.1021/la102559e.

(27) Le Ru, E. C.; Etchegoin, P. G. Quantifying SERS Enhancements. *MRS Bull.* **2013**, *38* (8), 631–640. https://doi.org/10.1557/mrs.2013.158.

(28) Mahmoud, M. A.; Snyder, B.; El-Sayed, M. A. Surface Plasmon Fields and Coupling in the Hollow Gold Nanoparticles and Surface-Enhanced Raman Spectroscopy. Theory and Experiment. *J. Phys. Chem. C* **2010**, *114* (16), 7436–7443. https://doi.org/10.1021/jp9109018.

(29) Lindley, S. A.; Cooper, J. K.; Rojas-Andrade, M. D.; Fung, V.; Leahy, C. J.; Chen, S.; Zhang, J. Z. Highly Tunable Hollow Gold Nanospheres: Gaining Size Control and Uniform Galvanic Exchange of Sacrificial Cobalt Boride Scaffolds. *ACS Appl. Mater. Interfaces* **2018**, *10* (15), 12992–13001. https://doi.org/10.1021/acsami.8b00726.

(30) Ibrahim, A.; Oldhamn, P.; Stokes, D.; Vo-Dinh, T. Determination of Enhancement Factors for Surface-Enhanced FT-Raman Spectroscopy on Gold and

Silver Surfaces - Ibrahim - 1996 - Journal of Raman Spectroscopy - Wiley Online Library. *Journal of Raman Spectroscopy* **1996**, *27* (12), 887–891. https://doi.org/10.1002/(SICI)1097-4555(199612)27:12<887::AID-JRS46>3.0.CO;2-2.

(31) Wang, L.; Xiong, W.; Nishijima, Y.; Yokota, Y.; Ueno, K.; Misawa, H.; Bi, G.; Qiu, J. Spectral Properties and Mechanism of Instability of Nanoengineered Silver Blocks. *Opt. Express* **2011**, *19* (11), 10640. https://doi.org/10.1364/OE.19.010640.

(32) Li, H.-J.; Zhang, A.-Q.; Hu, Y.; Sui, L.; Qian, D.-J.; Chen, M. Large-Scale Synthesis and Self-Organization of Silver Nanoparticles with Tween 80 as a Reductant and Stabilizer. *Nanoscale Research Letters* **2012**, *7* (1), 612. https://doi.org/10.1186/1556-276X-7-612.

(33) Hillenkamp, M.; Domenicantonio, G. D.; Eugster, O.; Félix, C. Instability of Ag Nanoparticles in SiO2at Ambient Conditions. *Nanotechnology* **2006**, *18* (1), 015702. https://doi.org/10.1088/0957-4484/18/1/015702.

(34) Tiwari, P.; Das, G. M.; Dantham, V. R. Optical Properties of Au-Ag Bimetallic Nanoparticles of Different Shapes for Making Efficient Bimetallic-Photonic Whispering Gallery Mode Hybrid Microresonators. *Plasmonics* **2020**, *15* (5), 1251–1260. https://doi.org/10.1007/s11468-020-01141-7.

(35) M. Fales, A.; Vo-Dinh, T. Silver Embedded Nanostars for SERS with Internal Reference (SENSIR). *Journal of Materials Chemistry C* **2015**, *3* (28), 7319–7324. https://doi.org/10.1039/C5TC01296A.

(36) Zhang, W.; Liu, J.; Niu, W.; Yan, H.; Lu, X.; Liu, B. Tip-Selective Growth of Silver on Gold Nanostars for Surface-Enhanced Raman Scattering. *ACS Appl. Mater. Interfaces* **2018**, *10* (17), 14850–14856. https://doi.org/10.1021/acsami.7b19328.

(37) Liu, Y.; Zhang, W.; Phan, T. H.; Chrzanowski, W.; Rodger, A.; Wang, Y. Positively Charged Gold–Silver Nanostar Enabled Molecular Characterization of Cancer Associated Extracellular Vesicles. *Anal. Methods* **2020**, *12* (48), 5908–5915. https://doi.org/10.1039/D0AY01770A.

(38) Liu, R.; Jiang, L.; Yu, Z.; Jing, X.; Liang, X.; Wang, D.; Yang, B.; Lu, C.; Zhou, W.; Jin, S. MXene (Ti3C2T)-Ag Nanocomplex as Efficient and Quantitative SERS Biosensor Platform by in-Situ PDDA Electrostatic Self-Assembly Synthesis Strategy. *Sensors and Actuators B: Chemical* **2021**, *333*, 129581. https://doi.org/10.1016/j.snb.2021.129581.

(39) Li, Y.; Jiang, L.; Zou, Y.; Song, Z.; Jin, S. Highly Reproducible SERS Sensor Based on Self-Assembled Au Nanocubic Monolayer Film for Sensitive and Quantitative Detection of Glutathione. *Applied Surface Science* **2021**, *540*, 148381. https://doi.org/10.1016/j.apsusc.2020.148381.

(40) Zhou, H.; Yang, D.; Ivleva, N. P.; Mircescu, N. E.; Niessner, R.; Haisch, C. SERS Detection of Bacteria in Water by in Situ Coating with Ag Nanoparticles. *Anal. Chem.* **2014**, *86* (3), 1525–1533. https://doi.org/10.1021/ac402935p.

(41) Tan, S.; Erol, M.; Attygalle, A.; Du, H.; Sukhishvili, S. Synthesis of Positively Charged Silver Nanoparticles via Photoreduction of $AgNO_3$ in Branched

Polyethyleneimine/HEPES Solutions. *Langmuir* **2007**, *23* (19), 9836–9843. https://doi.org/10.1021/la701236v.

(42) Huang, G. G.; Han, X. X.; Hossain, M. K.; Ozaki, Y. Development of a Heat-Induced Surface-Enhanced Raman Scattering Sensing Method for Rapid Detection of Glutathione in Aqueous Solutions. *Anal. Chem.* **2009**, *81* (14), 5881–5888. https://doi.org/10.1021/ac900392s.

(43) Adams, S.; Thai, D.; Mascona, X.; Schwartzberg, A. M.; Zhang, J. Z. Key Factors Affecting the Reproducibility of Synthesis and Growth Mechanism of Near-Infrared Absorbing Hollow Gold Nanospheres. *Chem. Mater.* **2014**, *26* (23), 6805–6810. https://doi.org/10.1021/cm5033892.

(44) Schwartzberg, A. M.; Olson, T. Y.; Talley, C. E.; Zhang, J. Z. Synthesis, Characterization, and Tunable Optical Properties of Hollow Gold Nanospheres. *The Journal of Physical Chemistry. B* **2006**, *110* (40), 19935–19944. https://doi.org/10.1021/jp062136a.

(45) Olson, T. Y.; Schwartzberg, A. M.; Orme, C. A.; Talley, C. E.; O'Connell, B.; Zhang, J. Z. Hollow Gold−Silver Double-Shell Nanospheres: Structure, Optical Absorption, and Surface-Enhanced Raman Scattering. *J. Phys. Chem. C* **2008**, *112* (16), 6319–6329. https://doi.org/10.1021/jp7116714.

(46) Sonay, A. Y.; Çağlayan, A. B.; Çulha, M. Synthesis of Peptide Mediated Au Core–Ag Shell Nanoparticles as Surface-Enhanced Raman Scattering Labels. *Plasmonics* **2012**, *7* (1), 77–86. https://doi.org/10.1007/s11468-011-9278-4.

(47) Palik, E. D. *Handbook of Optical Constants of Solids*; Academic Press, 1998.

(48) Pierre, M. C. S.; Haes, A. J. Purification Implications on SERS Activity of Silica Coated Gold Nanospheres. *Anal. Chem.* **2012**, *84* (18), 7906–7911. https://doi.org/10.1021/ac3016517.

(49) Preciado-Flores, S.; Wang, D.; A. Wheeler, D.; Newhouse, R.; K. Hensel, J.; Schwartzberg, A.; Wang, L.; Zhu, J.; Barboza-Flores, M.; Z. Zhang, J. Highly Reproducible Synthesis of Hollow Gold Nanospheres with near Infrared Surface Plasmon Absorption Using PVP as Stabilizing Agent. *Journal of Materials Chemistry* **2011**, *21* (7), 2344–2350. https://doi.org/10.1039/C0JM03690K.

(50) Pu, Y.-C.; Song, F.; Zhang, W.; Lindley, S.; Adams, S.; Zhang, J. Z. Size-Tunable Synthesis of Hollow Gold Nanospheres through Control of Reaction Temperature. *Particle & Particle Systems Characterization* **2017**, *34* (8), 1600255. https://doi.org/10.1002/ppsc.201600255.

(51) Chirico, G.; Borzenkov, M.; Pallavicini, P. *Gold Nanostars*; SpringerBriefs in Materials; Springer International Publishing: Cham, 2015. https://doi.org/10.1007/978-3-319-20768-1.

(52) Khoury, C. G.; Vo-Dinh, T. Gold Nanostars For Surface-Enhanced Raman Scattering: Synthesis, Characterization and Optimization. *J. Phys. Chem. C* **2008**, *112* (48), 18849–18859. https://doi.org/10.1021/jp8054747.

(53) Fales, A. M.; Yuan, H.; Vo-Dinh, T. Development of Hybrid Silver-Coated Gold Nanostars for Nonaggregated Surface-Enhanced Raman Scattering. *J. Phys. Chem. C* **2014**, *118* (7), 3708–3715. https://doi.org/10.1021/jp4091393.

(54) Liu, X.; Atwater, M.; Wang, J.; Huo, Q. Extinction Coefficient of Gold Nanoparticles with Different Sizes and Different Capping Ligands. *Colloids and Surfaces B: Biointerfaces* **2007**, *58* (1), 3–7. https://doi.org/10.1016/j.colsurfb.2006.08.005.

(55) Fales, A. M.; Yuan, H.; Vo-Dinh, T. Development of Hybrid Silver-Coated Gold Nanostars for Nonaggregated Surface-Enhanced Raman Scattering. *J. Phys. Chem. C* **2014**, *118* (7), 3708–3715. https://doi.org/10.1021/jp4091393.

(56) Khan, S. S.; Mukherjee, A.; Chandrasekaran, N. Impact of Exopolysaccharides on the Stability of Silver Nanoparticles in Water. *Water Research* **2011**, *45* (16), 5184–5190. https://doi.org/10.1016/j.watres.2011.07.024.

(57) Barathithasan, R. Electrophoretic Light Scattering (Zeta Potential).

(58) Le Ru, E. C.; Etchegoin, P. G. Quantifying SERS Enhancements. *MRS Bull.* **2013**, *38* (8), 631–640. https://doi.org/10.1557/mrs.2013.158.

(59) Allen, A. C.; Efrem, M.; Mahalingam, U.; Guarino-Hotz, M.; Foley, A. R.; Raskatov, J. A.; Song, C.; Lindley, S. A.; Li, J.; Chen, B.; Zhang, J. Z. Hollow Gold Nanosphere Templated Synthesis of PEGylated Hollow Gold Nanostars and Use for SERS Detection of Amyloid Beta in Solution. *J. Phys. Chem. B* **2021**. https://doi.org/10.1021/acs.jpcb.1c06776.

(60) Zhao, J.; Pinchuk, A. O.; McMahon, J. M.; Li, S.; Ausman, L. K.; Atkinson, A. L.; Schatz, G. C. Methods for Describing the Electromagnetic Properties of Silver and Gold Nanoparticles. *Acc Chem Res* **2008**, *41* (12), 1710–1720. https://doi.org/10.1021/ar800028j.

(61) Draine, B. T.; Flatau, P. J. Discrete-Dipole Approximation For Scattering Calculations. *J. Opt. Soc. Am. A, JOSAA* **1994**, *11* (4), 1491–1499. https://doi.org/10.1364/JOSAA.11.001491.

(62) Draine, B. T. The Discrete-Dipole Approximation and Its Application to Interstellar Graphite Grains. *ApJ* **1988**, *333*, 848. https://doi.org/10.1086/166795.

(63) Zhang, J. Z.; Wheeler, D.; Schwartzberg, A.; Jianying, S. Basics and Practice of Surface Enhanced Raman Scattering (SERS) and Tip Enhanced Raman Scattering (TERS) - IOS Press. *Biomedical Spectroscopy and Imaging* **2014**, *3* (2), 121–159. https://doi.org/10.3233/BSI-140086.

(64) Ameer, F. S.; Pittman, C. U.; Zhang, D. Quantification of Resonance Raman Enhancement Factors for Rhodamine 6G (R6G) in Water and on Gold and Silver Nanoparticles: Implications for Single-Molecule R6G SERS. *J. Phys. Chem. C* **2013**, *117* (51), 27096–27104. https://doi.org/10.1021/jp4105932.

(65) Tartaj, P.; González-Carreño, T.; Serna, C. J. Single-Step Nanoengineering of Silica Coated Maghemite Hollow Spheres with Tunable Magnetic Properties. *Advanced Materials* **2001**, *13* (21), 1620–1624. https://doi.org/10.1002/1521-4095(200111)13:21<1620::AID-ADMA1620>3.0.CO;2-Z.

(66) Colthup, N. B.; Daly, L. H.; Wiberley, S. E. *Introduction to Infrared and Raman Spectroscopy*, 2d ed.; Academic Press: New York, 1975.

(67) McFarland, A. D.; Young, M. A.; Dieringer, J. A.; Van Duyne, R. P. Wavelength-Scanned Surface-Enhanced Raman Excitation Spectroscopy. *J. Phys. Chem. B* **2005**, *109* (22), 11279–11285. https://doi.org/10.1021/jp050508u.

Chapter Three

3 Near-Infrared Light Absorbing Silver Coated Hollow Gold Nanostars for Surface Enhanced Raman Scattering Detection of Bovine Serum Albumin Using Capping Ligand Exchange

3.1 Abstract

Methylammonium lead bromide perovskite magic-sized clusters and quantum dots were synthesized using a new heated ligand assisted reprecipitation (HLARP)

technique using organic amines and acids as capping ligands. The optical properties of these nanoparticles were analyzed using UV-vis electronic absorption and photoluminescent spectroscopy. Varying the temperature of the precursor solution while keeping the antisolvent temperature consistent allows for tuning between perovskite magic-sized clusters (MSCs) and quantum dots (PQDs) without the need to use excessive concentrations of capping ligand. Higher precursor solution temperatures favor MSCs, while lower temperatures favor PQDs. Furthermore, increasing the temperature of the system shifts the original emission band from 436 nm to 453 nm, potentially through the introduction of surface defects. Low frequency Raman spectroscopy reveals that MSCs have similar vibrational frequencies to bulk perovskite. Electrospray mass spectrometry and infrared spectroscopy were used to probe the ligands on the surface of the MSCs, indicating that amine is the primary capping ligand and the surface presumably cation rich.

3.2 Introduction

Perovskite quantum dots (PQDs) have been studied extensively for their unique properties, such as high photoluminescence (PL) quantum yield and tunable optical properties.[1] Their emission can be easily tuned over the entire visible spectrum by controlling the crystal size,[2,3] capping ligand,[4,5] and elemental composition.[6,7] These distinctive optoelectronic properties make them promising substrates for applications in the fields of photovoltaics for light-emitting devices,[8,9] photodetectors,[10,11] and sensing.[12,13] PQDs' tunable emission stems from their quantum confinement and high surface to volume (S/V) ratio.[14,15] By comparison, perovskite magic-sized clusters (MSCs) are smaller, more monodispersed, and have narrower, bluer optical absorption bands. [4,5,16–21] They are often described as kinetic products or stable intermediaries of PQDs.[22] Understanding the relationship between PQDs and MSCs can aid in fundamental studies of the growth mechanism of quantum dots and bulk perovskite.

As MSCs have such a high S/V ratio, they are susceptible to surface dangling bonds and defect sites leading to instability.[23,24] Thus, MSCs are typically formed by increasing the concentration of molecular capping ligands with appropriate anchoring functional groups to increase surface protection. To date, a significant amount of work has been put into tuning between MSCs and PQDs by varying ligand composition and concentration.[5,18,25,26] These syntheses typically employ ligand-assisted reprecipitation (LARP) at room temperature. For instance, Xu *et al.* demonstrated that an increase in trivalent metal hydrated nitrate coordination complexes yields monodispersed MSCs.[4] Using a similar process, Li *et al.* demonstrated that increasing the concentration of organic acid and amine ligands also yields MSCs exclusively. Moreover, increasing the concentration of organic amine alone also favors the production of MSCs.[5] It was determined that amine was likely a strong capping ligand, which allowed it to more effectively passivate a smaller particle. However, nanocrystal formation is dependent on a multitude of variables. By varying the temperature, quantum dots have been synthesized using the hot injection method.[27] This requires high temperatures (120-140°C) and are typically performed in an air-free environment, heating both precursor and antisolvent solutions, but typically results in an increase of monodispersity and particle stability.[28,29] However, for MSCs, other variables have barely been explored, and little research has been done using temperature for tuning.[30] In the Gibb's Thompson equation, the temperature and critical radius are inversely proportional.

Thus, increasing temperature results in smaller nanoparticles by imparting more energy to the surface, allowing them to stabilize at smaller sizes.[31] However, in the synthesis presented herein, the solution is rapidly cooled from an elevated temperature to around 20°C. Rapid cooling during a crystallization process decreases the size of crystal formation by increasing the number of collisions and speeding up the formation time scale.[32] Moreover, rapid cooling increases the number of nucleation sites, encouraging many particles to form at the same time and more rapidly depleting available resources, causing smaller particles to form.[33] However, rapid cooling can cause more defects in the crystal structure, as it forms the kinetic, not thermodynamic, product.[34] Defects can lead to modifications in the Stokes shift, where emission occurs a at a longer wavelength than absorption,[35] and defect engineering can be useful to tune the optical properties of nanoparticles for different applications like solar cells or photovoltaics.[36]

In this work, MSCs and PQDs are synthesized using a new heated ligand assisted reprecipitation (HLARP) technique using organic amines and acids as capping ligands. The optical properties of these nanoparticles were analyzed using UV-vis and photoluminescent spectroscopy. Higher precursor solution temperatures favor MSCs, while lower temperatures favor PQDs. Moreover, increasing the temperature of the system allows the formation of stable states of MSCs to be tuned from the original emission band of 436 nm to 453 nm. Low frequency Raman was used to gain structural insights. Electrospray mass spectrometry and Infrared spectroscopy were used to determine that MSCs are primarily capped with amine, indicating that the surface of the MSCs is cation rich.

3.3 Methods

3.3.1 Materials

Methylammonium bromide (MABr, 99.9%, Greatcell Solar), $PbBr_2$ (99.999%, Alfa Aesar), valeric acid (99.0% Alfa Aesar), *n*-octanoic acid (98.0%, Tokyo Chemical Industry), oleic acid (90%, Sigma Aldrich), *n*-octylamine (98.0%, Tokyo Chemical Industry), *N*,*N*-dimethylformamide (DMF, 99.9%, Fisher Scientific), hydrobromic acid (HBr, 48%, Honeywell) and toluene (99.9%, Fisher Scientific) were commercially available. All chemicals were used as received without any further purification.

3.3.2 Synthesis of $MAPbBr_3$ PQDs and MSCs

In a modified LARP synthesis process of PQDs and MSCs, MABr (0.080 mmol, 9.0 mg), $PbBr_2$ (0.20 mmol, 73.0 mg), and 400 μL of DMF were added to a borosilicate vial, and the solution was sonicated in a water bath between 20°C-70°C until all solid dissolved. Next, organic acid (oleic, octyl, or valeric) of varying amounts was added to the solution and sonicated at this temperature for 30 s. Then, amine (oleyl or octyl) of equimolar amounts was added to the solution and sonicated for 30 s at temperature. One hundred microliters of the precursor solution were injected at a fast rate into 5.0 mL of toluene under vigorous stirring. Particles were washed through centrifugation, first at 5000 rpm, retaining the supernatant, and then twice at 10,000 rpm keeping the pellet.

Control experiments were conducted by repeating this process without the addition of oleic acid, doubling the amount of oleic acid, or replacing oleic acid with an equimolar amount of hydrobromic acid.

3.3.3 Spectroscopic Measurements

Ultraviolet-visible (UV–vis) absorption spectra were measured with an Agilent Technologies Cary 60 UV–vis spectrophotometer, and the PL spectra were measured using a Cary Eclipse spectrofluorometer using a quartz 700 μL microcuvette at room temperature and an excitation wavelength of 400 nm. FTIR spectra were obtained with a PerkinElmer FTIR spectrometer (Spectrum One, a spectral resolution of 4 cm^{-1}), where the samples were prepared by dropping the $MAPbBr_3$ nanoparticle solutions onto salt plates for analysis.

3.3.4 Mass Spectrometry

The washed particles with less than 10 mM concentration in 50% methanol were analyzed by direct sample injection from a syringe needle with 10 μl/min flow rate on a Thermo Electron Finnigan LTQ mass spectrometer positive mode or negative mode over a full scan range of *m/z* 50–1000. The voltage was set to 5.0 kV with a capillary temperature was 275°C. Data were analyzed by using the XCalibur software.

3.4 Results and Discussion

3.4.1 Tuning Between PQDs and MSCs

$MAPbBr_3$ nanoparticles of varying sizes capped with 0.15 mmol of oleylamine and oleic acid were synthesized using a new heated ligand assisted reprecipitation (HLARP) method. Precursor solution was heated to 20, 40, 60, or 70ºC and injected into room temperature anti-solvent. Nanoparticles formed at different precursor temperatures with 0.15 mmol of capping ligand are subsequently labeled MSC20A-MSC70A. Their UV-Vis absorption and PL spectra are shown in Figure 3-1. Three absorption bands are observed for MSC20A and MSC40A at 430 nm, 450 nm, 519 nm. In the case of MSC60A and MSC70A, there is only one absorption band at 430 nm. According to previous studies, the range of 450-520 nm broader excitonic absorption peaks are attributed to PQDs.[5,37,38] while the single sharp excitonic absorption peak at around 430 nm is assigned to MSCs.[5,25,26,39]

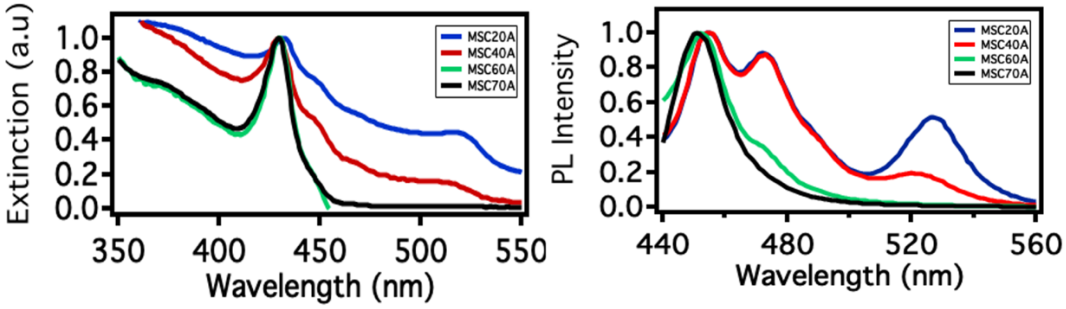

Figure 3-7 (left) Normalized UV-vis absorption (right) Normalized PL spectra of $MAPbBr_3$ PQDs and MSCs capped with 0.15 mmol of oleylamine and oleic acid with various precursor temperatures.

In the PL spectra, three emission peaks at 455 nm, 473 nm, and 528 nm were observed for MSC20A and MSC40A. Two emission peaks are observed for MSC60A at 450 nm and 473 nm. Finally, only one monodispersed emission peak at 453 nm was observed for MSC70A. The PL emission peak at 528 nm and 473 nm corresponds to PQDs of differing sizes, while the strong and sharp excitonic emission peak at 450 nm is assigned to MSCs. It should be noted that MSCs synthesized with the HLARP method use 15% less capping ligand than previously reported LARP methods.[5] HLARP MSCs formed with less capping ligand with rapid cooling and exhibit a Stokes shift of 23 nm, compared to previous reports with 6 nm shift produced with the LARP method with excess octylamine and octanoic acid at room temperature.[5] Details of the UV–vis absorption and PL emission peaks of $MAPbBr_3$ PQDs and MSCs with various ligands at differing temperatures are summarized in the Supporting Information.

This synthesis is predicated on the principles that increasing the temperature increases the surface free energy necessary to decrease the critical radius[31,40] of a nanoparticle and that rapid cooling causes crystal formation to occur on a faster time scale.[41–43] Thus, increasing the temperature of the precursor solution increases this free energy, allowing for the formation of smaller particles. Moreover, increasing the temperature increases the solubility of the capping ligands allowing for better nanoparticle/capping ligand interaction, leading to more effective passivation, which helps to stabilize at a smaller size.[44] Additionally, by injecting heated precursor into a room temperature anti-solvent, the solution supersaturates due to two factors, both solvent and temperature changes.[45] Thus, the equilibrium is shifted towards crystallization on a shorter timescale than those synthesized using the LARP method. Rapid cooling also facilitates the production of more nucleation sites, which decreases the concentration of precursors, inhibits Ostwald ripening, and thus forms smaller particles.[33] Since MSCs synthesized using HLARP form more rapidly, they are not the most thermodynamically stable product but a stable intermediary.

The HLARP synthesis of $MAPbBr_3$ PQDs and MSCs was repeated using double the amount of oleic acid and oleylamine, 0.30 mmol, at a lower temperature range of 20-60ºC. Figure 3-2 shows UV-vis absorption and PL spectra with a similar trend. Here there are fewer absorption bands compared to 0.15 mmol of capping ligand as shown in Figure 3-1. MSC20B-60B produce one major absorption band around 427 nm. The intensity of the shoulder from 470 nm to 510 nm, indicating PQDs, diminishes with the increase in temperature of the precursor solution. As expected, the increase in capping ligand increases the production of MSCs. However, it also arrested the production of the 450 nm absorbing particles. The growth of MSCs is typically described as discrete, where there is a thermodynamic barrier to the growth of a larger size.[46] It is possible that the addition of excess capping ligand is preventing collisions that provide energy to overcome this barrier and form a larger crystal.

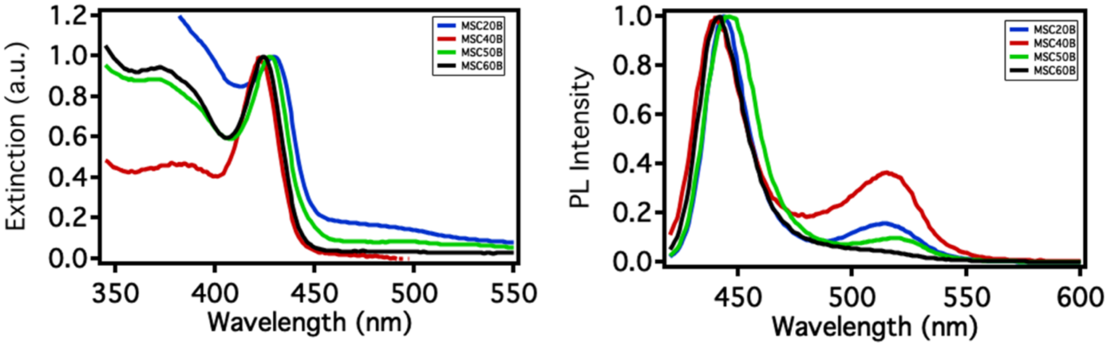

Figure 3-8 (left) Normalized UV-vis absorption (right) Normalized PL spectra of $MAPbBr_3$ PQDs and MSCs capped with 030 mmol of oleylamine and oleic acid with various precursor temperatures.

In the PL spectra, there is one broad emission peak at 515 nm, attributed to PQDs, and one sharp peak ranging from 440 nm to 446 nm associated with MSCs. As the temperature increased, the 515 nm peak disappeared, and the 446 nm peak blue shifts to 440 nm. MSC60B show one narrow peak at 440 nm. Increasing the capping ligand concentration of the synthesis blue shifted the MSCs, which likely indicates a reduction in particle radius. Here monodispersity is achieved at a lower temperature. However, their Stokes shift is 13 nm and thus still larger than many reported LARP methods,[4,5,17] but smaller than the 23 nm shift of MSC70A.

3.4.2 Tunability of MSCs

The monodispersed MSCs from Figures 3-1 and 2 are compared directly in Figure 3-3 to the original LARP synthesis and show the tunability of the MSCs emission band. A characteristic feature of MSCs is their discrete, monodispersed size.[5,45] There is a 17 nm difference in the emission position between the MSC70A and the MSCs from the original LARP method (Figure 3-3D), which emit at 453 nm and 436 nm, respectively. The Stokes shift also increases from 13 nm to 23 nm using the HLARP synthesis. MSC60B emission peak is red shifted by 4 nm from the original LARP MSCs, but both have a Stokes shift of 13 nm.

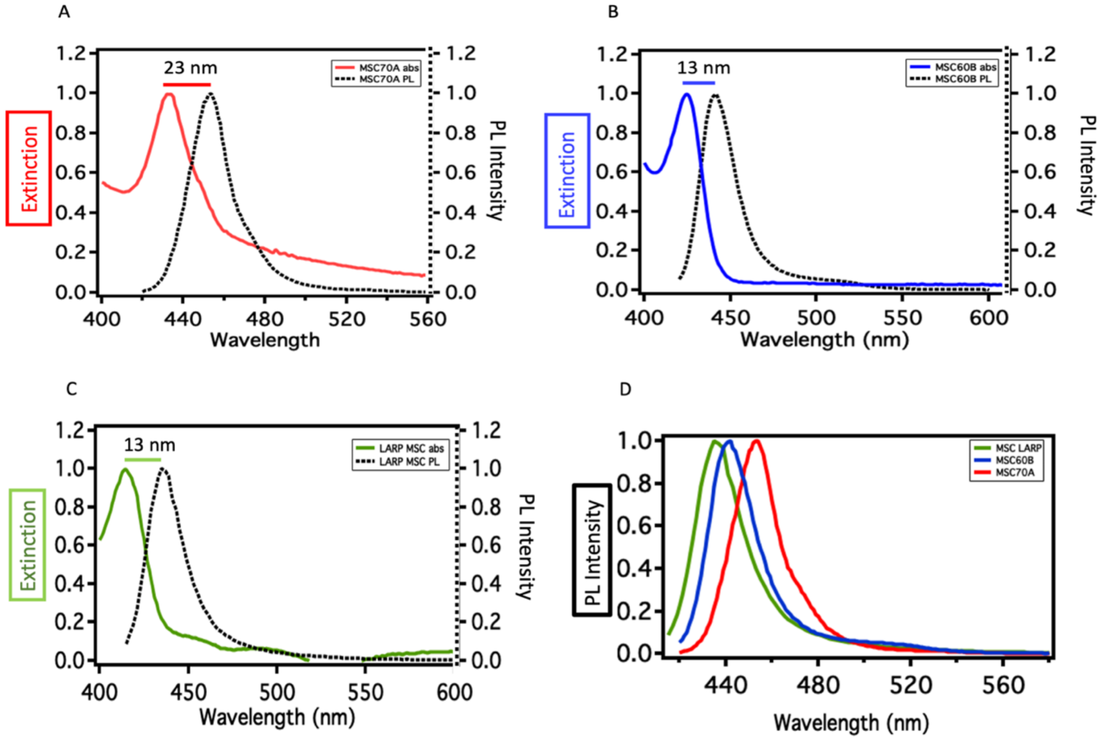

Figure 3-9 Combined normalized UV-vis and PL data for (A) MSC70A (B) MSC60B (C) $MAPbBr_3$ oleylamine and oleic acid synthesized using the original LARP method (D) Normalized PL spectra of MSC70A, MSC60B, and LARP MSCs compared directly.

The optical properties of these nanoparticles are governed by quantum confinement,[14] and thus, changing their size will affect their bandgap. Size-dependent bandgap can be made with the Brus method,[38,39,47]

$$E_g(MSCs) = E_g(bulk) + \frac{h^2}{8r^2}\left(\frac{1}{m_e} + \frac{1}{m_h}\right) \tag{2}$$

where $E_g(MSCs)$ is the band gap of MSCs, E_g is the bandgap of bulk perovskite, h is Planck's constant, r is the radius, m_e is the mass of the electron, m_h is the mass of the hole. From previous reports, E_g (bulk) was previously determined to be 2.30 eV[48] and $\left(\frac{1}{m_e} + \frac{1}{m_h}\right)$ was determined to be $2.37\text{x}10^{30}\ \frac{1}{\text{Kg}}$.[21]

The sizes of MSCs LARP, MSC60B, and MSC70A were calculated to be 3.05, 3.13, and 3.41nm, respectively. As MSCs have such a high S/V ratio, they are particularly vulnerable to trap states formed through surface defects.[49] By synthesizing MSCs with less capping ligand, a higher temperature is required to form monodispersed MSCs. Increasing the temperature also introduces rapid cooling, which has been shown to introduce more defects into the nanoparticle.[34,36] Thus, they likely have more crystal defects that create trap states, slow radiative recombination, and create the larger Stokes shift. By contrast, using a larger concentration of capping ligand, a lower temperature was needed to synthesize MSCs with a bluer shifted emission for MSC60B. The MSCs surface defects were more effectively passivated, and crystal formation could occur on a slightly larger timescale. As these crystals are likely more "perfect", they have less defects to create trap states. Thus, radiative recombination occurs without as much electron-phonon coupling.[50] This would agree with the previously reported MSCs synthesized with excess capping ligand forming at room temperature. They are likely to have a decrease in defects or trap states, resulting in a smaller Stokes shift. This tunability allows them to be optimized for different applications. A larger Stokes shift is desirable for solar cell applications to minimize photon reabsorption,[51,52] while a smaller Stokes shift is more applicable for photovoltaics to achieve a higher power conversion efficiency.[52,53]

3.4.3 Structural Properties

Figure 3-4 shows the low frequency Raman of the MSCs in solution. The MSCs vibrational modes were compared to methylammonium lead bromide bulk. The characteristic mode at 53 cm^{-1} indicates octahedra distortion[54] and the bending of lead halide bonds.[55] The modes at 69 cm^{-1} and 94 cm^{-1} are due to lurching methylammonium,[54] and the mode at 107 cm^{-1} is due to methylammonium libations.[55] Comparing to theoretical spectra of $MAPbBr_3$ in its tetrahedral-1, tetrahedral-2, and orthorhombic phases, the 94 cm^{-1} is well accounted for in tetrahedral-2 formation and in the octahedral, not in the tetrahedral-1. All four modes of the nanocrystal are in good agreement with bulk methylammonium lead bromide.[54] This is somewhat unexpected since, given their small size, one might expect higher vibrational frequencies than bulk. Future theoretical studies may help to provide some explanation or new insight into this.

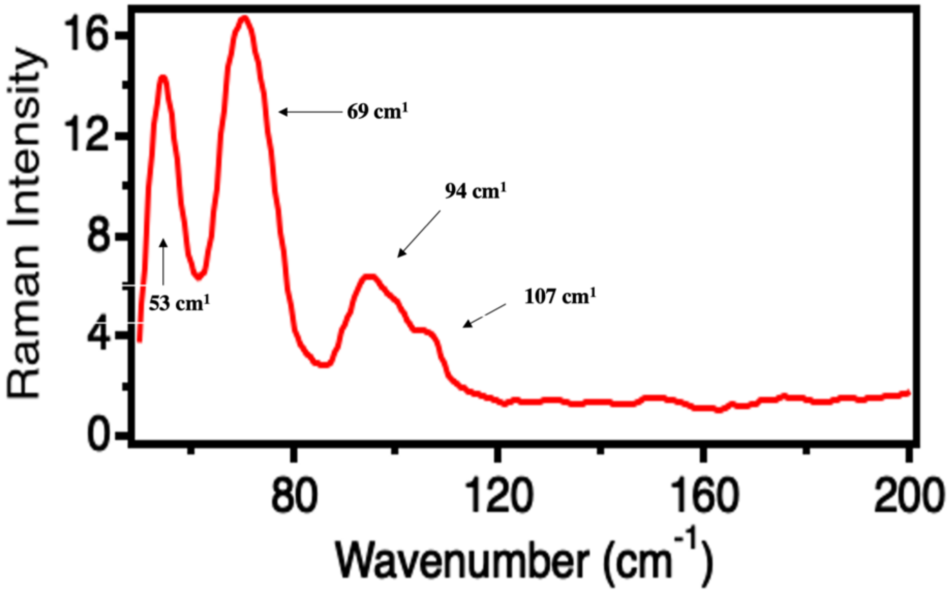

Figure 3-10 Low frequency Raman spectrum of MAPbBr$_3$ MSCs in solution measured with 785 nm laser.

3.4.4 Surface Ligand Binding

Figure 3-5 compares the IR spectra of oleic acid, oleylamine, and MSCs emitting at 453 nm. Oleylamine shows characteristic modes of oleyl groups. The peaks at 2851–2853 and 2922–2925 cm^{-1} are due to the symmetric and asymmetric CH$_2$ stretching modes, respectively, and peaks at 3003–3006 cm^{-1} are assigned to the ν(C–H) mode of the C–H bond adjacent to the C=C bond. It also shows C-H bending modes at 1468 cm^{-1}. The spectrum is distinguished by the sharpness of the modes at 2922–2925 cm^{-1} and 2851–2853 cm^{-1}.[56]

Oleic acid similarly shows the characteristic modes of oleyl groups at 2851–2853, 2922–2925 cm^{-1}, 3003–3006 cm^{-1}, and 1468 cm^{-1}. However, it has characteristic modes of the carboxylic acid group. The ν(C=O) mode is observed as a sharp, strong peak at 1707 cm^{-1}, an additional C-H bending mode at 1450 cm^{-1}, and a broad shoulder in the region between 3100 and 3500 cm^{-1}, which could be assigned to dimers of oleic acid in a bilayer structure.[56]

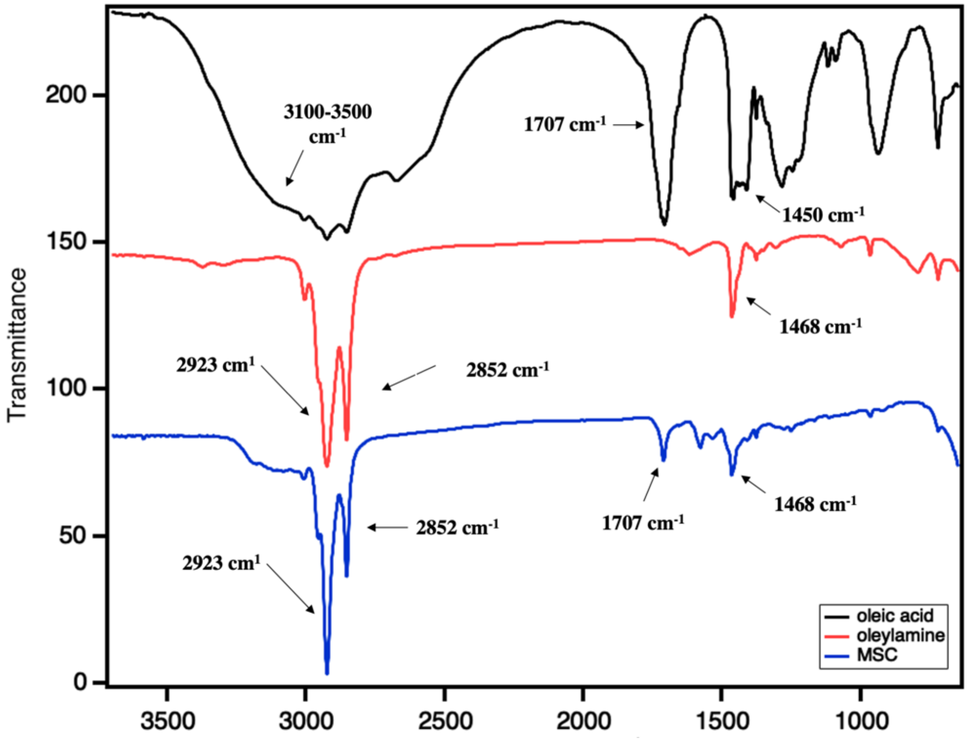

Figure 3-11 IR spectra of oleylamine (red), oleic acid (black), and MSCs (blue).

The FT-IR spectra of MSCs show all the oleyl group modes. It also shows a peak at 1707 cm^{-1} that can be attributed to the carbonyl group of oleic acid. The low intensity of the peak indicates a low concentration. The spectrum also shows the characteristic sharp peaks at 2923 cm^{-1} and 2852 cm^{-1}, characteristic of oleylamine, suggesting both amine and acid ligands are present on the surface.[57] Moreover, a combination of the protonated and deprotonated form of each capping ligand is likely to interact due to a proton transfer reaction between the two. However, the protonated and deprotonated forms of these compounds are difficult to distinguish using IR. Moreover, the IR alone is unable to quantify the molar ratio of ligands on the surface thus mass spectrometry was employed to gain insight.[56]

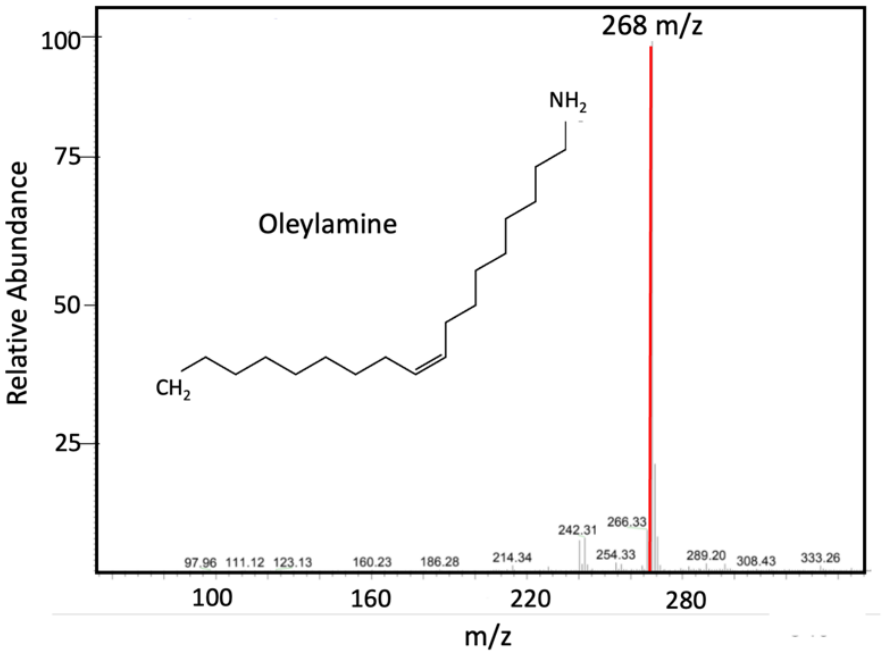

Figure 3-6 Positive Scan Mode Mass Spectrum of MSCs capped with oleylamine and oleic acid.

Figure 3-6 shows the positive ion mass spectrum of MSCs emitting at 453 nm. Washed particles were injected directly into an ESI mass spectrometer and positive and negative ion spectra were obtained. The positive ion spectrum shows a characteristic peak at 268 m/z, indicating ionized oleylamine or oleyl ammonium (Figure 3-6). As equimolar amounts of oleylamine and oleic acid were used in the synthesis of these MSCs, an oleic acid or oleate peak would be expected. However, the requisite 281 m/z peak is not present on the negative ion spectrum. This is intriguing as common passivation theories of metal halide perovskites accept the cocktail approach, using many types of capping ligands to passivate different defects.[24] While oleic acid is still present on the surface, as shown by the IR spectrum, oleylamine or oleyl ammonium is the predominant capping ligand. To confirm these findings, MSCs were synthesized with exclusively oleylamine and oleyl ammonium as capping ligands. Oleylamine alone could effectively result in the generation of MSCs. Two control experiments were conducted using oleyl ammonium, which was generated from oleylamine using an excess of oleic acid and with an equimolar amount of hydrobromic acid. The acidified mixtures yielded a mixture of MSCs and PQDs. Thus, acidification of oleylamine does not yield monodispersed MSCs. Since oleylamine by itself does yield MSCs, it is likely the primary capping ligand.

These results are consistent with Liu *et al*.'s findings that increased oleylamine yields more MSCs.[5] However, here we confirm that oleylamine is the primary capping ligand bound on the surface of the MSCs. Since capping ligands are used to passivate surface defects, we can infer a significant amount about the surface chemistry based on which capping ligand is on the surface. The FTIR confirms the presence of oleylamine and a small amount of oleic acid. The presence of oleic acid is shown in the FTIR, but nothing about its binding to the surface is known. As oleylamine and oleic acid interact via an acid-base neutralization to form oleyl ammonium and oleate,[5] thus we likely have oleyl ammonium and oleate present on the surface as well. As is consistent with the literature, the combination of these ligands will effectively passivate several anionic and cationic defects more effectively than one ligand alone.[24] However, with such a large, confirmed presence of oleylamine present on the surface, the MSC surface is likely cation rich as oleylamine acts as an electron donator.[49]

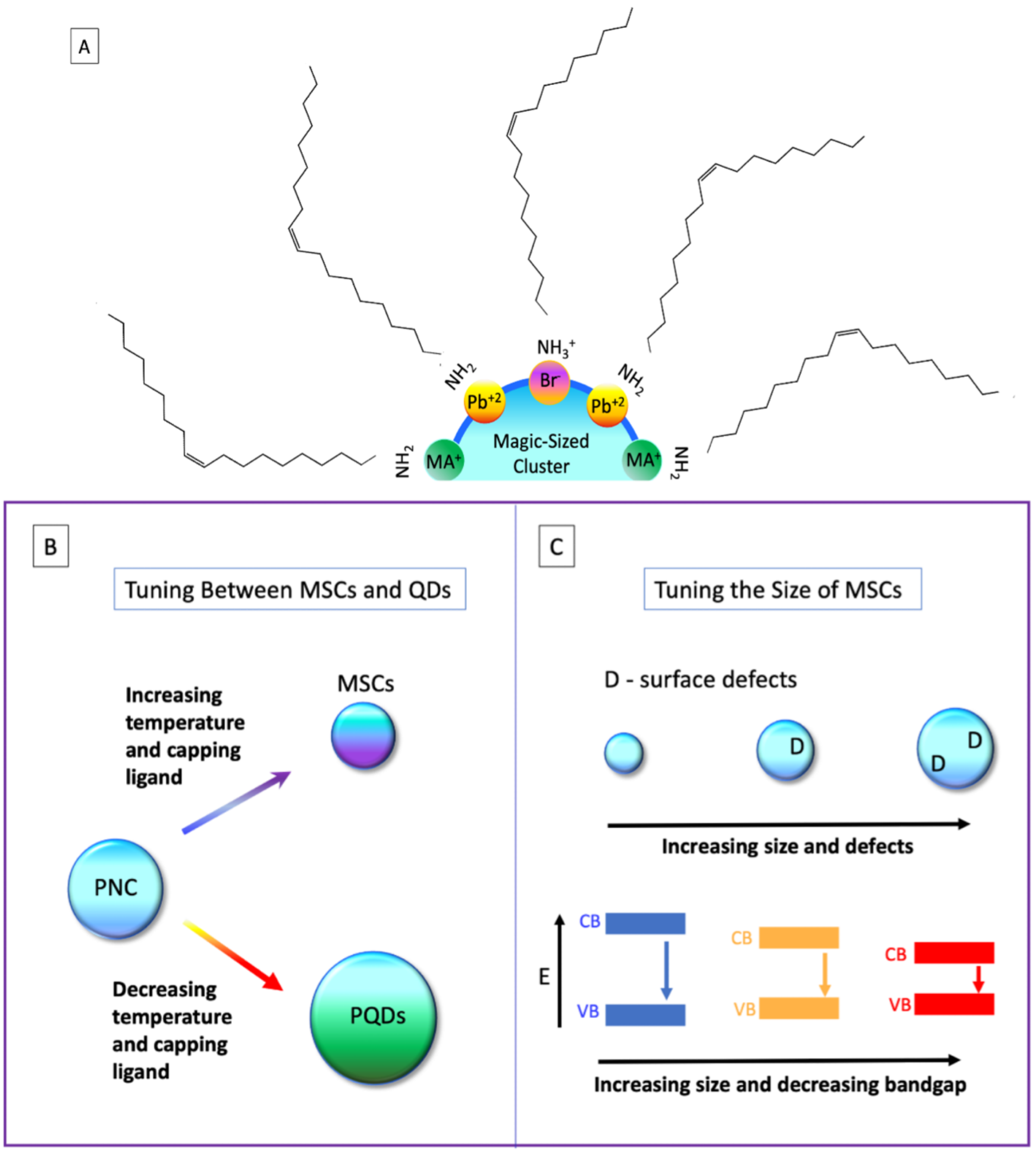

Figure 3-7 (A) Potential cationic surface dangling bonds capped by oleylamine and oleyl ammonium on the surface of MSCs (B) Describing growth mechanism to tune

between MSCs and PQDs using Temperature, Capping Ligand Concentration, and Rapid Cooling (C) Comparison of Size of MSCs, defects, and bandgap, PNC-perovskite nanocrystal.

As shown in Figure 3-7A, we propose that the surface of MSCs is primarily capped with oleylamine and a small amount of oleyl ammonium. Different defects are usually anticipated for perovskite nanocrystals, such as MSCs and PQDs, in relation to different components, MA^+, Pb^{2+}, or Br^-.[49] When both oleylamine and oleic acid are used as ligands, they react to form oleyl ammonium and oleate. Thus, oleylamine, oleyl ammonium, oleate, and oleic acid are all expected to play some role in passivating the cationic and anion defects, as observed in PQDs.[24] It is expected that these ligands passivate with similar molar amounts, as observed in the mass spectrum of $CsPbI_3$ PQDs.[58] However, Liu *et al*. showed that MSCs formation occurs with an increase in amine concentration, and the mass spectrum presented herein, along with control experiments (not shown), shows MSCs are predominantly capped using oleylamine in its deprotonated form. Thus, the surface seems cation rich, with likely methylammonium and lead defects dominating over halide anions. There are likely a small percentage of Br^- defects on the surface that are passivated by oleyl ammonium. Li *et al*. proposed that amines could act as a stronger capping ligand,[5] and long chain primary amines provide excellent surface coverage, leading to more effective passivation and smaller particle size.[59] This suggests a correlation between smaller particles and cationic surface environments.

Figure 3-7B illustrates the tuning effects of temperature and capping ligand concentration on MSCs and PQDs. In this work, we see the equilibrium shift to MSCs from PQDs by increasing the capping ligand concentration and the temperature of the precursor solution. Using excessive capping ligand usually leads to better passivation and reduced particle size.[4,5] Capping ligands help lower the surface free energy and stabilize particles at a smaller critical radius.[33,42,43] Meanwhile, increasing the temperature helps to overcome the energy barriers for formation and results in the stabilization of smaller particles.[33,42,43] It also facilitates the formation of nucleation sites and increases the solubility of capping ligands, both of which favor smaller particles.[60] Moreover, the nanocrystals also undergo rapid cooling during formation, which inhibits Ostwald ripening, similarly lowering the critical radius.[33] Both of these variables used in conjunction not only allow for the tuning between MSCs and PQDs, but also for varying the size of MSCs.

As quantum size confinement affects both MSCs and PQDs, tuning their size has significant implications on their bandgaps (Figure 3-7C). [61] While the tunability of PQDs has been well established[1,62–70], the tunability of MSCs is less explored since they are often described as discrete.[45,71] In this work, MSCs show a tunable emission from 436 nm to 453 nm. This emission band shift may also be due to a change in band edge defect states (Figure 3-7C). In addition to the size difference, there is also an increase in the magnitude of the Stokes shift when switching from smaller particles, like MSC LARP and MSC60B, to larger particles, MSC70A.[35] MSC70A were formed using a 50°C temperature differential from rapid cooling. Rapid cooling results in smaller particles and causes crystal formation to occur on a shorter timescale. This can also lead to more defects often responsible for trap state emission.[34] Thus, the kinetic barrier is overcome, but there is no time to reach thermodynamic equilibrium. By increasing the temperature in conjunction with increasing capping ligand concentration, MSCs exhibit tunable emission bands through both potential defect introduction and size variability.

3.5 Conclusion

Methylammonium lead bromide magic-sized clusters and quantum dots are synthesized using a new heated ligand assisted reprecipitation technique using organic amines and acids as capping ligands. UV-vis and PL spectroscopy were used to confirm the changes between PQDs and MSCs by varying the temperature of the precursor solution while keeping the antisolvent temperature consistent, without the need to use an excessive concentration of capping ligand. It was found that higher precursor solution temperatures favor MSCs, while lower temperatures favor PQDs. Moreover, increasing the temperature of the system allows MSCs' emission band to be tuned from 436 nm to 453 nm along with increased Stokes shift from 13 nm to 23 nm through the introduction of surface defects. Low frequency Raman results agree with that of bulk $MAPbBr_3$, suggesting that the core of the MSCs has a very similar crystal or unit cell structure as bulk, which is interesting given their small size that one may expect higher vibrational frequencies than bulk. Since the HLARP synthesis utilizes less capping ligand, IR spectroscopy and mass spectrometry could be used to determine that amine was the primary capping ligand bound on the surface of the MSCs. This indicates that the surface of the MSCs is cation rich.

3.6 References

(1) Wang, H.-C.; Bao, Z.; Tsai, H.-Y.; Tang, A.-C.; Liu, R.-S. Perovskite Quantum Dots and Their Application in Light-Emitting Diodes. *Small* **2018**, *14* (1), 1702433. https://doi.org/10.1002/smll.201702433.

(2) *Non-injection gram-scale synthesis of cesium lead halide perovskite quantum dots with controllable size and composition | SpringerLink.* https://link.springer.com/article/10.1007/s12274-016-1090-1 (accessed 2022-03-23).

(3) Leng, J.; Wang, T.; Zhao, X.; Ong, E. W. Y.; Zhu, B.; Ng, J. D. A.; Wong, Y.-C.; Khoo, K. H.; Tamada, K.; Tan, Z.-K. Thermodynamic Control in the Synthesis of Quantum-Confined Blue-Emitting $CsPbBr_3$ Perovskite Nanostrips. *J. Phys. Chem. Lett.* **2020**, *11* (6), 2036–2043. https://doi.org/10.1021/acs.jpclett.9b03873.

(4) Xu, K.; Allen, A. C.; Luo, B.; Vickers, E. T.; Wang, Q.; Hollingsworth, W. R.; Ayzner, A. L.; Li, X.; Zhang, J. Z. Tuning from Quantum Dots to Magic Sized Clusters of $CsPbBr_3$ Using Novel Planar Ligands Based on the Trivalent Nitrate Coordination Complex. *J. Phys. Chem. Lett.* **2019**, *10* (15), 4409–4416. https://doi.org/10.1021/acs.jpclett.9b01738.

(5) Liu, L.; Xu, K.; Vickers, E. T.; Allen, A. C.; Li, X.; Peng, L.; Zhang, J. *Varying the Concentration of Organic Acid and Amine Ligands Allows Tuning between Quantum Dots and Magic-Sized Clusters of $CH_3NH_3PbBr_3$ Perovskite:*

Implications for Photonics and Energy Conversion | ACS Applied Nano Materials. https://pubs.acs.org/doi/abs/10.1021/acsanm.0c02894 (accessed 2021-04-13).

(6) Lou, Y.; Fang, M.; Chen, J.; Zhao, Y. Formation of Highly Luminescent Cesium Bismuth Halide Perovskite Quantum Dots Tuned by Anion Exchange. *Chem. Commun.* **2018**, *54* (30), 3779–3782. https://doi.org/10.1039/C8CC01110A.

(7) Wang, H.; Sui, N.; Bai, X.; Zhang, Y.; Rice, Q.; Seo, F. J.; Zhang, Q.; Colvin, V. L.; Yu, W. W. Emission Recovery and Stability Enhancement of Inorganic Perovskite Quantum Dots. *J. Phys. Chem. Lett.* **2018**, *9* (15), 4166–4173. https://doi.org/10.1021/acs.jpclett.8b01752.

(8) Wei, Y.; Cheng, Z.; Lin, J. An Overview on Enhancing the Stability of Lead Halide Perovskite Quantum Dots and Their Applications in Phosphor-Converted LEDs. *Chemical Society Reviews* **2019**, *48* (1), 310–350. https://doi.org/10.1039/C8CS00740C.

(9) Wang, S.; Wang, Y.; Zhang, Y.; Zhang, X.; Shen, X.; Zhuang, X.; Lu, P.; Yu, W. W.; Kershaw, S. V.; Rogach, A. L. Cesium Lead Chloride/Bromide Perovskite Quantum Dots with Strong Blue Emission Realized via a Nitrate-Induced Selective Surface Defect Elimination Process. *J. Phys. Chem. Lett.* **2019**, *10* (1), 90–96. https://doi.org/10.1021/acs.jpclett.8b03750.

(10) Bi, C.; Kershaw, S. V.; Rogach, A. L.; Tian, J. Improved Stability and Photodetector Performance of $CsPbI_3$ Perovskite Quantum Dots by Ligand Exchange with Aminoethanethiol. *Advanced Functional Materials* **2019**, *29* (29), 1902446. https://doi.org/10.1002/adfm.201902446.

(11) Zhang, Z.-X.; Li, C.; Lu, Y.; Tong, X.-W.; Liang, F.-X.; Zhao, X.-Y.; Wu, D.; Xie, C.; Luo, L.-B. Sensitive Deep Ultraviolet Photodetector and Image Sensor Composed of Inorganic Lead-Free Cs3Cu2I5 Perovskite with Wide Bandgap. *J. Phys. Chem. Lett.* **2019**, *10* (18), 5343–5350. https://doi.org/10.1021/acs.jpclett.9b02390.

(12) Lu, L.-Q.; Tan, T.; Tian, X.-K.; Li, Y.; Deng, P. Visual and Sensitive Fluorescent Sensing for Ultratrace Mercury Ions by Perovskite Quantum Dots. *Analytica Chimica Acta* **2017**, *986*, 109–114. https://doi.org/10.1016/j.aca.2017.07.014.

(13) Wang, Y.; Zhu, Y.; Huang, J.; Cai, J.; Zhu, J.; Yang, X.; Shen, J.; Jiang, H.; Li, C. CsPbBr3 Perovskite Quantum Dots-Based Monolithic Electrospun Fiber Membrane as an Ultrastable and Ultrasensitive Fluorescent Sensor in Aqueous Medium. *J. Phys. Chem. Lett.* **2016**, *7* (21), 4253–4258. https://doi.org/10.1021/acs.jpclett.6b02045.

(14) *Precise Control of Quantum Confinement in Cesium Lead Halide Perovskite Quantum Dots via Thermodynamic Equilibrium | Nano Letters*. https://pubs.acs.org/doi/abs/10.1021/acs.nanolett.8b00861?casa_token=csmbeRgCtKQAAAAA:hTz_702eAEatMYdwszjn9BFr6SuwZfVlTLgZKH8YBT3zEkRWbnNpK7o7cFUSmBv49zID-1dARsKEHsA (accessed 2022-03-23).

(15) Tyagi, P.; Arveson, S. M.; Tisdale, W. A. Colloidal Organohalide Perovskite Nanoplatelets Exhibiting Quantum Confinement. *J. Phys. Chem. Lett.* **2015**, *6* (10), 1911–1916. https://doi.org/10.1021/acs.jpclett.5b00664.

(16) Stein, J. L.; Steimle, M. I.; Terban, M. W.; Petrone, A.; Billinge, S. J. L.; Li, X.; Cossairt, B. M. Cation Exchange Induced Transformation of InP Magic-Sized Clusters. *Chem. Mater.* **2017**, *29* (18), 7984–7992. https://doi.org/10.1021/acs.chemmater.7b03075.

(17) Xu, K.; Vickers, E. T.; Luo, B.; Allen, A. C.; Chen, E.; Roseman, G.; Wang, Q.; Kliger, D. S.; Millhauser, G. L.; Yang, W.; Li, X.; Zhang, J. Z. First Synthesis of Mn-Doped Cesium Lead Bromide Perovskite Magic Sized Clusters at Room Temperature. *J. Phys. Chem. Lett.* **2020**, *11* (3), 1162–1169. https://doi.org/10.1021/acs.jpclett.9b03700.

(18) Impact of Molecular Ligands in the Synthesis and Transformation between Metal Halide Perovskite Quantum Dots and Magic Sized Clusters - Acsphyschemau (1).Pdf.

(19) Vickers, E. T.; Chen, Z.; Cherrette, V.; Smart, T.; Zhang, P.; Ping, Y.; Zhang, J. Z. Interplay between Perovskite Magic-Sized Clusters and Amino Lead Halide Molecular Clusters. *Research (Wash D C)* **2021**, *2021*. https://doi.org/10.34133/2021/6047971.

(20) White, S. L.; Banerjee, P.; Chakraborty, I.; Jain, P. K. *Ion Exchange Transformation of Magic-Sized Clusters*. ACS Publications. https://pubs.acs.org/doi/full/10.1021/acs.chemmater.6b03882 (accessed 2022-02-17). https://doi.org/10.1021/acs.chemmater.6b03882.

(21) Vickers, E. T.; Xu, K.; Dreskin, B. W.; Graham, T. A.; Li, X.; Zhang, J. Z. Ligand Dependent Growth and Optical Properties of Hybrid Organo-Metal Halide

Perovskite Magic Sized Clusters. *J. Phys. Chem. C* **2019**, *123* (30), 18746–18752. https://doi.org/10.1021/acs.jpcc.9b05521.

(22) Jiang, Z.-J.; Kelley, D. F. Role of Magic-Sized Clusters in the Synthesis of CdSe Nanorods. *ACS Nano* **2010**, *4* (3), 1561–1572. https://doi.org/10.1021/nn100076f.

(23) R. Nevers, D.; B. Williamson, C.; Hanrath, T.; D. Robinson, R. Surface Chemistry of Cadmium Sulfide Magic-Sized Clusters: A Window into Ligand-Nanoparticle Interactions. *Chemical Communications* **2017**, *53* (19), 2866–2869. https://doi.org/10.1039/C6CC09549F.

(24) Zhang, J. Z. A "Cocktail" Approach to Effective Surface Passivation of Multiple Surface Defects of Metal Halide Perovskites Using a Combination of Ligands. *J. Phys. Chem. Lett.* **2019**, *10* (17), 5055–5063. https://doi.org/10.1021/acs.jpclett.9b01166.

(25) Xu, K.; Allen, A. C.; Luo, B.; Vickers, E. T.; Wang, Q.; Hollingsworth, W. R.; Ayzner, A. L.; Li, X.; Zhang, J. Z. Tuning from Quantum Dots to Magic Sized Clusters of CsPbBr3 Using Novel Planar Ligands Based on the Trivalent Nitrate Coordination Complex. *J. Phys. Chem. Lett.* **2019**, *10* (15), 4409–4416. https://doi.org/10.1021/acs.jpclett.9b01738.

(26) Xu, K.; Vickers, E. T.; Luo, B.; Wang, Q.; Allen, A. C.; Wang, H.; Cherrette, V.; Li, X.; Zhang, J. Z. Room Temperature Synthesis of Cesium Lead Bromide Perovskite Magic Sized Clusters with Controlled Ratio of Carboxylic Acid and

Benzylamine Capping Ligands. *Solar Energy Materials and Solar Cells* **2020**, *208*, 110341. https://doi.org/10.1016/j.solmat.2019.110341.

(27) Zhang, L.-J.; Shen, X.-C.; Liang, H.; Yao, J.-T. Multiple Families of Magic-Sized ZnSe Quantum Dots via Noninjection One-Pot and Hot-Injection Synthesis. *J. Phys. Chem. C* **2010**, *114* (50), 21921–21927. https://doi.org/10.1021/jp1044282.

(28) *Physicochemical Evaluation of the Hot‐Injection Method, a Synthesis Route for Monodisperse Nanocrystals - de Mello Donegá - 2005 - Small - Wiley Online Library*. https://onlinelibrary.wiley.com/doi/full/10.1002/smll.200500239?casa_token=lE-u7wT4WFgAAAAA%3Ae-QuUUPvaFzxMxtSrnmkxl75Q6uTKof9F0RL9C0cmrBgHZ11EtCb91vrxJfq8bwQ-EqHOMZaOGv6IQ0 (accessed 2022-03-23).

(29) Kamat, P. V. Quantum Dot Solar Cells. The Next Big Thing in Photovoltaics. *J. Phys. Chem. Lett.* **2013**, *4* (6), 908–918. https://doi.org/10.1021/jz400052e.

(30) Permatasari, F. A.; Masitoh, H. E.; Mahen, E. C. S.; Nuryadin, B. W.; Aimon, A. H.; Syah, Y. M.; Iskandar, F. Synergetic Effect of the Surface Ligand and SiO2 Driven Photoluminescence Stabilization of the CH3NH3PbBr3 Perovskite Magic-Sized Clusters. *Sci Rep* **2021**, *11* (1), 22211. https://doi.org/10.1038/s41598-021-01560-4.

(31) Pu, Y.-C.; Song, F.; Zhang, W.; Lindley, S.; Adams, S.; Zhang, J. Z. Size-Tunable Synthesis of Hollow Gold Nanospheres through Control of Reaction

Temperature. *Particle & Particle Systems Characterization* **2017**, *34* (8), 1600255. https://doi.org/10.1002/ppsc.201600255.

(32) *Cooling Rate and Crystal Size | Seth Stein.* https://sites.northwestern.edu/sethstein/a-small-is-beautiful-approach-to-upgrading-a-beginning-geophysics-course/cooling-rate-and-crystal-size/ (accessed 2022-03-23).

(33) Madras, G.; McCoy, B. J. Temperature Effects on the Transition from Nucleation and Growth to Ostwald Ripening. *Chemical Engineering Science* **2004**, *59* (13), 2753–2765. https://doi.org/10.1016/j.ces.2004.03.022.

(34) Zhou, Y.; Sun, X.; Zhong, K.; Evans, D. G.; Lin, Y.; Duan, X. Control of Surface Defects and Agglomeration Mechanism of Layered Double Hydroxide Nanoparticles. *Ind. Eng. Chem. Res.* **2012**, *51* (11), 4215–4221. https://doi.org/10.1021/ie202302n.

(35) Tan, A. M. Z.; Garcia, M. A.; Hennig, R. G. Giant Stokes Shift for Charged Vacancies in Monolayer SnS. *Phys. Rev. Materials* **2022**, *6* (4), 044003. https://doi.org/10.1103/PhysRevMaterials.6.044003.

(36) *Uniform, Scalable, High-Temperature Microwave Shock for Nanoparticle Synthesis through Defect Engineering - ScienceDirect.* https://www.sciencedirect.com/science/article/pii/S2590238519300475 (accessed 2022-05-12).

(37) Vickers, E. T.; Enlow, E. E.; Delmas, W. G.; DiBenedetto, A. C.; Chowdhury, A. H.; Bahrami, B.; Dreskin, B. W.; Graham, T. A.; Hernandez, I. N.; Carter, S. A.; Ghosh, S.; Qiao, Q.; Zhang, J. Z. Enhancing Charge Carrier Delocalization in

Perovskite Quantum Dot Solids with Energetically Aligned Conjugated Capping Ligands. *ACS Energy Lett.* **2020**, *5* (3), 817–825. https://doi.org/10.1021/acsenergylett.0c00093.

(38) Xu, K.; Vickers, E. T.; Rao, L.; Lindley, S. A.; Allen, A. C.; Luo, B.; Li, X.; Zhang, J. Z. Synergistic Surface Passivation of CH3NH3PbBr3 Perovskite Quantum Dots with Phosphonic Acid and (3-Aminopropyl)Triethoxysilane. *Chemistry – A European Journal* **2019**, *25* (19), 5014–5021. https://doi.org/10.1002/chem.201805656.

(39) Vickers, E. T.; Xu, K.; Dreskin, B. W.; Graham, T. A.; Li, X.; Zhang, J. Z. Ligand Dependent Growth and Optical Properties of Hybrid Organo-Metal Halide Perovskite Magic Sized Clusters. *J. Phys. Chem. C* **2019**, *123* (30), 18746–18752. https://doi.org/10.1021/acs.jpcc.9b05521.

(40) Thanh, N. T. K.; Maclean, N.; Mahiddine, S. Mechanisms of Nucleation and Growth of Nanoparticles in Solution. *Chem. Rev.* **2014**, *114* (15), 7610–7630. https://doi.org/10.1021/cr400544s.

(41) Stefanescu, D. M. Equilibrium and Non-Equilibrium during Solidification. In *Science and Engineering of Casting Solidification, Second Edition*; Springer US: Boston, MA, 2009; pp 1–20. https://doi.org/10.1007/978-0-387-74612-8_2.

(42) Shen, Y.; Chen, R.; Yu, X.; Wang, Q.; Jungjohann, K. L.; Dayeh, S. A.; Wu, T. Gibbs–Thomson Effect in Planar Nanowires: Orientation and Doping Modulated Growth. *Nano Lett.* **2016**, *16* (7), 4158–4165. https://doi.org/10.1021/acs.nanolett.6b01037.

(43) Scalfi, L.; Coasne, B.; Rotenberg, B. On the Gibbs–Thomson Equation for the Crystallization of Confined Fluids. *J. Chem. Phys.* **2021**, *154* (11), 114711. https://doi.org/10.1063/5.0044330.

(44) Silva, F. O.; Carvalho, M. S.; Mendonça, R.; Macedo, W. A.; Balzuweit, K.; Reiss, P.; Schiavon, M. A. Effect of Surface Ligands on the Optical Properties of Aqueous Soluble CdTe Quantum Dots. *Nanoscale Res Lett* **2012**, *7* (1), 536. https://doi.org/10.1186/1556-276X-7-536.

(45) Pun, A. B.; Mazzotti, S.; Mule, A. S.; Norris, D. J. Understanding Discrete Growth in Semiconductor Nanocrystals: Nanoplatelets and Magic-Sized Clusters. *Acc. Chem. Res.* **2021**, *54* (7), 1545–1554. https://doi.org/10.1021/acs.accounts.0c00859.

(46) Pun, A. B.; Mazzotti, S.; Mule, A. S.; Norris, D. J. Understanding Discrete Growth in Semiconductor Nanocrystals: Nanoplatelets and Magic-Sized Clusters. *Acc. Chem. Res.* **2021**, *54* (7), 1545–1554. https://doi.org/10.1021/acs.accounts.0c00859.

(47) Bawendi, M. G.; Steigerwald, M. L.; Brus, L. E. The Quantum Mechanics of Larger Semiconductor Clusters (“Quantum Dots”). *Annu. Rev. Phys. Chem.* **1990**, *41* (1), 477–496. https://doi.org/10.1146/annurev.pc.41.100190.002401.

(48) Harrell, S. M.; McBride, J. R.; Rosenthal, S. J. Synthesis of Ultrasmall and Magic-Sized CdSe Nanocrystals. *Chem. Mater.* **2013**, *25* (8), 1199–1210. https://doi.org/10.1021/cm303318f.

(49) Enhancing Defect Tolerance with Ligands at the Surface of Lead Halide Perovskites.

(50) Wheeler, D. A.; Zhang, J. Z. Exciton Dynamics in Semiconductor Nanocrystals. *Adv. Mater.* **2013**, *25* (21), 2878–2896. https://doi.org/10.1002/adma.201300362.

(51) Meinardi, F.; Colombo, A.; Velizhanin, K. A.; Simonutti, R.; Lorenzon, M.; Beverina, L.; Viswanatha, R.; Klimov, V. I.; Brovelli, S. Large-Area Luminescent Solar Concentrators Based on 'Stokes-Shift-Engineered' Nanocrystals in a Mass-Polymerized PMMA Matrix. *Nature Photon* **2014**, *8* (5), 392–399. https://doi.org/10.1038/nphoton.2014.54.

(52) Liu, Y.; Kim, D.; Morris, O. P.; Zhitomirsky, D.; Grossman, J. C. Origins of the Stokes Shift in PbS Quantum Dots: Impact of Polydispersity, Ligands, and Defects. *ACS Nano* **2018**, *12* (3), 2838–2845. https://doi.org/10.1021/acsnano.8b00132.

(53) Ushakova, E. V.; Litvin, A. P.; Parfenov, P. S.; Fedorov, A. V.; Artemyev, M.; Prudnikau, A. V.; Rukhlenko, I. D.; Baranov, A. V. Anomalous Size-Dependent Decay of Low-Energy Luminescence from PbS Quantum Dots in Colloidal Solution. *ACS Nano* **2012**, *6* (10), 8913–8921. https://doi.org/10.1021/nn3029106.

(54) Leguy, A. M. A.; Goñi, A. R.; Frost, J. M.; Skelton, J.; Brivio, F.; Rodríguez-Martínez, X.; Weber, O. J.; Pallipurath, A.; Alonso, M. I.; Campoy-Quiles, M.; Weller, M. T.; Nelson, J.; Walsh, A.; Barnes, P. R. F. Dynamic Disorder, Phonon Lifetimes, and the Assignment of Modes to the Vibrational Spectra of

Methylammonium Lead Halide Perovskites. *Phys. Chem. Chem. Phys.* **2016**, *18* (39), 27051–27066. https://doi.org/10.1039/C6CP03474H.

(55) Quarti, C.; Grancini, G.; Mosconi, E.; Bruno, P.; Ball, J. M.; Lee, M. M.; Snaith, H. J.; Petrozza, A.; De Angelis, F. The Raman Spectrum of the $CH_3NH_3PbI_3$ Hybrid Perovskite: Interplay of Theory and Experiment. *J. Phys. Chem. Lett.* **2014**, *5* (2), 279–284. https://doi.org/10.1021/jz402589q.

(56) Perez De Berti, I.; Cagnoli, M.; Pecchi, G.; Alessandrini, J.; Stewart, S.; Bengoa, F.; Marchetti, S. Alternative Low-Cost Approach to the Synthesis of Magnetic Iron Oxide Nanoparticles by Thermal Decomposition of Organic Precursors. *Nanotechnology* **2013**, *24*, 175601. https://doi.org/10.1088/0957-4484/24/17/175601.

(57) Salavati-Niasari, M.; Fereshteh, Z.; Davar, F. Synthesis of Oleylamine Capped Copper Nanocrystals via Thermal Reduction of a New Precursor. *Polyhedron* **2009**, *28* (1), 126–130. https://doi.org/10.1016/j.poly.2008.09.027.

(58) Kim, J.; Cho, S.; Dinic, F.; Choi, J.; Choi, C.; Jeong, S. M.; Lee, J.-S.; Voznyy, O.; Ko, M. J.; Kim, Y. Hydrophobic Stabilizer-Anchored Fully Inorganic Perovskite Quantum Dots Enhance Moisture Resistance and Photovoltaic Performance. *Nano Energy* **2020**, *75*, 104985. https://doi.org/10.1016/j.nanoen.2020.104985.

(59) Green, M. The Nature of Quantum Dot Capping Ligands. *J. Mater. Chem.* **2010**, *20* (28), 5797–5809. https://doi.org/10.1039/C0JM00007H.

(60) Zhang, L.-J.; Shen, X.-C.; Liang, H.; Yao, J.-T. Multiple Families of Magic-Sized ZnSe Quantum Dots via Noninjection One-Pot and Hot-Injection Synthesis. *J. Phys. Chem. C* **2010**, *114* (50), 21921–21927. https://doi.org/10.1021/jp1044282.

(61) Elward, J. M.; Chakraborty, A. Effect of Dot Size on Exciton Binding Energy and Electron–Hole Recombination Probability in CdSe Quantum Dots. *J. Chem. Theory Comput.* **2013**, *9* (10), 4351–4359. https://doi.org/10.1021/ct400485s.

(62) Song, W.-S.; Yang, H. Efficient White-Light-Emitting Diodes Fabricated from Highly Fluorescent Copper Indium Sulfide Core/Shell Quantum Dots. *Chem. Mater.* **2012**, *24* (10), 1961–1967. https://doi.org/10.1021/cm300837z.

(63) Song, W.-S.; Yang, H. Fabrication of White Light-Emitting Diodes Based on Solvothermally Synthesized Copper Indium Sulfide Quantum Dots as Color Converters. *Applied Physics Letters* **2012**, *100* (18), 183104. https://doi.org/10.1063/1.4711019.

(64) Pietryga, J. M.; Park, Y.-S.; Lim, J.; Fidler, A. F.; Bae, W. K.; Brovelli, S.; Klimov, V. I. Spectroscopic and Device Aspects of Nanocrystal Quantum Dots. *Chem. Rev.* **2016**, *116* (18), 10513–10622. https://doi.org/10.1021/acs.chemrev.6b00169.

(65) Zhang, R.; Yang, P.; Wang, Y. Facile Synthesis of CuInS2/ZnS Quantum Dots with Highly near-Infrared Photoluminescence via Phosphor-Free Process. *J Nanopart Res* **2013**, *15* (9), 1910. https://doi.org/10.1007/s11051-013-1910-0.

(66) Moreels, I.; Justo, Y.; De Geyter, B.; Haustraete, K.; Martins, J. C.; Hens, Z. Size-Tunable, Bright, and Stable PbS Quantum Dots: A Surface Chemistry Study. *ACS nano* **2011**, *5* (3), 2004–2012.

(67) Song, W.-S.; Yang, H. Efficient White-Light-Emitting Diodes Fabricated from Highly Fluorescent Copper Indium Sulfide Core/Shell Quantum Dots. *Chem. Mater.* **2012**, *24* (10), 1961–1967. https://doi.org/10.1021/cm300837z.

(68) Protesescu, L.; Yakunin, S.; Bodnarchuk, M. I.; Krieg, F.; Caputo, R.; Hendon, C. H.; Yang, R. X.; Walsh, A.; Kovalenko, M. V. Nanocrystals of Cesium Lead Halide Perovskites ($CsPbX_3$, X = Cl, Br, and I): Novel Optoelectronic Materials Showing Bright Emission with Wide Color Gamut. *Nano Lett.* **2015**, *15* (6), 3692–3696. https://doi.org/10.1021/nl5048779.

(69) Liu, X.; Jiang, Y.; Lan, X.; Li, S.; Wu, D.; Han, T.; Zhong, H.; Zhang, Z. Synthesis of High Quality and Stability CdS Quantum Dots with Overlapped Nucleation-Growth Process in Large Scale. *Journal of Colloid and Interface Science* **2011**, *354* (1), 15–22. https://doi.org/10.1016/j.jcis.2010.10.013.

(70) Stein, J. L.; Mader, E. A.; Cossairt, B. M. Luminescent InP Quantum Dots with Tunable Emission by Post-Synthetic Modification with Lewis Acids. *J. Phys. Chem. Lett.* **2016**, *7* (7), 1315–1320. https://doi.org/10.1021/acs.jpclett.6b00177.

(71) Mule, A. S.; Mazzotti, S.; Rossinelli, A. A.; Aellen, M.; Prins, P. T.; van der Bok, J. C.; Solari, S. F.; Glauser, Y. M.; Kumar, P. V.; Riedinger, A.; Norris, D. J. Unraveling the Growth Mechanism of Magic-Sized Semiconductor Nanocrystals. *J. Am. Chem. Soc.* **2021**, *143* (4), 2037–2048. https://doi.org/10.1021/jacs.0c12185.

Chapter Four

4 Structural Study of Paraffin-stabilized Methylammonium Lead Bromide Magic-Sized Clusters: Implications in Photonics

4.1 Abstract

Metal halide perovskites, such as methylammonium lead bromide, have recently attracted considerable attention due to their interesting and useful photoelectric properties. Here, two types of methylammonium lead bromide magic-sized clusters (MSCs), passivated with oleylamine and oleic acid, were synthesized using ligand assisted reprecipitation (LARP) and heated LARP (HLARP) methods. The optical properties of these MSCs were characterized using UV-Vis electronic absorption and photoluminescence (PL) spectroscopy. The HLARP synthesis resulted in an increase in the PL quantum yield of the MSCs by two-fold to 76%. The stability of the MSCs was tested using time-dependent PL spectroscopy. LARP MSCs in solution degraded completely after 14 days under ambient conditions, while HLARP MSCs lasted for 26 days. To stabilize them, the MSCs were added to a non-coordinating matrix, paraffin. Both MSCs showed significantly improved resistance to water with the addition of paraffin. Solid LARP MSCs lost all luminescence with and without the addition of paraffin by about three hours. Solid HLARP MSCs without paraffin started to aggregate after three hours, but paraffin stabilized HLARP MSC films were stable for eight days. This improved stability in solid state form allowed for analysis

using Raman spectroscopy, X-ray diffraction (XRD), and transmission electron microscopy (TEM). Raman spectroscopy revealed that the HLARP MSCs show an additional peak at 147 cm^{-1} compared to LARP MSCs, which is attributed to methylammonium. XRD and TEM confirm that MSCs have a quasi-crystalline orthorhombic structure. The significantly extended stability of the solid HLARP MSCs with paraffin has important implications for potential device applications.

4.2 Introduction

Perovskite quantum dots (PQDs) have been studied extensively for their tunable optical properties and high photoluminescence (PL) quantum yield.[1] Their emission window can be broadly tuned by controlling the crystal size,[2–5] capping ligand,[6,7] and elemental composition.[8,9] These fascinating optoelectronic properties make them promising substrates for applications in photovoltaics for light emitting devices,[10–12] photodetectors,[13–15] and sensing.[16–18] PQDs are characterized by their tunability, which stems from their high surface-to-volume (S/V) ratio and quantum confinement.[19,20] Perovskite magic-sized clusters (MSCs) share many of these characteristics with PQDs but are smaller with higher monodispersity and narrower, bluer optical absorption and emission bands. [6,21–25] They are often described as discrete,[26] meta-stable intermediaries of PQDs.[27] While MSCs can be formed in a variety of ways using a variety of temperature ranges and environments, LARP is typically used for its simplicity.[28] HLARP introduces temperature variability but remains straightforward without the need for an air-free environment. Moreover, it allows the size of the nanocrystals to be tuned.[29] MSCs can be used to understand the relationship between PQDs and MSCs and provide insight into the growth mechanism of PQDs and bulk perovskite. They also present themselves as a potential substrate for blue-light emitting devices.

As MSCs have a high S/V ratio, they are susceptible to instability due to surface dangling bonds or defect sites.[30–32] Thus, MSCs are typically formed using an excess concentration of capping ligand using the LARP method.[6,7,24] However, a newer synthesis utilized 15% of the capping ligand with the heated ligand assisted reprecipitation (HLARP) method, resulting in a slightly larger particle size and more red-shifted emission.[29] Little is known about the differences between the properties of these MSCs other than their size. The change to the synthetic procedure, however, has potential stability benefits, as excess oleylamine has been shown to play a role in the moisture-driven structural degradation mechanism of PQDs.[33] Oleylamine reacts with water, forming a reactive hydroxide salt that strips the 3D perovskite structure by layers, eventually forming non-emissive lead bromide.[33]

Perovskite can also degrade with light, oxygen, or water, creating a huge barrier for solid characterization and thin film device applications.[34–40] Light and oxygen react in tandem to form free radicals that deprotonate the methylammonium cation.[41,42] Additionally, water has been shown to penetrate the perovskite structure, forming hydrate perovskite structures, and weakening the bond between the cation and lead bromide, causing degradation of the perovskite structure.[43,44] Thus, preventing the interaction of perovskite nanocrystals with light, oxygen, and water is paramount to increasing their stability.

In addition to externally driven degradation, there are various obstacles that impede the ability of perovskite MSCs to be characterized as a solid. For instance, drying effects and aggregation can make powder XRD (PXRD) measurements difficult or inaccurate[7] and TEM is often deemed inadequate due to weak contrast, poor resolution, and high beam sensitivity.[45] Therefore, little is known about their solid structure and there is an impetus to stabilize these MSCs to glean more accurate measurements. The hydrophobic nature of paraffin has been shown to increase shelf life by creating a non-reactive hydrophobic barrier to prevent aggregation,[46,47] while the hermetic nature of paraffin seals the material from the effects of oxygen.[48]

In this work, LARP and HLARP MSCs were characterized using UV-Vis electronic absorption and photoluminescent spectroscopy. We employ a simple, green and low-cost method to encapsulate MSCs in paraffin, improving their oxygen and water stability, and allowing them to maintain their luminous intensity for longer. The stability of both HLARP and LARP MSCs was compared in solution under ambient conditions with and without paraffin and in the presence of water with and without paraffin. The samples were also dried to make films and compared with and without the presence of paraffin. LARP MSCs degraded rapidly but remained stable enough to obtain Raman data. However, UV-Vis and PL results show that the HLARP MSCs film did not aggregate or degrade for up to eight days, allowing for analysis using both X-ray diffraction and Raman spectroscopy. Moreover, HLARP MSCs proved stable enough to image nonaggregated MSCs for the first time.

4.3 Methods

4.3.1 Materials

Methylammonium bromide (MABr, 99.9%, Greatcell Solar), lead bromide $PbBr_2$ (99.999%, Alfa Aesar), oleic acid (90%, Sigma Aldrich), *n*-oleylamine (98.0%, Tokyo Chemical Industry), *N*,*N*-dimethylformamide (DMF, 99.9%, Fisher Scientific), paraffin wax cake (Fisher Scientific), and toluene (99.9%, Fisher Scientific) were commercially available. All chemicals were used as received without any further purification.

4.3.2 Synthesis of $MAPbBr_3$ MSCs

Two types of MSCs were synthesized using LARP and HLARP syntheses, MABr (0.080 mmol, 9.0 mg), $PbBr_2$ (0.20 mmol, 73.0 mg), and 400 µL of DMF were added to a borosilicate vial, and the solution was sonicated in a water bath at room temperature or between 20°C (LARP) or 70°C (HLARP) until all solid dissolved. Next, 0.15 mmol (HLARP) or 1 mmol (LARP) of oleic acid was added to the solution and sonicated at the same temperature for 30 s. Then, an equimolar amount of oleylamine was added to the solution and sonicated for 30 s at the same temperature. 100 μL of the precursor solution was quickly injected into 5.0 mL of toluene under vigorous stirring. The formation of these MSCs was analyzed over time. To stabilize the MSCs, 12 mg of paraffin was dissolved in 100 μL of as prepared solution. Solid samples were prepared by drop casting the as prepared solution and paraffin mixture onto borosilicate glass slides.

4.3.3 Stability Tests

4.3.3.1 Open Air

The as prepared LARP and HLARP samples were sealed and left under ambient conditions and exposed to light and air. Aliquots of sample were removed and tested using UV-Vis and PL spectroscopes over the course of 14 (LARP) to 26 days (HLARP) until the sample was no longer luminous. For paraffin stabilized samples, 12 mg of paraffin was added to 100 μL of the as prepared solution and tested every week.

4.3.3.2 Water Stability Test

To test water stability, 10 μL of water was added to 5 mL of as prepared LARP and HLARP solutions. These samples were then tested using UV-Vis and PL spectroscopes until they no longer emitted light. For paraffin stabilized samples, the as prepared solution was mixed 600 mg of paraffin and similarly tested.

4.3.3.3 Solid Samples

For solid samples, 50 μL of as prepared sample was drop cast onto borosilicate glass slides. This process was repeated for paraffin stabilized samples, where the as prepared solution was mixed with 600 mg of paraffin. These samples were similarly analyzed using absorption and PL spectroscopies.

4.3.3.4 Spectroscopic Measurements

Ultraviolet-visible (UV–vis) absorption spectra were measured with an Agilent Technologies Cary 60 UV–vis spectrophotometer, and the PL spectra were measured using a Cary Eclipse spectrofluorometer using a quartz 700 μL microcuvette at room temperature and an excitation wavelength of 400 nm. Raman measurements were conducted on a Thermo Fisher DRX3 785 nm laser at a power of 1 mW for 30 seconds and three accumulations using a 100x objective.

4.3.3.5 X-Ray Diffraction

Using the unwashed MSCs stabilized in paraffin, 50 μL were drop cast onto a borosilicate slide and analyzed using a Rigaku American Miniflex Plus powder diffractometer at a voltage of 40 kV and current of 30 mA, with a scanning angle 1.4–32 (2θ) and a rate of 0.05 degrees/ min and a step size of 0.02 degrees over the course of ten hours.

4.3.3.6 Transmission Electron Microscopy

High resolution transmission electron microscopy (HRTEM) and high-angle annular dark field (HAADF) scanning transmission electron microscopy (STEM) were performed at the National Center for Electron Microscopy (NCEM) facility in Molecular Foundry, Lawrence Berkeley National Laboratory on an FEI UT Tecnai microscope, operated at an acceleration voltage of 200 kV. The sample was diluted 225-fold and dropped onto 10 nm thick lacey carbon grids. 10 μL were dropped and blotted twice and allowed to dry for 10 min before being analyzed.

4.4 Results and Discussion

4.4.1 Optical Properties of $MAPbBr_3$

The normalized overlayed absorption and PL spectra were measured for two types of methylammonium lead bromide MSCs synthesized by LARP and HLARP methods.

In the 400-600 nm region, the LARP MSCs show a single absorption band peaked at 423 nm and a single PL band peaked at 436 nm when excited at 400 nm (Figure 1A). The HLARP MSCs exhibit red shifted absorption and PL bands peaked at 432 nm and 450 nm, respectively. This red-shift of both the absorption and PL bands indicates the formation of larger MSCs and is in good agreement with previous reports.[7,29] The PL bands of both samples have a narrow full width at half maximum (FWHM) of 20 nm, indicative of a narrow size distribution.

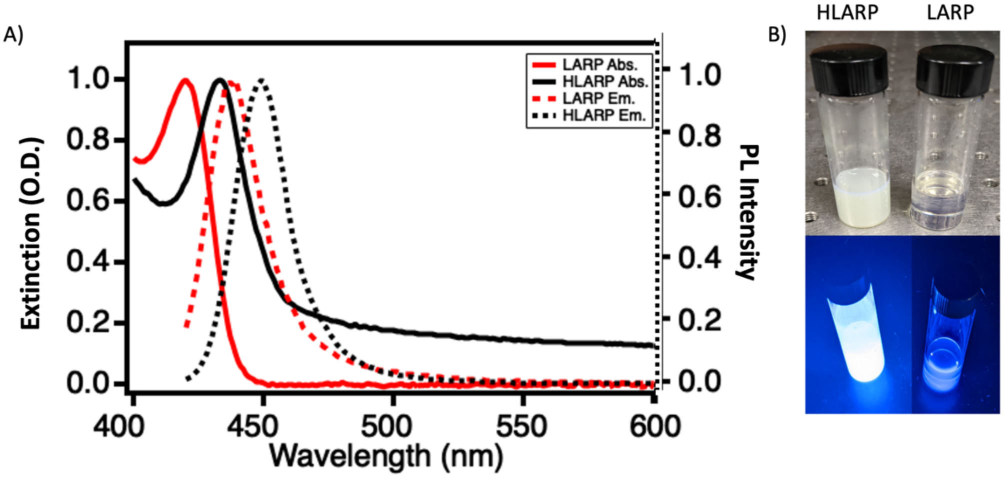

Figure 4-12. A) Normalized UV-Vis Electronic Absorption and PL Spectra for LARP and HLARP Syntheses; B) Images of MSCs made with LARP and HLARP under ambient light and UV light.

HLARP MSCs have a PLQY of 76%, over double that of the LARP MSCs at 36%. This is expected as higher temperature syntheses, such as those in PQD hot injection, often lead to nanoparticles with higher PL quantum yield (QY) (Figure 1B).[49,50] Moreover, HLARP MSCs' absorption band is ten times as intense as LARP

MSCs', showing an increase in concentration and product yield. The increased temperature leads to more collisions, increasing the number of nucleation sites and the rate of the reaction.[29] Thus, the HLARP synthesis produces a more concentrated solution of MSCs with higher PLQYs.

4.4.2 Stability Analysis

The long-term stability of MSCs in solution was monitored until the sample fully degraded and lost luminous intensity (Figure 2). The time-dependent PL spectra of LARP MSCs under ambient conditions indicate that they retain their 436 nm emission without shifting but completely degrade after 14 days (Figure 2A). The time-dependent PL spectra of HLARP MSCs under similar ambient conditions show that the HLARP MSCs have ~20 times the initial PL emission intensity of LARP MSCs but show a different degradation mechanism (Figure 2B). The initial emission band starts at 450 nm and shifts to 456 nm after 24 hours. This indicates that the MSCs are growing slightly due to Ostwald ripening and reaching a larger metastable state.[51–53] The intensity of the solution increases for up to five days, more than doubling in intensity before starting to diminish and degrade. This is likely due to leftover starting reagents in the unwashed solution forming new nucleation sites, and thus new MSCs. The leftover capping ligand in the solution does not appear to be a detriment at this concentration, as HLARP MSCs take 26 days to fully diminish.

Both degradation processes plotted over time show the increased stability of HLARP over LARP MSCs in ambient conditions (Figure 2G).

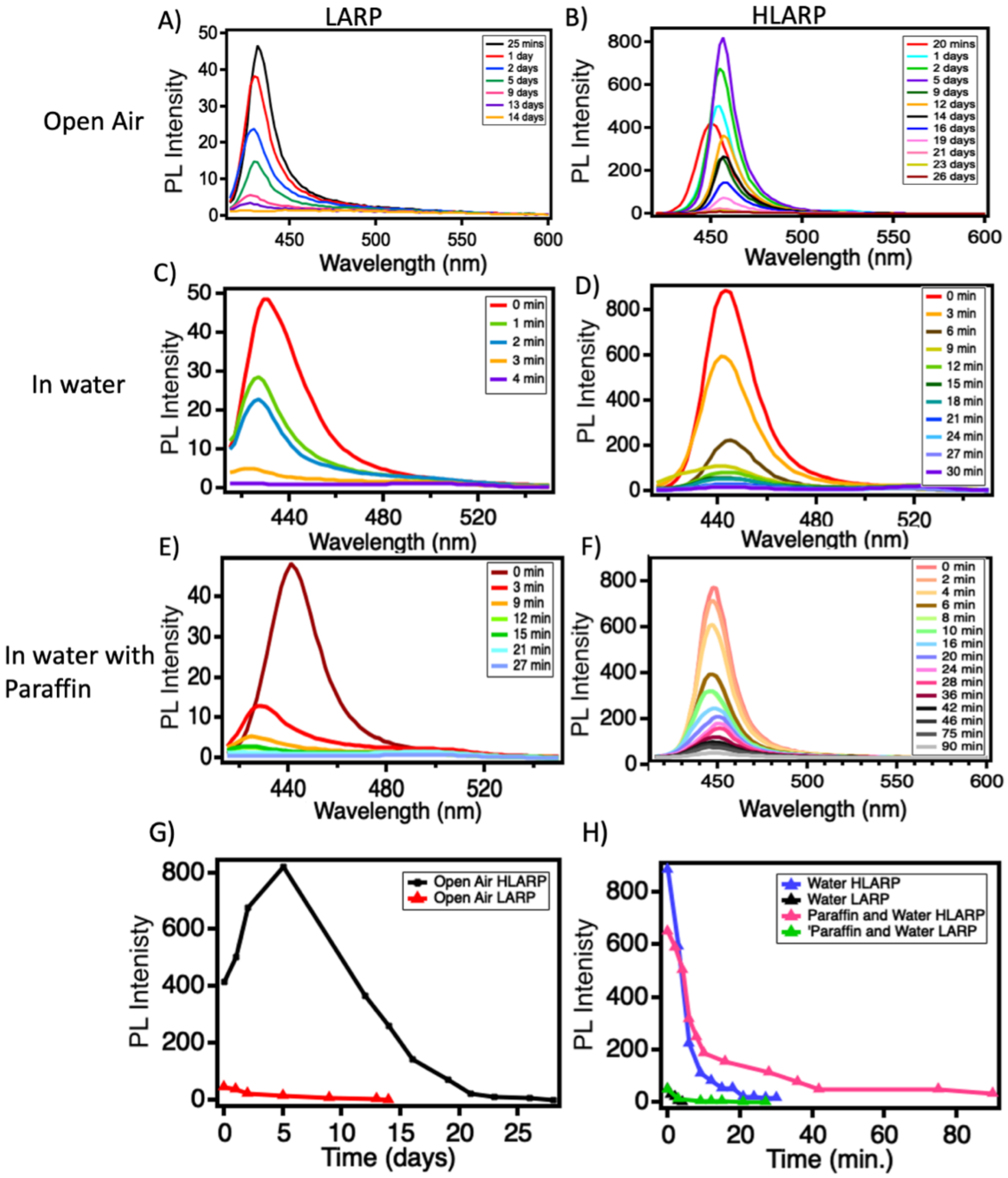

Figure 4-13. Time-dependent PL stability analysis of LARP and HLARP over time: A) LARP MSCs under ambient conditions, exposed to light and air; B) LARP MSCs

after the addition of 10 μL of water; C) LARP MSCs after the stabilization in paraffin and the addition of 10 μL of water; D) HLARP MSCs under ambient conditions, exposed to light and air; E) HLARP MSCs after the addition of 10 μL of water; F) HLARP MSCs after the stabilization in paraffin and the addition of 10 μL of water; G) PL Intensity over time comparing LARP and HLARP MSCs under ambient conditions; H) PL Intensity over time comparing LARP and HLARP MSCs with the addition of water.

MSCs can degrade due to water, light, oxygen, or excess capping ligand.[44] The only difference between the LARP and HLARP MSCs is the size and the amount of capping ligand left over in the solution. In general, larger nanoparticles show increased stability over smaller nanoparticles, at least partially justifying HLARP's improved stability.[53] Additionally, LARP MSCs are synthesized with 667% more capping ligands than the HLARP synthesis. Since oleic acid and oleylamine were used as stabilizing ligands and they readily react with each other, this may result in the reaction of bound and unbound ligands, causing the detachment of bound ligands, and resulting in aggregation of the nanoparticles.[54] Secondly, oleylamine can react with water to form oleyl ammonium salt, which reacts and causes a moisture-induced structural degradation.[33] Therefore, increasing the amount of oleylamine in the solution leaves MSCs more susceptible to water destabilization. By synthesizing HLARP MSCs with less capping ligands, they do not undergo these capping ligand degradations as readily and are less susceptible to the oleylamine moisture-driven degradation, making them more stable under ambient conditions. HLARP MSCs stabilized in paraffin remain stable for at least three months under ambient conditions.

To further test the stability and resilience against humidity, 10 μL of water was injected into the 5.0 mL as-prepared sample. The LARP MSCs with this addition proved to be highly unstable in water, as the time-dependent PL spectra fully diminished in four minutes (Figure 2C). In comparison, the time-dependent PL spectra of HLARP MSCs showed they remained luminous for 30 minutes (Figure 2D). Typically, when water molecules in the air interact with the perovskite crystal, strong hydrogen bonds form with the organic cations, weakening the bond between the cation and the $PbBr_2$, allowing for faster deprotonation of the organic cation, leaving the crystal more susceptible to external stressors.[44,55] Moreover, as stated above, the excess oleylamine can react with water to speed up moisture-driven structural degradation.[33]

To reduce degradation, paraffin was introduced as a non-coordinating solvent and stabilizing matrix.[56] Long-chain hydrophobic polymers have been shown to greatly increase water stability by preventing the interaction between water and the PQDs.[57] Here, we see significant improvements to the stability of MSCs with the addition of paraffin. The time-dependent PL spectra of the LARP MSCs show that the MSCs remained luminous for nearly seven times longer, retaining photoluminescence for 27 minutes (Figure 2E). The time-dependent PL spectra of the paraffin stabilized HLARP MSCs also show an improvement and emitted for over 90 minutes (Figure 2F).

Paraffin has been shown to aid PQDs largely with water degradation and partially with oxygen degradation, acting as a hermetic barrier.[48,55–57] With the addition of water, LARP MSCs shifted from 436 nm to 423 nm before the PL intensity diminished. This indicates that the MSCs are breaking into smaller particles before losing luminescence. In the case of the HLARP MSCs, the longevity of the MSCs is improved by a factor of about three. HLARP MSCs degraded without exhibiting peak shifting and retained their 450 nm emission. The small addition of water significantly increases the degradation of the MSCs. Both LARP and HLARP MSCs retain their PL on the scale of weeks when exposed to light and air, but the addition of water, even in the presence of a stabilizing matrix, degrades them in a matter of minutes. Thus, water degradation appears to be the main cause of structural degradation. The addition of paraffin significantly improved the stability and shelf life of these materials and facilitated their characterization in solution. The comparison of the diminishing PL intensities due to water degradation is shown in Figure 2H.

For applications and structural characterizations, it is important for the MSCs to be stabilized as a solid. However, MSCs degrade in the solid form as particles aggregate or fall apart upon drying due to local supersaturation.[45,58,59] The LARP MSCs were drop cast onto borosilicate glass slides and analyzed after three hours. Their PL spectrum was indistinguishable from the borosilicate background, retaining no luminescence. To stabilize the LARP MSCs, paraffin was added prior to drop casting. Similarly, after three hours, the LARP MSCs lost all luminosity. Excess capping ligands could severely limit the ability of these nanoparticles to stabilize as a solid. Thus, if the smaller sized LARP MSCs are desirable for applications, washing protocols may improve stability.

The PL spectra of HLARP MSCs in solution and their dried counterparts were compared, as shown in Figure 3. The solution PL spectrum has one band peaked at 450 nm, while the dried HLARP MSCs without paraffin have the same band with a peak at 450 nm, but with a new band appearing at 473 nm (Figure 3A), indicative of the formation of larger particles.[29] However, with the addition of paraffin, the MSCs keep the one emission band but shift slightly from 450 nm to 456 nm (Figure 3A). This is the same shift that was seen in the solution after one day, attributed to slightly more stable and larger MSCs after possible Ostwald ripening.[60] The paraffin-stabilized HLARP MSC film was left under ambient conditions and remained stable for eight days (Figure 3B). This is important for their potential device applications and characterization in solid state form.

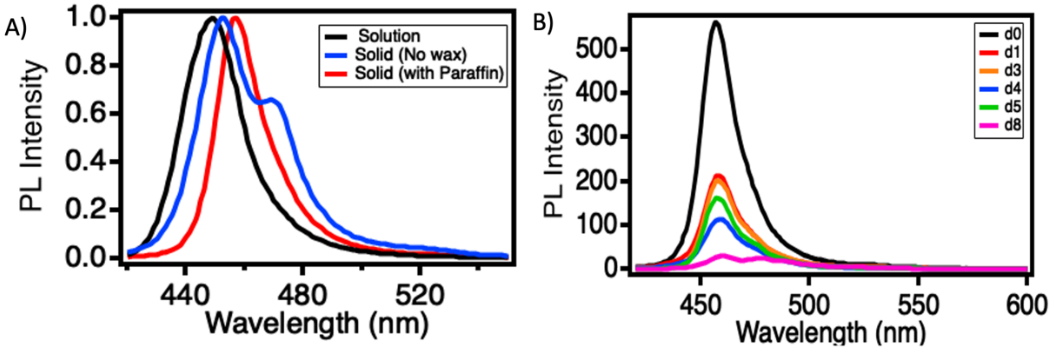

Figure 4-14. Stability of HLARP MSCs as a solid, determined by PL Intensity of A) Normalized spectra of the solution compared to dried HLARP MSCs as prepared and

dried HLARP MSCs stabilized in paraffin after three hours; B) Paraffin stabilized HLARP MSCs over 8 d; C) Images of LARP and HLARP MSCs dried after 3 hours with and without paraffin.

4.4.3 Structural Analysis

The Raman spectra in high frequency and low frequency regions were measured for the solid LARP and HLARP MSCs, immediately upon drying and before aggregation, as shown in Figure 4. In the high frequency region above 700 cm^{-1}, both LARP and HLARP confirm the presence of the primary capping ligand, oleylamine (Figure 4A).[61] All modes in the low frequency region are in good agreement with methylammonium lead bromide bulk perovskite (Figure 4B). The peaks at 107 cm^{-1} and 118 cm^{-1} are indicative of lurching methylammonium, and the broad peak at 240 cm^{-1} due to torsional vibration of methylammonium is present in both LARP and HLARP. However, the 147 cm^{-1} nodding donkey around C is prominent and only shown in the HLARP MSCs.[62] This mode corresponds to a rotational vibration of the cation around the methylammonium carbon. This mode is presumably affected by octahedra tilting, and distortions of the crystal lattice, due to the hydrogen bonding with the halogen and thus provide some measure of the coupling between the molecule and the inorganic framework. The presence of this mode in the HLARP MSCs, and not the LARP MSCs, suggests that the larger MSC is more ordered and that upon the growth of the nanocrystal, the methylammonium becomes more firmly bound in the nanocrystal due to a distortion of the framework.[63]

This distortion could play a role in the improved stability of HLARP MSCs over LARP MSCs.

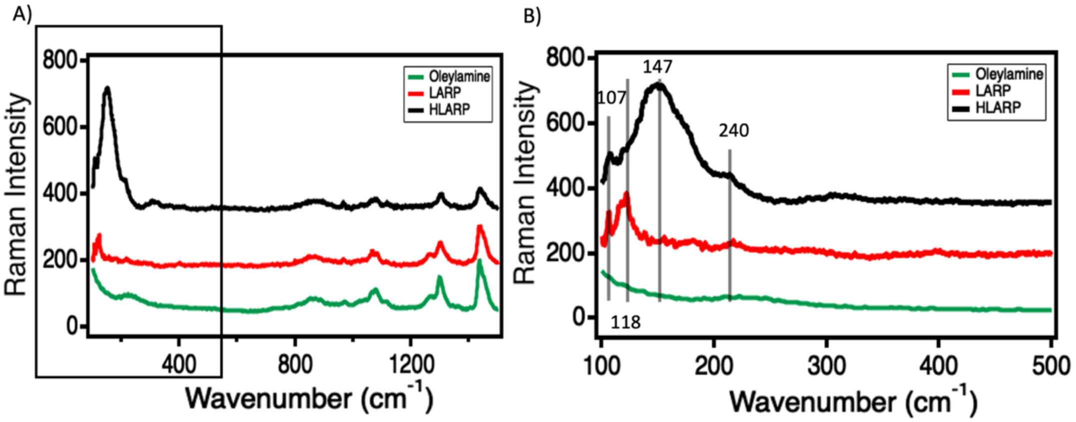

Figure 4-4. Comparison of oleylamine, LARP MSCs, and HLARP MSCs using: A) high and low frequency Raman spectra; B) zoomed in low frequency Raman spectra.

Paraffin stabilization of the HLARP MSCs allowed for PXRD analysis. The XRD patterns of HLARP MSCs are shown in Figure 5. Sharp peaks at ~ 2°, 4°, 6.5°, 21.5° and 23.9° (2θ) due to paraffin are observed. Broad features at 12.4°, 13.8° and 14.9° (2θ) are attributed to HLARP MSCs. The distinct peak at 14.9° correlates well with the expected (020) plane of the orthorhombic $MAPbBr_3$ perovskite. This peak is further confirmed by the higher order amorphous hump (~ 26-31.5° 2θ). Paraffin with oleylamine and oleic acid capping ligands dried in a similar manner produce no features in the 12-15° area of interest. The diffraction data of the HLARP MSCs share common perovskite d-spacings and likely have a distorted perovskite structure. The 14.9° peak is slightly shifted towards a smaller 2θ. This indicated the shift to larger d-spacings from the theoretical 14.95° (5.92 Å) peak of the orthorhombic $MAPbBr_3$.

Moreover, the peak is significantly broader, indicating its smaller size.[64] Organic ligand passivation can cause lattice strain near the surface, which typically relaxes within a few monolayers.[65] However, due to the small size of MSCs, there are likely five (020) lattice planes. Since their size is so small, ligand passivation at the surface strains most of the MSCs' perovskite structure, which would similarly agree with the broad diffraction peaks. Given that LARP MSCs show less order in their low frequency Raman spectra, it is likely that LARP MSCs would show even less crystalline character. This is further supported by their estimated smaller size since larger nanocrystals have more layers to satisfy Bragg's law and produce sharper reflections with increased intensity.[66]

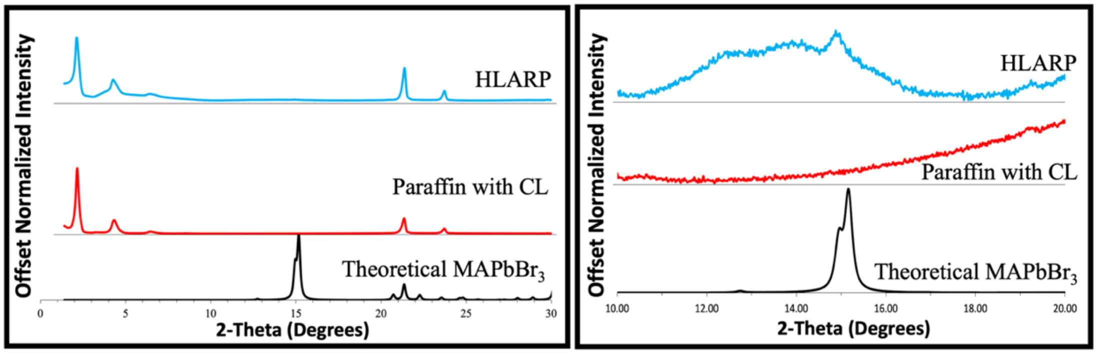

Figure 4-5. X-Ray Diffraction Patterns for HLARP MSCs, Paraffin and Capping Ligand, and Theoretical Spectrum of methylammonium lead bromide (Left) from 0-30° (Right) from 10-20°.

HR-TEM images of HLARP MSCs (Figure 6) indicate the average size was 2.46±0.15 nm by 3.20±0.19, for an average of 2.8 nm, smaller than anticipated with the Brus method.[29] Moreover, the MSCs shown here are around 2 nm smaller than previous reports of TEM images where aggregation was not prevented.[7] These measurements indicate that the MSCs have low crystallinity. The fast Fourier transform (FFT) of the HR-TEM reveals a lattice spacing of ~0.30 nm, which is consistent with the (040) Miller index (Figure 6C). Every two lattice spacings are consistent with the (020) Miller index, a d-spacing of ~0.6 nm, and the 14.9° diffraction peak in the PXRD (Figure 6C). The (040) with a 2θ of ~30° is represented as a very broad and weakly diffracting reflection. Both (020) and (040) miller indices are indicative of the orthorhombic crystal structure.[64,67] The TEM image shows lattice planes perpendicular to the b-axis lattice constant (Figure 6C). The b-axis is approximately 1.5 times longer than a or c axes, which correlates with the shape of the MSCs. The lattice spacing is not present in all the images, likely due to beam sensitivity and particle movement. This makes it hard to characterize the other spacings exactly and also explains the broadness shown in the PXRD pattern. Lattice spacings of around 0.36 nm are also present, which could account for the 12.4° powder peak, but there are very few layers to concretely determine this.

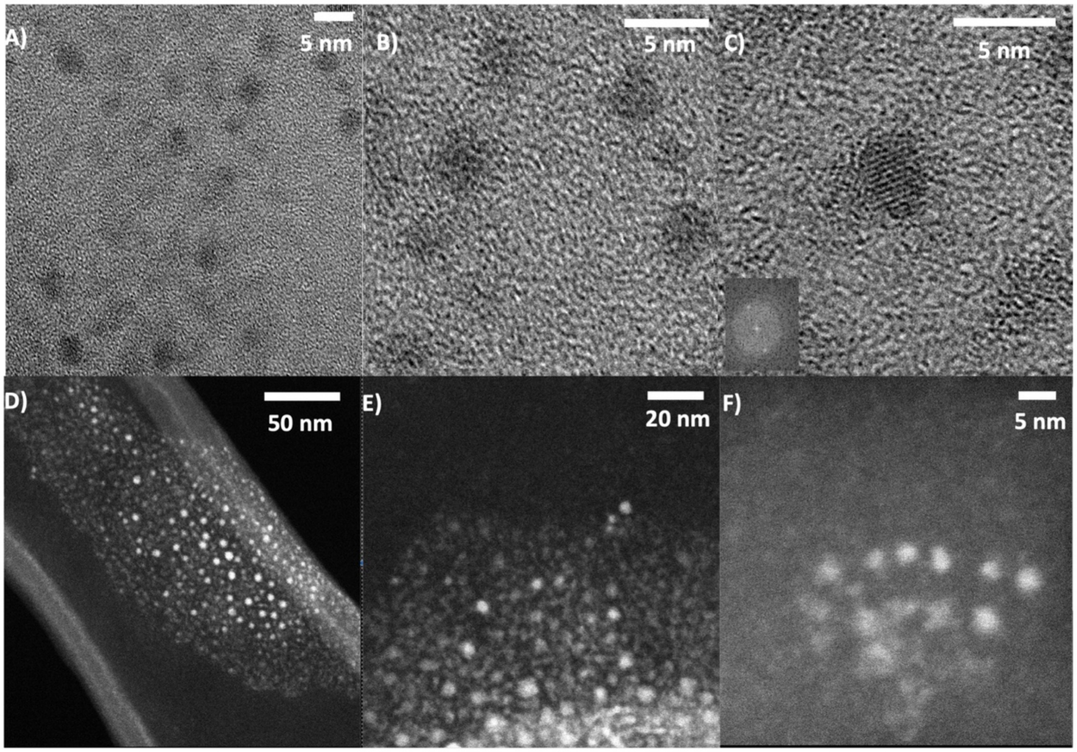

Figure 4-6. Images of HLARP MSCs at various resolutions using: A-C) HR-TEM; D-F) HAADF STEM.

If the concentration is too high, some MSCs aggregate into PQDs. These nanoparticles are ~5 nm in size and show much higher crystallinity by contrast. They show lattice spacing of 0.30 and 0.25 nm, which are in good agreement with the theoretical methylammonium lead bromide powder pattern. Thus, it is possible to structurally distinguish between MSCs and PQDs. MSCs have perovskite characteristics but are quasi-crystalline. PQDs show higher crystallinity, and therefore, are more similar to the perovskite crystal structure.

A potential mechanism of paraffin stabilization and a model of a quasi-crystalline $MAPbBr_3$ LARP and HLARP MSCs can be hypothesized (Figure 7). The

HLARP and LARP MSCs differ in many characteristics. While the HLARP MSCs are slightly harder to make, they possess double the PLQY of the LARP MSCs. The LARP MSCs' decrease in PLQY could be due to an increased number of defects or trap states which give alternative pathways to radiative recombination and can significantly decrease the quantum yield.[8,68–72] This would be contrary to previous hypotheses surrounding the LARP and HLARP MSCs.[29] Additionally, the LARP MSCs were estimated to be around 3.04 nm in size using the Brus model.[29] However, using TEM, it was determined that the larger HLARP MSCs are an average of 2.8 nm in size. Therefore, by modifying the Brus approximation methods, LARP MSCs are likely 2.5 nm in size (Figure 7).[24] This smaller size could lead to their relative instability.[53] In contrast, the HLARP MSCs are formed using a minimal amount of capping ligand at an elevated temperature. This extra step increases the particle size to 2.8 nm, but also doubles the PLQY to 76%. The increase could be due to the higher temperature, providing sufficient energy to allow the MSCs to reach a more stable state. The HLARP MSCs' improved stability allowed them to be characterized with PXRD and TEM. They show lattice spacings of 0.30 nm, which suggests that they are orthorhombic (Figure 7). Contrastingly, the instability of the LARP MSCs hindered their ability to be characterized as a solid.

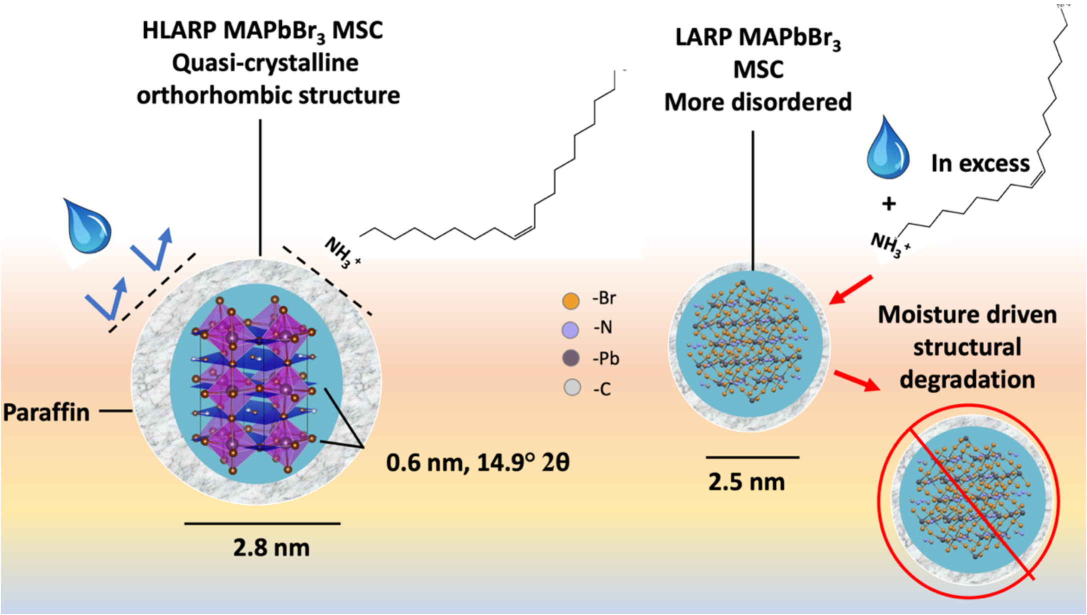

Figure 4-7. Scheme illustration of the differences between LARP and HLARP MSCs and the major effects on their stabilization.

LARP and HLARP MSCs also differ in the capping ligand concentration during synthesis and the order within their structures. LARP MSCs are synthesized with 667% more capping ligands. Excess capping ligands have been shown to play a key role in the degradation of MSCs. There are two potential mechanisms. Since there are both free acid and amine ligands present in the solution, they have the ability to react with ligands bound on the surface of the MSC, leading to aggregation.[54] Furthermore, oleylamine has been shown to react strongly with water and provide a mechanism for moisture-driven structural degradation (Figure 7).[33] This likely contributes to the increased instability of LARP MSCs over HLARP MSCs. Thus, to improve the stability of the LARP synthesis, washing protocols must be optimized.

HLARP MSCs are also more crystalline than LARP MSCs, suggested by the additional Raman mode at 147 cm^{-1}. This indicates an additional bond between the methylammonium and the inorganic framework. Water molecules destabilize perovskite crystal structures by binding to their organic cation and weakening its bond to the crystal structure,[41] the HLARP MSCs are more resilient to water and excess capping ligand degradation, likely due to their increased structural order. Using paraffin as a stabilizing matrix, the HLARP MSCs were stable for eight days as a solid and over three months in solution exposed to light, oxygen, and water. These data suggest that MSCs can be stabilized for future applications in photonics.

4.5 Conclusion

Two types of methylammonium lead bromide MSCs, passivated with oleylamine and oleic acid, were synthesized using LARP and HLARP methods. These MSCs were characterized using UV-Vis electronic absorption and PL spectroscopy. The HLARP synthesis resulted in an increase in the PL quantum yield of the MSCs by two-fold to 76% and showed increased product yield. The stability of the MSCs was tested using time-dependent PL spectroscopy. LARP MSCs in solution degraded completely after 14 days under ambient conditions, while HLARP MSCs lasted for 26 days. To stabilize them, the MSCs were added to paraffin to create a hydrophobic and hermetic barrier and protect them from the degrading effects of water and oxygen. Both paraffin stabilized MSCs showed increased resilience to the addition of water. Solid LARP MSCs lost all luminescence with and without the addition of paraffin by about three hours. Solid HLARP MSCs without paraffin started to aggregate after three hours, but paraffin stabilized HLARP MSC films were stable for eight days. This improved stability in solid state form allowed for analysis using Raman spectroscopy, PXRD, and TEM. Raman spectroscopy revealed that the HLARP MSCs show an additional peak at 147 cm^{-1} compared to LARP MSCs, which is attributed to methylammonium, indicates a more highly ordered structure, and may have implications in HLARP's increased stability. PXRD and TEM confirm that MSCs have a quasi-crystalline orthorhombic structure. The significantly extended stability of the solid HLARP MSCs with paraffin shows promise for future use in photonics.

4.6 References

(1) Wang, H.-C.; Bao, Z.; Tsai, H.-Y.; Tang, A.-C.; Liu, R.-S. Perovskite Quantum Dots and Their Application in Light-Emitting Diodes. *Small* **2018**, *14* (1), 1702433. https://doi.org/10.1002/smll.201702433.

(2) Chen Xu; Lucheng, Peng; Huang, Keke; Shi, Zhan; Xie, Renguo; Yang, Wengsheng. *Non-injection gram-scale synthesis of cesium lead halide perovskite quantum dots with controllable size and composition | SpringerLink.* https://link.springer.com/article/10.1007/s12274-016-1090-1 (accessed 2022-03-23).

(3) Leng, J.; Wang, T.; Zhao, X.; Ong, E. W. Y.; Zhu, B.; Ng, J. D. A.; Wong, Y.-C.; Khoo, K. H.; Tamada, K.; Tan, Z.-K. Thermodynamic Control in the Synthesis of Quantum-Confined Blue-Emitting CsPbBr3 Perovskite Nanostrips. *J. Phys. Chem. Lett.* **2020**, *11* (6), 2036–2043. https://doi.org/10.1021/acs.jpclett.9b03873.

(4) Xu, K.; Allen, A. C.; Luo, B.; Vickers, E. T.; Wang, Q.; Hollingsworth, W. R.; Ayzner, A. L.; Li, X.; Zhang, J. Z. Tuning from Quantum Dots to Magic Sized Clusters of CsPbBr3 Using Novel Planar Ligands Based on the Trivalent Nitrate Coordination Complex. *J. Phys. Chem. Lett.* **2019**, *10* (15), 4409–4416. https://doi.org/10.1021/acs.jpclett.9b01738.

(5) Liu, L.; Xu, K.; Vickers, E. T.; Allen, A. C.; Li, X.; Peng, L.; Zhang, J. *Varying the Concentration of Organic Acid and Amine Ligands Allows Tuning between Quantum Dots and Magic-Sized Clusters of CH3NH3PbBr3 Perovskite: Implications for Photonics and Energy Conversion | ACS Applied Nano Materials*. https://pubs.acs.org/doi/abs/10.1021/acsanm.0c02894 (accessed 2021-04-13).

(6) Lou, Y.; Fang, M.; Chen, J.; Zhao, Y. Formation of Highly Luminescent Cesium Bismuth Halide Perovskite Quantum Dots Tuned by Anion Exchange. *Chem. Commun.* **2018**, *54* (30), 3779–3782. https://doi.org/10.1039/C8CC01110A.

(7) Wang, H.; Sui, N.; Bai, X.; Zhang, Y.; Rice, Q.; Seo, F. J.; Zhang, Q.; Colvin, V. L.; Yu, W. W. Emission Recovery and Stability Enhancement of Inorganic Perovskite Quantum Dots. *J. Phys. Chem. Lett.* **2018**, *9* (15), 4166–4173. https://doi.org/10.1021/acs.jpclett.8b01752.

(8) Wei, Y.; Cheng, Z.; Lin, J. An Overview on Enhancing the Stability of Lead Halide Perovskite Quantum Dots and Their Applications in Phosphor-Converted LEDs. *Chemical Society Reviews* **2019**, *48* (1), 310–350. https://doi.org/10.1039/C8CS00740C.

(9) Wang, S.; Wang, Y.; Zhang, Y.; Zhang, X.; Shen, X.; Zhuang, X.; Lu, P.; Yu, W. W.; Kershaw, S. V.; Rogach, A. L. Cesium Lead Chloride/Bromide Perovskite Quantum Dots with Strong Blue Emission Realized via a Nitrate-Induced Selective Surface Defect Elimination Process. *J. Phys. Chem. Lett.* **2019**, *10* (1), 90–96. https://doi.org/10.1021/acs.jpclett.8b03750.

(10) Bi, C.; Kershaw, S. V.; Rogach, A. L.; Tian, J. Improved Stability and Photodetector Performance of CsPbI3 Perovskite Quantum Dots by Ligand Exchange with Aminoethanethiol. *Advanced Functional Materials* **2019**, *29* (29), 1902446. https://doi.org/10.1002/adfm.201902446.

(11) Zhang, Z.-X.; Li, C.; Lu, Y.; Tong, X.-W.; Liang, F.-X.; Zhao, X.-Y.; Wu, D.; Xie, C.; Luo, L.-B. Sensitive Deep Ultraviolet Photodetector and Image Sensor Composed of Inorganic Lead-Free Cs3Cu2I5 Perovskite with Wide Bandgap. *J. Phys. Chem. Lett.* **2019**, *10* (18), 5343–5350. https://doi.org/10.1021/acs.jpclett.9b02390.

(12) Lu, L.-Q.; Tan, T.; Tian, X.-K.; Li, Y.; Deng, P. Visual and Sensitive Fluorescent Sensing for Ultratrace Mercury Ions by Perovskite Quantum Dots. *Analytica Chimica Acta* **2017**, *986*, 109–114. https://doi.org/10.1016/j.aca.2017.07.014.

(13) Wang, Y.; Zhu, Y.; Huang, J.; Cai, J.; Zhu, J.; Yang, X.; Shen, J.; Jiang, H.; Li, C. CsPbBr3 Perovskite Quantum Dots-Based Monolithic Electrospun Fiber Membrane as an Ultrastable and Ultrasensitive Fluorescent Sensor in Aqueous Medium. *J. Phys. Chem. Lett.* **2016**, *7* (21), 4253–4258. https://doi.org/10.1021/acs.jpclett.6b02045.

(14) *Precise Control of Quantum Confinement in Cesium Lead Halide Perovskite Quantum Dots via Thermodynamic Equilibrium | Nano Letters*. https://pubs.acs.org/doi/abs/10.1021/acs.nanolett.8b00861?casa_token=csmbeRgCtKQAAAAA:hTz_702eAEatMYdwszjn9BFr6SuwZfVlTLgZKH8YBT3zEkRWbnNpK7o7cFUSmBv49zID-1dARsKEHsA (accessed 2022-03-23).

(15) Tyagi, P.; Arveson, S. M.; Tisdale, W. A. Colloidal Organohalide Perovskite Nanoplatelets Exhibiting Quantum Confinement. *J. Phys. Chem. Lett.* **2015**, *6* (10), 1911–1916. https://doi.org/10.1021/acs.jpclett.5b00664.

(16) Stein, J. L.; Steimle, M. I.; Terban, M. W.; Petrone, A.; Billinge, S. J. L.; Li, X.; Cossairt, B. M. Cation Exchange Induced Transformation of InP Magic-Sized Clusters. *Chem. Mater.* **2017**, *29* (18), 7984–7992. https://doi.org/10.1021/acs.chemmater.7b03075.

(17) Xu, K.; Vickers, E. T.; Luo, B.; Allen, A. C.; Chen, E.; Roseman, G.; Wang, Q.; Kliger, D. S.; Millhauser, G. L.; Yang, W.; Li, X.; Zhang, J. Z. First Synthesis of Mn-Doped Cesium Lead Bromide Perovskite Magic Sized Clusters at Room Temperature. *J. Phys. Chem. Lett.* **2020**, *11* (3), 1162–1169. https://doi.org/10.1021/acs.jpclett.9b03700.

(18) Impact of Molecular Ligands in the Synthesis and Transformation between Metal Halide Perovskite Quantum Dots and Magic Sized Clusters - Acsphyschemau (1).Pdf.

(19) Vickers, E. T.; Chen, Z.; Cherrette, V.; Smart, T.; Zhang, P.; Ping, Y.; Zhang, J. Z. Interplay between Perovskite Magic-Sized Clusters and Amino Lead Halide

Molecular Clusters. *Research (Wash D C)* **2021**, *2021*. https://doi.org/10.34133/2021/6047971.

(20) White, S. L.; Banerjee, P.; Chakraborty, I.; Jain, P. K. *Ion Exchange Transformation of Magic-Sized Clusters*. ACS Publications. https://pubs.acs.org/doi/full/10.1021/acs.chemmater.6b03882 (accessed 2022-02-17). https://doi.org/10.1021/acs.chemmater.6b03882.

(21) Vickers, E. T.; Xu, K.; Dreskin, B. W.; Graham, T. A.; Li, X.; Zhang, J. Z. Ligand Dependent Growth and Optical Properties of Hybrid Organo-Metal Halide Perovskite Magic Sized Clusters. *J. Phys. Chem. C* **2019**, *123* (30), 18746–18752. https://doi.org/10.1021/acs.jpcc.9b05521.

(22) Pun, A. B.; Mazzotti, S.; Mule, A. S.; Norris, D. J. Understanding Discrete Growth in Semiconductor Nanocrystals: Nanoplatelets and Magic-Sized Clusters. *Acc. Chem. Res.* **2021**, *54* (7), 1545–1554. https://doi.org/10.1021/acs.accounts.0c00859.

(23) Jiang, Z.-J.; Kelley, D. F. Role of Magic-Sized Clusters in the Synthesis of CdSe Nanorods. *ACS Nano* **2010**, *4* (3), 1561–1572. https://doi.org/10.1021/nn100076f.

(24) R. Nevers, D.; B. Williamson, C.; Hanrath, T.; D. Robinson, R. Surface Chemistry of Cadmium Sulfide Magic-Sized Clusters: A Window into Ligand-Nanoparticle Interactions. *Chemical Communications* **2017**, *53* (19), 2866–2869. https://doi.org/10.1039/C6CC09549F.

(25) Zhang, J. Z. A "Cocktail" Approach to Effective Surface Passivation of Multiple Surface Defects of Metal Halide Perovskites Using a Combination of Ligands. *J. Phys. Chem. Lett.* **2019**, *10* (17), 5055–5063. https://doi.org/10.1021/acs.jpclett.9b01166.

(26) Guarino-Hotz, M.; Barnett, J. L.; Pham, L. B.; Win, A. A.; Cherrette, V. L.; Zhang, J. Z. Tuning between Methylammonium Lead Bromide Perovskite Magic-Sized Clusters and Quantum Dots through Ligand Assisted Reprecipitation at Elevated Temperatures. *J. Phys. Chem. C* **2022**, *126* (32), 13854–13862. https://doi.org/10.1021/acs.jpcc.2c04384.

(27) Sandeep, K.; Gopika, K. Y.; Revathi, M. R. Role of Capped Oleyl Amine in the Moisture-Induced Structural Transformation of CsPbBr3 Perovskite Nanocrystals. *physica status solidi (RRL) – Rapid Research Letters* **2019**, *13* (11), 1900387. https://doi.org/10.1002/pssr.201900387.

(28) Kim, Y.; Yassitepe, E.; Voznyy, O.; Comin, R.; Walters, G.; Gong, X.; Kanjanaboos, P.; Nogueira, A. F.; Sargent, E. H. Efficient Luminescence from Perovskite Quantum Dot Solids. *ACS Appl. Mater. Interfaces* **2015**, *7* (45), 25007–25013. https://doi.org/10.1021/acsami.5b09084.

(29) Ouyang, Y.; Li, Y.; Zhu, P.; Li, Q.; Gao, Y.; Tong, J.; Shi, L.; Zhou, Q.; Ling, C.; Chen, Q.; Deng, Z.; Tan, H.; Deng, W.; Wang, J. Photo-Oxidative Degradation of Methylammonium Lead Iodide Perovskite: Mechanism and Protection. *Journal of Materials Chemistry A* **2019**, *7* (5), 2275–2282. https://doi.org/10.1039/C8TA12193A.

(30) Shirayama, M.; Kato, M.; Miyadera, T.; Sugita, T.; Fujiseki, T.; Hara, S.; Kadowaki, H.; Murata, D.; Chikamatsu, M.; Fujiwara, H. Degradation Mechanism of $CH_3NH_3PbI_3$ Perovskite Materials upon Exposure to Humid Air. *Journal of Applied Physics* **2016**, *119* (11), 115501. https://doi.org/10.1063/1.4943638.

(31) Abdelmageed, G.; Jewell, L.; Hellier, K.; Seymour, L.; Luo, B.; Bridges, F.; Zhang, J. Z.; Carter, S. Mechanisms for Light Induced Degradation in $MAPbI_3$ Perovskite Thin Films and Solar Cells. *Appl. Phys. Lett.* **2016**, *109* (23), 233905. https://doi.org/10.1063/1.4967840.

(32) Kundu, S.; Kelly, T. L. In Situ Studies of the Degradation Mechanisms of Perovskite Solar Cells. *EcoMat* **2020**, *2* (2). https://doi.org/10.1002/eom2.12025.

(33) Li, B.; Li, Y.; Zheng, C.; Gao, D.; Huang, W. Advancements in the Stability of Perovskite Solar Cells: Degradation Mechanisms and Improvement Approaches. *RSC Adv.* **2016**, *6* (44), 38079–38091. https://doi.org/10.1039/C5RA27424A.

(34) Busatto, S.; de Mello Donega, C. Magic-Size Semiconductor Nanostructures: Where Does the Magic Come From? *ACS Mater. Au* **2022**, *2* (3), 237–249. https://doi.org/10.1021/acsmaterialsau.1c00075.

(35) Raja, S. N.; Bekenstein, Y.; Koc, M. A.; Fischer, S.; Zhang, D.; Lin, L.; Ritchie, R. O.; Yang, P.; Alivisatos, A. P. Encapsulation of Perovskite Nanocrystals into Macroscale Polymer Matrices: Enhanced Stability and Polarization. *ACS Appl. Mater. Interfaces* **2016**, *8* (51), 35523–35533. https://doi.org/10.1021/acsami.6b09443.

(36) de Mello Donegá, C.; Liljeroth, P.; Vanmaekelbergh, D. Physicochemical Evaluation of the Hot-Injection Method, a Synthesis Route for Monodisperse Nanocrystals. *Small* **2005**, *1* (12), 1152–1162. https://doi.org/10.1002/smll.200500239.

(37) Zhang, L.-J.; Shen, X.-C.; Liang, H.; Yao, J.-T. Multiple Families of Magic-Sized ZnSe Quantum Dots via Noninjection One-Pot and Hot-Injection Synthesis. *J. Phys. Chem. C* **2010**, *114* (50), 21921–21927. https://doi.org/10.1021/jp1044282.

(38) Houk, L. R.; Challa, S. R.; Grayson, B.; Fanson, P.; Datye, A. K. The Definition of "Critical Radius" for a Collection of Nanoparticles Undergoing Ostwald Ripening. *Langmuir* **2009**, *25* (19), 11225–11227. https://doi.org/10.1021/la902263s.

(39) Boyd, C. C.; Cheacharoen, R.; Leijtens, T.; McGehee, M. D. Understanding Degradation Mechanisms and Improving Stability of Perovskite Photovoltaics. *Chem. Rev.* **2019**, *119* (5), 3418–3451. https://doi.org/10.1021/acs.chemrev.8b00336.

(40) Permatasari, F. A.; Masitoh, H. E.; Mahen, E. C. S.; Nuryadin, B. W.; Aimon, A. H.; Syah, Y. M.; Iskandar, F. Synergetic Effect of the Surface Ligand and SiO2 Driven Photoluminescence Stabilization of the CH3NH3PbBr3 Perovskite Magic-Sized Clusters. *Sci Rep* **2021**, *11* (1), 22211. https://doi.org/10.1038/s41598-021-01560-4.

(41) Wu, H.; Lin, S.; Wang, R.; You, X.; Chi, Y. Water-Stable and Ion Exchange-Free Inorganic Perovskite Quantum Dots Encapsulated in Solid Paraffin and Their Application in Light Emitting Diodes. *Nanoscale* **2019**, *11* (12), 5557–5563. https://doi.org/10.1039/C8NR09384A.

(42) Yordanov, G. G.; Yoshimura, H.; Dushkin, C. D. Fine Control of the Growth and Optical Properties of CdSe Quantum Dots by Varying the Amount of Stearic Acid in a Liquid Paraffin Matrix. *Colloids and Surfaces A: Physicochemical and Engineering Aspects* **2008**, *322* (1), 177–182. https://doi.org/10.1016/j.colsurfa.2008.03.002.

(43) Liu, S.; Yuan, L.; Zhao, Y.; Chen, Y.; Xiang, W.; Liang, X. Water-Stable All-Inorganic CsPb1-XSnXBr2I Perovskite Quantum Dots Encapsulated in Paraffin for White Light-Emitting Diodes. *Journal of Alloys and Compounds* **2019**, *806*, 1022–1028. https://doi.org/10.1016/j.jallcom.2019.07.340.

(44) Baranov, D.; Lynch, M. J.; Curtis, A. C.; Carollo, A. R.; Douglass, C. R.; Mateo-Tejada, A. M.; Jonas, D. M. Purification of Oleylamine for Materials Synthesis and Spectroscopic Diagnostics for Trans Isomers. *Chem. Mater.* **2019**, *31* (4), 1223–1230. https://doi.org/10.1021/acs.chemmater.8b04198.

(45) Liu, F.; Wang, F.; Hansen, K. R.; Zhu, X.-Y. Bimodal Bandgaps in Mixed Cesium Methylammonium Lead Bromide Perovskite Single Crystals. *J. Phys. Chem. C* **2019**, *123* (23), 14865–14870. https://doi.org/10.1021/acs.jpcc.9b03536.

(46) Songvilay, M.; Wang, Z.; Sakai, V. G.; Guidi, T.; Bari, M.; Ye, Z.-G.; Xu, G.; Brown, K. L.; Gehring, P. M.; Stock, C. Decoupled Molecular and Inorganic Framework Dynamics in CH3NH3PbCl3. *Phys Rev Mater* **2019**, *3*, 10.1103/PhysRevMaterials.3.125406. https://doi.org/10.1103/PhysRevMaterials.3.125406.